High-Mass Drell-Yan Cross-Section and Search for New Phenomena in Multi-Electron/Positron Final States with the ATLAS Detector

Dissertation
zur Erlangung des Grades „Doktor der Naturwissenschaften“
am Fachbereich Physik, Mathematik und Informatik
der Johannes Gutenberg-Universität in Mainz

Simon Wollstadt
geboren in Hamburg

Mainz, Oktober 2014

Institut für Physik
Staudingerweg 7, 55128 Mainz, Deutschland
Johannes Gutenberg-Universität Mainz

JOHANNES GUTENBERG
UNIVERSITÄT MAINZ

PDF-XChange Editor
Click to BUY NOW!
tracker-software.com

Simon Wollstadt: *High-Mass Drell-Yan Cross-Section and Search for New Phenomena in Multi-Electron/Positron Final States with the ATLAS Detector,* © Oktober 2014

Erstgutachter:
Zweitgutachter:

Datum der mündlichen Püfung: 12.02.2015

ABSTRACT

The Standard Model of particle physics is a very successful theory which describes nearly all known processes of particle physics very precisely. Nevertheless, there are several observations which cannot be explained within the existing theory. In this thesis, two analyses with high energy electrons and positrons using data of the ATLAS detector are presented. One, probing the Standard Model of particle physics and another searching for phenomena beyond the Standard Model.

The production of an electron-positron pair via the Drell-Yan process leads to a very clean signature in the detector with low background contributions. This allows for a very precise measurement of the cross-section and can be used as a precision test of perturbative quantum chromodynamics (pQCD) where this process has been calculated at next-to-next-to-leading order (NNLO). The invariant mass spectrum m_{ee} is sensitive to parton distribution functions (PFDs), in particular to the poorly known distribution of antiquarks at large momentum fraction (Bjoerken x). The measurement of the high-mass Drell-Yan cross-section in proton-proton collisions at a center-of-mass energy of $\sqrt{s} = 7\,\text{TeV}$ is performed on a dataset collected with the ATLAS detector, corresponding to an integrated luminosity of $4.7\ \text{fb}^{-1}$. The differential cross-section of $pp \to Z^0/\gamma^* + X \to e^+e^- + X$ is measured as a function of the invariant mass in the range $116\ \text{GeV} < m_{ee} < 1500\ \text{GeV}$. The background is estimated using a data-driven method and Monte Carlo simulations. The final cross-section is corrected for detector effects and different levels of final state radiation corrections. A comparison is made to various event generators and to predictions of pQCD calculations at NNLO. A good agreement within the uncertainties between measured cross-sections and Standard Model predictions is observed.

Examples of observed phenomena which can not be explained by the Standard Model are the amount of dark matter in the universe and neutrino oscillations. To explain these phenomena several extensions of the Standard Model are proposed, some of them leading to new processes with a high multiplicity of electrons and/or positrons in the final state. A model independent search in multi-object final states, with objects defined as electrons and positrons, is performed to search for these phenomenas. The dataset collected at a center-of-mass energy of $\sqrt{s} = 8\,\text{TeV}$, corresponding to an integrated luminosity of $20.3\ \text{fb}^{-1}$ is used. The events are separated in different categories using the object multiplicity. The data-driven background method, already used for the cross-section measurement was developed further for up to five objects to get an estimation of the number of events including fake contributions. Within the uncertainties the comparison between data and Standard Model predictions shows no significant deviations.

KURZFASSUNG

Das Standardmodell der Teilchenphysik ist eine sehr erfolgreiche Theorie, welche nahezu alle bekannten Prozesse mit hoher Genauigkeit beschreibt. Allerdings gibt es einige experimentelle Beobachtungen die durch die existierende Theorie nicht beschrieben werden. In dieser Arbeit werden zwei Analysen mit hoch energetischen Elektronen/-Positronen präsentiert. Die verwendeten Daten wurden mit dem ATLAS Detektor aufgezeichnet. Die erste Analyse ist ein Test des Standardmodells der Teilchenphysik, die zweite sucht nach Phänomenen jenseits des Standardmodells.

Die durch den Drell-Yan Prozess erzeugten Elektron-Positron Paare hinterlassen eine saubere Signatur im Detektor, was zu einer geringen Anzahl an Untergrundereignissen führt. Dies erlaubt eine sehr genaue Messung des Wirkungsquerschnitts und kann als Präzisionstest der störungstheoretischen Quatenchromodynamik (pQCD) verwendet werden, da der Wirkungsquerschnitt in nächst-zu-nächstführender Ordnung (NNLO) berechnet werden kann. Die Partonverteilungsfunktionen und im speziellen die schlecht bestimmten Verteilungen für Antiquarks bei hohem Impulsanteil (Bjoerken x) sind sensitiv auf die invariante Massenverteilung m_{ee}. Die Messung des Drell-Yan Wirkungsquerschnitts in Proton-Proton Kollisionen wurde mit Daten des ATLAS Detektors durchgeführt, welche bei einer Schwerpunktsenergie von $\sqrt{s} = 7\,\text{TeV}$ aufgezeichnet wurden und einer integrierten Luminosität von 4.7 fb^{-1} entsprechen. Der differenzielle Wirkungsquerschnitt von $pp \to Z^0/\gamma^* + X \to e^+e^- + X$ wurde als Funktion der invarianten Masse im Bereich $116\,\text{GeV} < m_{ee} < 1500\,\text{GeV}$ gemessen. Der Untergrund wurde mit Hilfe einer datengetriebenen Methode und Monte Carlo Simulationen abgeschätzt. Der finale Wirkungsquerschnitt wurde auf Detektoreffekte korrigiert und mit verschiedenen Monte Carlo Generatoren und einer theoretischen Vorhersage der pQCD verglichen. Innerhalb der Unsicherheiten zeigt die Messung eine gute Übereinstimmung mit den Vorhersagen des Standardmodells.

In verschiedenen Experimenten wurden Phänomene beobachtet, welche nicht durch das Standardmodell erklärt werden können. Beispiele hierfür sind die gemessene Menge an dunkler Materie im Universum und die in Experimenten beobachtete Neutrino-Oszillation. Um diese und andere Phänomene zu erklären gibt es eine Vielzahl an vorgeschlagenen Erweiterungen des Standardmodells. Einige von ihnen führen zu neuen Prozessen mit einer großen Anzahl an Elektronen und/oder Positronen im Endzustand. Um solche Prozesse zu finden wurde eine modellunabhängige Suche nach Endzuständen mit einer hohen Elektronen/Positronen Multiplizität durchgeführt. Dafür wurden die Daten, welche vom ATLAS Detektor bei einer Schwerpunktsenergie von $\sqrt{s} = 8\,\text{TeV}$ aufgezeichnet wurden und einer integrierten Luminosität von 20.3 fb^{-1} entsprechen, verwendet. Die selektierten Ereignisse wurden anhand ihrer Multiplizität separiert. Die datengetriebene Methode, welche bereits für die Wirkungsquerschnittsmessung verwendet wurde, wurde so erweitert, dass sie für Ereignisse mit bis zu fünf Objekten verwendet werden konnte. Mit Hilfe dieser Methode wurde die Anzahl der zu erwartenden Ereignisse, in denen ein oder mehrere Objekte fehlerhaft als Elektron oder Positron identifiziert wurden, abgeschätzt. Der Vergleich der selektierten Ereignisse mit der Standardmodellerwartung zeigt keine signifikanten Abweichungen.

CONTENTS

PDF-XChange Editor Click to BUY NOW! tracker-software.com

PDF-XChange Editor
Click to BUY NOW!
tracker-software.com

LIST OF FIGURES

PDF-XChange Editor
Click to BUY NOW!
tracker-software.com

LIST OF TABLES

PDF-XChange Editor
Click to BUY NOW!
tracker-software.com

PDF-XChange Editor
Click to BUY NOW!
tracker-software.com

Part I

INTRODUCTION AND THEORY

PDF-XChange Editor
Click to BUY NOW!
tracker-software.com

PDF-XChange Editor Click to BUY NOW! tracker-software.com

1

INTRODUCTION

> By convention hot, by convention cold, but in reality atoms and void, and also in reality we know nothing, since the truth is at bottom.
>
> (Democrit (around 400 BC))

The idea that matter is made up of indivisible units, called "atoms[1]", was already postulated in the ancient world and is valid until the present day. The ideas of Democrit [1] were valid until the early 1900s, when Rutherford and others proved in scattering experiments that atoms have a substructure [2]. This discovery was a milestone in particle physics and led to a large number of experiments and new theories. In the 1950s and 1960s, a bewildering variety of particles were found in scattering experiments known as the "particle zoo". With the unification of the electromagnetic and weak interaction by Glashow [3] 1961 and the incorporation of the Higgs mechanism by Weinberg [4] and Salam [5] 1967, the modern form of the Standard Model theory was born. Gell-Mann [6] and Zweig [7] proposed already in 1964 an ordering scheme for hadrons by introducing quarks. The Standard Model was complemented by adding the theory of the strong interaction between 1973 and 1974 which explains the observed particles as combinations of a small number of fundamental particles (quarks and antiquarks). With high energy accelerators, it was possible to study the substructure further and verify the predicted particles. Important achievements were the discovery of the gluon 1979 at the PETRA accelerator at DESY and the massive gauge bosons $W^{\pm}$, Z^0 [8, 9] 1983 at the Sp$\bar{p}$S at CERN. With the discovery of the top quark [10, 11] (1995) and the tau neutrino [12] (2000), both at the Tevatron (Fermilab), and the Higgs boson 2012 with the ATLAS [13] and CMS [14] experiments at the Large Hadron Collider (LHC), all particles predicted by the Standard Model were found.
The Standard Model of particle physics is a very elegant theory which can explain three of the four fundamental forces and all known particles, but there are several observations which cannot be explained within the existing theory. In the Standard Model, neutrinos are assumed to be massless particles but neutrino flavor oscillation has been observed by experiments [15]. This is only possible for massive particles. Theoretical extensions of the Standard Model such as the Seesaw mechanism [16], predict massive neutrinos. Interestingly, these models can lead to final states with three or four electrons and/or positrons. From cosmological observations [17], we know that only ~4% of the universe is made of "visible matter" and the Standard Model cannot explain the observed amount of dark matter and dark energy. Also the size of the matter/antimatter asymmetry cannot be explained by the Standard Model, even if CP-violating processes [18, 19] are taken into account which lead to a small imbalance between matter and

1 The word atom is coming from the greek word átomos, which means indivisible.

antimatter. A quite elegant explanation for dark matter would be new stable particles, predicted for example by supersymetric (SUSY) theories [20], where each fermion has a bosonic superpartner and vice versa.

The LHC is the largest and most powerful particle accelerator in the world, designed with the aim to probe proton-proton collisions[2] at very high energies. The ATLAS experiment is one of the two multipurpose detectors located at the LHC and is able to measure the particles produced in the collisions at very high precision. The goal of the LHC and the associated experiments is to probe the Standard Model at high energy regimes and search for new phenomena beyond the Standard Model. In this thesis, two analyses, a probe of the Standard Model and a model independent search, are presented.

The differential cross-section $d\sigma(pp \to e^+e^- + X)/dm_{ee}$ of the high-mass Drell-Yan process is theoretically described by perturbative quantum chromodynamics (pQCD) at next-to-next-to-leading order (NNLO). A clean experimental signature, low background and small experimental uncertainties allow a precision test of pQCD. The invariant mass spectrum is also sensitive to parton distribution functions (PFDs), in particular to the poorly known distribution of antiquarks at large Bjoerken x, where x can be interpreted at leading order as the momentum fraction of the proton carried by the interacting parton. Furthermore, the Drell-Yan production of e^+e^- pairs is a source of background for other Standard Model processes and the mass spectrum may be modified by new physics phenomena. The measurement of the cross-section in proton-proton collisions at a center-of-mass energy of $\sqrt{s} = 7\,\text{TeV}$ was performed on a dataset collected with the ATLAS detector, corresponding to an integrated luminosity of $4.7\,\text{fb}^{-1}$.

The second analysis presented in this thesis is a model independent search for phenomena beyond the Standard Model with multi-objects final states, with objects defined as electrons and positrons. This is motivated by several theoretical extensions of the Standard Model which could lead to final states with three or more electrons and/or positrons. One example is the decay of massive neutrinos or SUSY particles which could lead to such final states. For three or more electrons and/or positrons the number of expected events from Standard Model processes is quite small and electrons and positrons have a clean signature in the detector. For electrons and positrons it is possible to extend the phase space by including objects from the forward region[3] of the detector. The search is performed on a dataset collected in proton-proton collisions at a center-of-mass energy of $\sqrt{s} = 8\,\text{TeV}$, corresponding to an integrated luminosity of $20.3\,\text{fb}^{-1}$.

This thesis is structured as follows: Chapter 2 discusses the fundamental theory of the two analyses. An overview of the Standard Model of particle physics and the physics of a proton-proton collision are presented. This chapter is complemented by an introduction of the Drell-Yan process and a motivation for physical models beyond the Standard Model with multi-electron final states. In Chapter 3, the LHC and the associated experiments will be described with a focus on the ATLAS detector and its relevant detector components. Chapter 4 gives an overview of the reconstruction and identification algorithms for electrons and positrons at the ATLAS detector. Part ii is concluded by chapter 5 where the important parts, namely event generation and de-

2 In a different mode also heavy ions (usually lead ions) are accelerated.

3 This is the region close to the beam pipe, which is not covered by the tracking system of the detector.

tector simulation, of Monte Carlo simulations are discussed. In Part iii of this thesis, the measurement of the differential cross-section of the high-mass Drell-Yan process $pp \to Z^0/\gamma^* + X \to e^+e^- + X$ in bins of m_{ee} is presented. Chapter 7 addresses the event selection and in Chapter 8, the methods for background determination are shown. The corrections for detector effects are introduced in Chapter 9 and the results are presented in Chapter 10. Part iv is about the model independent search for new phenomena in multi-electron final states. The selection cuts are introduced in Chapter 12. After a description of the procedure to obtain the Standard Model prediction in Chapter 13, a validation of the methods is done in Chapter 14. The comparison between data and the Standard Model prediction concludes this analysis in Chapter 15. A summary of the results and a short outlook to further perspectives of the two analyses is given in Part v.

PDF-XChange Editor
Click to BUY NOW!
tracker-software.com

2

THEORY

In this chapter, the theoretical basics for the physics discussed in this thesis will be provided. After a brief introduction of the fundamental interactions in nature and the Standard Model (SM) of particle physics, the specific processes relevant for a proton-proton collision are presented. This is concluded with the introduction of the Drell-Yan process. In the last section, physical processes with multi-electron final states are described and theoretical models beyond the Standard Model which could lead to a multi-electron final state are motivated. Throughout the thesis, natural units are used, that means that the speed of light (c) and the Planck Constant ($\hbar$) are set to one.

2.1 THE STANDARD MODEL

The Standard Model (SM) of particle physics is a fundamental theory to describe all known elementary particles and their interactions [21]. The SM provides a description for three of the four fundamental interactions: the weak interaction which is responsible for radioactive decays and nuclear fusion, the electromagnetic interaction, describing the interaction between charged particles and the strong interaction, which binds quarks into nuclei. The electromagnetic and weak interaction was unified into the electroweak theory by Glashow [3], Salam [5] and Weinberg [4] in the 1960s. The fourth force, gravitation, becomes only important for very large masses or extremely small distances and cannot be described by the SM.
Within the SM, there are two different types of particles: fermions (with half-integral spin) and bosons (with integral spin).
Fermions are divided into two subgroups, quarks (which are subject to the strong interaction) and leptons (which are not subject to the strong interaction). Quarks and leptons occur in three generations with the same quantum numbers but different masses. Table 2.1 and Table 2.2 show the three generations of the fermions with their masses and quantum numbers.
For each fermion there is an anti-particle which is completely identical, but have opposite charge. Fermions can be left- or right-handed. The chargeless neutrinos are an exception and only left handed neutrinos are predicted by the Standard Model. They are the only fermions which do not interact with the electromagnetic force because they carry no charge. They are only influenced by the weak interaction, which couples only to left-handed particles. Therefore, right-handed neutrinos would only interact via gravitation, but in the Standard Model neutrinos are predicted as massless. Since particles from the second or third generation are not stable they will decay into particles from the first generation which are stable (e.g. $\mu^- \rightarrow e^- + \bar{\nu}_e + \nu_\mu$).
Bosons are divided into three groups (one for each interaction). The electromagnetic

Table 2.1: The three generations of the fermions together with their masses [22].

Fermion	1. generation		2. generation		3. generation	
Leptons	e	0.511 MeV	μ	105.7 MeV	τ	1776.8 MeV
	ν_e	< 2 eV	ν_μ	< 0.19 MeV	ν_τ	< 18.2 MeV
Quarks	up(u)	1.9-2.9 MeV	charm (c)	1.2-1.3 GeV	top (t)	173 GeV
	down (d)	4.4-5.3 MeV	strange (s)	87-119 MeV	bottom (b)	4.2 GeV

Table 2.2: Table of the fermions with the quantum numbers for electric charge (Q), hypercharge (Y), weak isospin (T) and the third component of weak isospin (T_3) [22].

Fermion	1. generation	2. generation	3. generation	Q [e]	Y	$\lvert\vec{T}\rvert$	T_3
Leptons	$\begin{pmatrix} e \\ \nu_e \end{pmatrix}_L$	$\begin{pmatrix} \mu \\ \nu_\mu \end{pmatrix}_L$	$\begin{pmatrix} \tau \\ \nu_\tau \end{pmatrix}_L$	-1 0	-1	$\frac{1}{2}$	$-\frac{1}{2}$ $+\frac{1}{2}$
	e_R	μ_R	τ_R	-1	-2	0	0
Quarks	$\begin{pmatrix} u \\ d \end{pmatrix}_L$	$\begin{pmatrix} c \\ s \end{pmatrix}_L$	$\begin{pmatrix} t \\ b \end{pmatrix}_L$	$+\frac{2}{3}$ $-\frac{1}{3}$	$+\frac{1}{3}$	$\frac{1}{2}$	$+\frac{1}{2}$ $-\frac{1}{2}$
	u_R	c_R	t_R	$+\frac{2}{3}$	$+\frac{4}{3}$	0	0
	d_R	s_R	b_R	$-\frac{1}{3}$	$-\frac{2}{3}$		

interaction is mediated by photons (γ). The weak interaction is mediated by the $W^\pm$- and Z^0-bosons; the Z^0 boson mediates the weak neutral current and the $W^\pm$ the weak charged current. The strong interaction is mediated by the exchange of eight different gluons (g) which couple to the so-called color charge. Because gluons carry color charge themselves, they also couple to each other [23]. The gauge bosons are summarized in Table 2.3.

Table 2.3: The gauge bosons of the Standard Model with mass, electric charge and corresponding interaction [22].

Gauge boson	symbol	mass [GeV]	electric charge [e]	interaction
photon	γ	0	0	electromagnetic
$W^\pm$-boson	$W^\pm$	80.385 ± 0.015	± 1	weak
Z^0-boson	Z^0	91.187 ± 0.002	0	electroweak
gluon	g	0	0	strong

Since the Standard Model is a relativistic theory, fermions are represented by spinors and gauge bosons by Lorentz four vectors. Spinor indices are suppressed and Lorentz indices are written as Greek letters ($\nu = 0, 1, 2, 3$). In addition to the spacetime symmetry, there is a larger symmetry under which the Standard Model Lagrangian is invariant, the so called gauge symmetry. This symmetry is local, in the sense that ro-

tations can be different for different spacetime points. It can be shown how the gauge bosons emerge as necessary ingredients of the theory if these local transformations are implemented consistently [24]. Gauge indices will denoted by small Latin letters $a = 1, ..., n$, where n is the number of generators of the respective gauge group or, equivalently, the number of gauge bosons. The gauge group of the Standard Model is $SU_c(3) \times SU_L(2) \times U_Y(1)$. The non-abelian gauge theory of strong interactions, also called quantum chromodynamics (QCD), is based on the $SU_c(3)$. As described in more detail in Section 2.1.2 each of the eight generators of the group corresponds to one of the gluons. Due to this gauge symmetry being an exact one, the gluons are massless. The gauge groups $SU_L(2)$ and $U_Y(1)$ together have four generators and the corresponding gauge bosons (W^1, W^2, W^3, B) couple to the isospin T and the hypercharge Y, respectively. In contrast to QCD, the $SU_L(2) \times U_Y(1)$ gauge symmetry is spontaneously broken. This will be discussed in detail in the next section. As a consequence, three gauge bosons ($W^{\pm}, Z^0$), which are linear combinations of the four generators become massive. The mechanism of spontaneous symmetry breaking predicted an additional massive scalar boson. The so called Higgs-boson was observed by the ATLAS [13] and CMS [14] experiments in 2012. The measured mass and the theoretical quantum numbers of the Higgs-boson are shown in Table 2.4. After the discovery of the Higgs-boson, all particles predicted by the Standard Model were observed by experiments.

Table 2.4: The Higgs-boson of the Standard Model with measured mass and theoretical predicted quantum numbers for the electric charge (Q), hypercharge (Y), weak isospin (T) and the third component of weak isospin (T_3) [22].

Higgs-boson	symbol	mass [GeV]	electric charge [e]	spin	Y_W	$\lvert\vec{T}\rvert$	T_3
Higgs-boson	Φ	125.9 ± 0.4	0	0	1	$\frac{1}{2}$	$-\frac{1}{2}$

Even though the Standard Model seems to provide an extremely accurate description of particle physics over a large range of energy scales, there are still some observed phenomena which cannot be described within its framework. One example is neutrino oscillation, which was discovered by experiments [15]. To explain the oscillation, the neutrinos need to have mass. This could be realized by a modification of the Standard Model, e.g. with the Seesaw mechanism which will discussed later. Other examples are the amount of observed cold dark matter, dark energy, as well as the matter/antimatter asymmetry observed in the universe.
The idea is to have a theory explaining all physical phenomena including gravitation. There are several attempts to extend the Standard Model into a unified field theory or a so called "Theory of everything", but for now there is no widely accepted or verified theory.

2.1.1 *The Electroweak Interaction*

In order to explain the observation that the weak interaction couples only to left handed particles, the isospin T was introduced by Heisenberg [25]. The left-handed fermions are grouped into doublets with $T = 1/2$ and $T_3 = \pm 1/2$ and all right-handed fermions form singlets with $T = 0$ and $T_3 = 0$. The electromagnetic interaction, which couples to left- and right-handed fermions, is described by the hypercharge Y_W which is related via

$$Q = T_3 + \frac{Y_W}{2} \tag{2.1}$$

to the electric charge Q and the third component of the weak isospin T_3 [26]. The corresponding symmetry group related to the weak isospin is the $SU(2)_L$ and their three generators $\tau_i = \sigma_i/2$ are given by the Pauli matrices σ_i [27]. The symmetry group associated to the weak hypercharge is the $U(1)_Y$. For the unified electroweak symmetry, the corresponding group is then the $SU(2)_L \times U(1)_Y$ and the requirement of gauge invariance under this symmetry leads to the following Lagrangian density:

$$\mathcal{L}_{ew} = -\frac{1}{4}\sum_{a=1}^{3} W^{a\mu\nu}W^{a}{}_{\mu\nu} - \frac{1}{4}B_{\mu\nu}B^{\mu\nu} + \sum_{m=1}^{3}\overline{\psi}^{L}_{m} i\not{D}\psi^{L}_{m} + \sum_{m,\sigma=1}^{3}\overline{\psi}^{R}_{m\sigma} i\not{D}\psi^{R}_{m\sigma}\,. \tag{2.2}$$

Here, the kinetic terms of the gauge bosons are described by the first two terms of Equation 2.2. The other two terms are kinetic terms for the fermions, where ψ^L is the left-handed fermion field and ψ^R the right-handed fermion field. The index m indicates the three generations and the σ the flavor components. The symbol $\not{D}$ is defined as $\not{D} = \gamma^\mu D_\mu$ and D_μ is the covariant derivative defined for left-handed fields as

$$D_\mu = \partial_\mu - \frac{i}{2}g_1 Y B_\mu - \frac{i}{2}g_2\sum_{a=1}^{3}\tau_a W^{a}{}_{\mu} \tag{2.3}$$

with g_1 the coupling constant for the $U(1)_Y$ and g_2 the coupling constant for $SU(2)_L$. Right-handed fields are only affected by the B_μ term because they are singlets under SU(2). The field strength tensor of the gauge fields is given by

$$W^{a}{}_{\mu\nu} = \partial_\mu W^{a}{}_{\nu} - \partial_\nu W^{a}{}_{\mu} + g_2\epsilon_{abc}W^{b}{}_{\mu}W^{c}{}_{\nu}\,, \tag{2.4}$$

, where ϵ_{abc} is the total antisymmetric tensor.

$$B_{\mu\nu} = \partial_\mu B_\nu - \partial_\nu B_\mu\,. \tag{2.5}$$

The gauge symmetry forbids mass terms for gauge fields but since their direct discovery in 1983 by the UA1 [8] and UA2 [9] experiments, it is known that the $W^{\pm}$- and Z^0-bosons have mass. Therefore, the symmetry has to be broken. The mechanism of

the spontaneous symmetry breaking is predicting a scalar field, called Higgs [28]. The Lagrangian density of this field (without the terms for Yukawa coupling which will not discussed here) is given by:

$$\mathcal{L}_{\mathrm{Higgs}} = -\left(D_\mu \Phi\right)^\dagger \left(D^\mu \Phi\right) - V\left(\Phi^\dagger \Phi\right) . \tag{2.6}$$

The coupling to gauge bosons is hidden in the covariant derivative, which is defined as in Equation 2.3. The hypercharge and the isospin for the Higgs is given in Table 2.4. Renormalizability and $SU_L(2) \times U_Y(1)$ invariance require the potential $V\left(\Phi^\dagger \Phi\right)$ to be of the form

$$V\left(\Phi^\dagger \Phi\right) = \lambda \left(\Phi^\dagger \Phi\right)^2 - \mu^2 \Phi^\dagger \Phi . \tag{2.7}$$

The λ term describes the self interactions among the scalar field and vacuum stability demands λ to be larger than zero. To realize spontaneous symmetry breaking, μ^2 has to be larger than zero. At the energy scale of electroweak symmetry breaking, the neutral component of the Higgs-doublet becomes the nonzero vacuum expectation value ($v \equiv |\langle \Phi \rangle|$) and can be developed around this

$$\Phi = \begin{pmatrix} \Phi^+ \\ \Phi^0 \end{pmatrix} = \begin{pmatrix} 0 \\ \frac{1}{\sqrt{2}} \left(v + H(x)\right) \end{pmatrix} \quad \text{with} \quad v^2 = \mu^2/\lambda . \tag{2.8}$$

The reel field $H(x)$ is called Higgs-boson. The charged component of the doublet forms the longitudinal component of the now massive gauge bosons. Inserting this into the kinetic term of Equation 2.6 gives:

$$\begin{aligned} -\left(D_\mu \Phi\right)^\dagger \left(D^\mu \Phi\right) = &-\frac{1}{2} \partial_\mu H \partial^\mu H - \frac{1}{8} (v + H)^2 g_2^2 \left(W_\mu^1 - i W_\mu^2\right) \left(W^{1\mu} + i W^{2\mu}\right) \\ &- \frac{1}{8} (v + H)^2 \left(-g_2 W^{3\mu} + g_1 B^\mu\right) \left(-g_2 W_\mu^3 + g_1 B_\mu\right) . \end{aligned} \tag{2.9}$$

With the replacement of

$$W_\mu^\pm \equiv \frac{1}{\sqrt{2}} \left(W_\mu^1 \mp i W_\mu^2\right) \tag{2.10}$$

the masses of the charged gauge bosons ($W^\pm$) are:

$$M_W^2 = \frac{g_2^2 v^2}{4} . \tag{2.11}$$

The masses of the uncharged gauge bosons is coming from the mixture of the remaining gauge fields B and W^3

$$\begin{pmatrix} Z_\mu^0 \\ A_\mu \end{pmatrix} = \begin{pmatrix} \cos\theta_W & -\sin\theta_W \\ \sin\theta_W & \cos\theta_W \end{pmatrix} \begin{pmatrix} W_\mu^3 \\ B_\mu \end{pmatrix} . \tag{2.12}$$

In this Equation θ_W is the so-called Weinberg-angle [29], which was measured to be $\sin^2\theta_W = 0.2312 \pm 0.0001$ [22]. The masses of the uncharged gauge bosons is therefore

$$M_Z^2 = \frac{1}{4}\left(g_1^2 + g_2^2\right) v^2 \ , \ M_\gamma^2 = 0 . \tag{2.13}$$

2.1.2 *The Strong Interaction*

The strong interaction is described by Quantum Chromodynamics (QCD) and is like the electroweak theory a gauge field theory. In contrast to the electroweak symmetry, the strong symmetry is unbroken. The requirement to be gauge invariant under $SU(3)$ transformation leads to the Lagrangian density $\mathcal{L}_{st}$, which can be written as

$$\mathcal{L}_{st} = -\frac{1}{4}\sum_{\alpha=1}^{8} G^\alpha{}_{\mu\nu} G^{\alpha\mu\nu} - \frac{1}{2}\sum_{m=1}^{3} \overline{Q}_m \not{\partial}\, Q_m - \frac{1}{2}\sum_{m=1}^{3} \overline{U}_m \not{\partial}\, U_m - \frac{1}{2}\sum_{m=1}^{3} \overline{D}_m \not{\partial}\, D_m , \tag{2.14}$$

with the field strength tensor of the gauge fields given by

$$G^\alpha{}_{\mu\nu} = \partial_\mu G^\alpha{}_\nu - \partial_\nu G^\alpha{}_\mu + g_3 f^\alpha{}_{\beta\gamma} G^\beta{}_\mu G^\gamma{}_\nu \tag{2.15}$$

and the covariant derivative

$$D_\mu = \partial_\mu - \frac{i}{2} g_3 \sum_{\alpha=1}^{8} G^\alpha{}_\mu \lambda_\alpha . \tag{2.16}$$

The index m indicates the three quark generations. Q_m is the up/down left-handed doublet and U_m and D_m stands for the right-handed up and down like quarks. The structure constants of the SU(3) are denoted by $f^\alpha{}_{\beta\gamma}$ and λ_α are the Gell-Mann matrices [30]. The gauge bosons of the strong interaction, the gluons, carry a color and anti-color charge and couple to all particles with color charge. There are no free charges in the strong interaction in contrast to the other interactions. The coupling strength grows with distance which leads to a phenomenon called confinement, which cannot be described by the perturbation theory. If the distance between two quarks is enlarged, the energy increases until it is large enough to produce quark-antiquark pairs out of the vacuum. Therefore it is not possible to have free quarks or gluons. They only exist in composed systems, which are color neutral. A quark-antiquark pair with the same color charge is called meson and a combination of three quarks with different colors is called baryon. Mesons and baryons together are called hadrons. Quarks and gluons bound in hadrons with high enough energy can be described as asymptotically free (see Figure 2.1). The coupling between partons[1] gets small enough to measure the scattering of single quarks and gluons.

1 The collection of quarks and gluons as components of hadrons are called "partons".

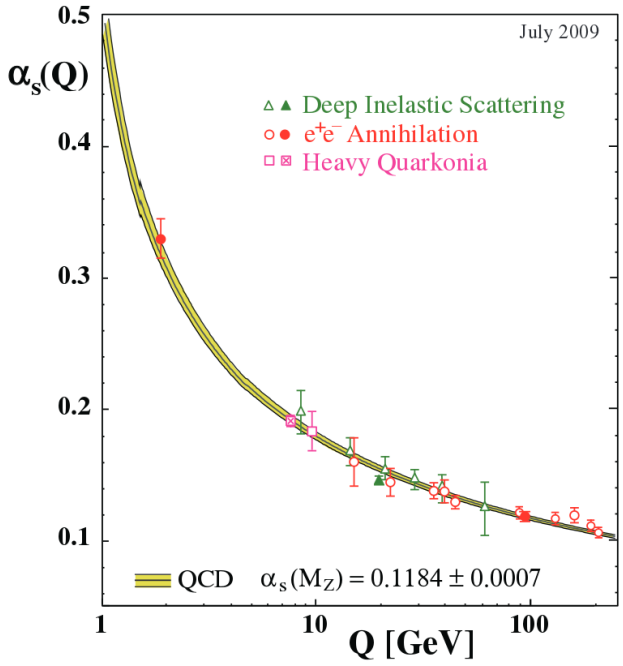

Figure 2.1: Measurements of the strong coupling constant $\alpha(s)$ for different energies. [31].

2.2 PROTON-PROTON COLLISIONS

For proton-proton collisions (pp), the energy of the protons plays a key role. For energies below order of 1 GeV, the collision can be interpreted as an elastic scattering of two charged particles. With increasing energy and therefore increasing resolution, the substructure of the protons, consisting of quarks, antiquarks and gluons, becomes visible. Above the binding energy, the process can be described as a scattering of partons. Therefore, not the complete center of mass energy of the proton-proton collision is available, but only the contribution of the colliding partons. The momentum fraction of the partons inside the proton is given by the parton distribution function (PDF) $f_{a/A}\left(x_a, Q^2\right)$. The cross-section of hadron scattering can be written as:

$$\sigma_{AB} = \sum_{a,b} \int dx_a dx_b f_{a/A}\left(x_a, Q^2\right) f_{b/B}\left(x_b, Q^2\right) \hat{\sigma}_{ab\to X}\,, \tag{2.17}$$

where A,B are the initial state hadrons (protons) and a,b the interacting partons. The momentum fraction x of the partons is called "Bjoerken x". In Figure 2.2 the scattering process is shown as a scheme.
The great advantage of a proton-proton accelerator such as the LHC[2] is that protons are available without large effort. In a proton-antiproton ($p\bar{p}$) accelerator[3] for example the anti-protons have to be produced with large effort for each fill. The disadvantage of a pp-accelerator is that only up- and down valenzquarks[4] are available. That means that the possibility for an interacting antiquarks with high momentum fraction is smaller than for a $p\bar{p}$-accelerator. At the design energy of the LHC this effect gets more and

2 More information about the LHC can be found in the next chapter.
3 The Tevatron at the Fermilab was the largest $p\bar{p}$ accelerator operating until 2011.
4 Valenzquarks are the quarks which are responsible for the quantum numbers of the hadrons.

PDF-XChange Editor Click to BUY NOW! tracker-software.com

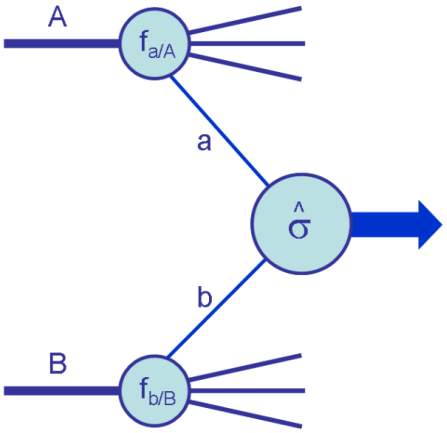

Figure 2.2: Scheme of scattering of two Hadrons at high energy [32].

more irrelevant because the distributions of gluons and antiquarks are getting shifted to larger x. In Figure 2.3, showing the behavior of the PDFs, this is clearly visible.
The substructure of the protons leads to a disadvantage with respect to e^+e^- accelerators. As described before there is only one interaction of two partons for each hard process. The remaining partons of the protons are traveling along the beam axis as indicated in Figure 2.2. Due to the "Confinement" described above, the partons form new hadrons resulting in additional particles in the detector which are not from the hard process. The sum of these particles is called the "underlying event". These disadvantages are compensated by the fact that with a hadron accelerator, it is easier to reach large center-of-mass energies since the energy loss due to synchrotron radiation is proportional to:

$$\Delta E \propto \frac{1}{m_0^4} \tag{2.18}$$

where m_0 is the mass of the accelerated particle.

2.2.1 *Parton Density Function*

The parton density functions (PDFs), which provides the probability that a specific parton carries the fraction x of the proton momentum can not be predicted by any known theory. Different sets of PDFs are obtained by fits on a large number of cross section data points in a large grid of Q^2 and x values. Therefore, the results of many experiments are used. The most commonly used procedure consists of parameterizing the dependence of the parton distributions (quarks, antiquarks, gluon) on the variable x at some low value of $Q^2 = Q_0^2$ and evolving these input distributions up in Q^2 through the DGLAP Equations [33]. Q_0^2 has to be large enough that the unknown terms of the perturbative Equations are assumed to be negligible. Typically, it is chosen in the range between 1 and 2 GeV. The number of unknown parameters is typically between 10 and 30. The factorization theorem allows to derive predictions for different cross sections. These predictions are then fitted to as much of the experimental data together as possi-

ble, to determine the parameters and to provide parton distributions.
Very extensive and precise results from deep inelastic scattering (DIS) experiments, where protons are probed by leptons provide the backbone of parton distribution analysis. The most precise measurements of protons, predominantly at low x values, are provided by the HERA experiments H1 [34] and ZEUS [35]. Additional DIS measurements done at fixed-targets experiments, e.g. at FNAL [36], are at higher x. The DIS data however are insufficient to determine accurately flavor decomposition of the quark and antiquark sea or the gluon distribution at large x. Therefore, additional physical processes are used in the fits. To test the dependency on the gluon distribution single jet inclusive production in nucleon-nucleon interactions are used, selecting jets with large transverse energy. The di-lepton production in the Drell-Yan process is used to probe the sea quark distribution.
There are several groups of physicists which are specialized to this topic. The different groups provide extractions of the PDFs using different collections of experimental data. The extracted PDFs are then made public in a certain order of α_s which is given by the order of the splitting functions used for the DGLAP evolution. In Figure 2.3 two PDFs times Bjoerken x as a function of the momentum fraction x provided by the MSTW PDF group are shown.

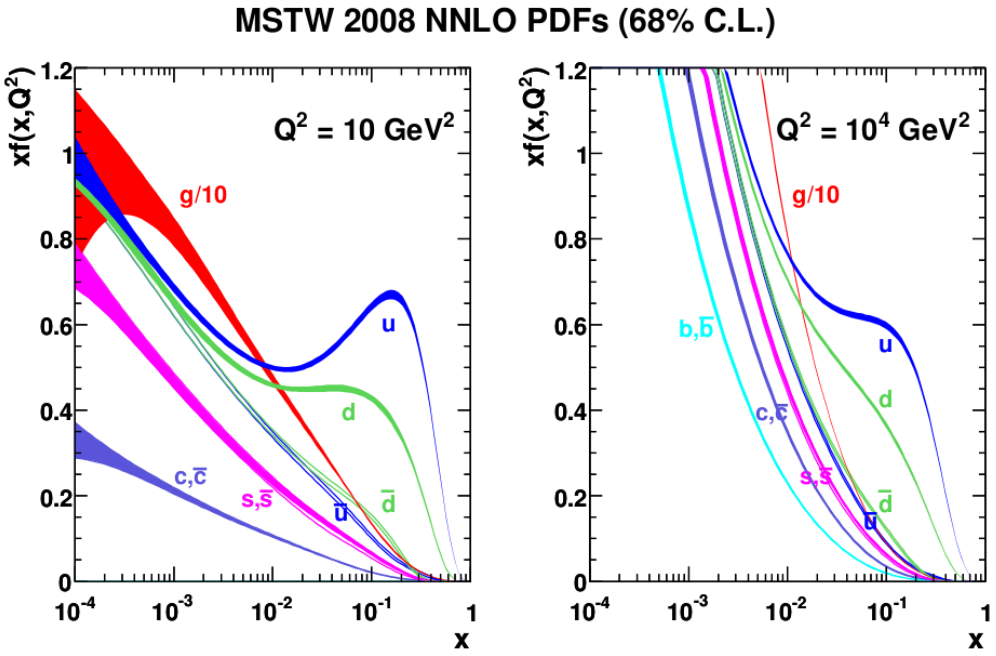

Figure 2.3: The MSTW2008NNLO Parton distribution functions (PDFs) times Bjoerken x for the momentum transfer of $Q^2 = 10\,\mathrm{GeV}^2$ (left) and $Q^2 = 0.01\,\mathrm{TeV}^2$ (right) are shown. The letters indicate the different quark flavor and the gluon (g), respectively. The uncertainties of the PDFs are indicated by the bands. The gluon distribution is divided by a factor of ten for better shape comparison [31].

The gluon distribution is scaled by a factor of 0.1 for better shape comparison. At x values around 0.1 to 0.5 the up and down distributions have a peak which corresponds to the valence quarks of the proton. For higher Q^2 the peaks get more and more smeared and the sea contributions becomes larger for higher x values. At low values of x most of the proton momenta is carried by gluons and the contributions

from the sea (anti-quarks) becomes more dominant. The uncertainties are indicated by the uncertainty bands.
The uncertainties of the PDFs are corresponding to the uncertainties of the measurements used for the global fit. The experimental uncertainties are propagated to the deduced parametrization parameters. The further propagation of these uncertainties to the PDFs can not be done straight forward, since some of these parameters are highly correlated. Normally the Hessian method [37] is used to calculate uncorrelated sets of parameters. These uncertainties of the parameters can directly propagated to the PDF uncertainties. Additional uncertainties arise from the chosen parametrization at Q^0 and the value of α_s used in the evolution.

2.3 DRELL-YAN PROCESS

The Drell-Yan[5] process [38] describes lepton-antilepton pair production via quark-antiquark annihilation. In a hadron collider, a quark of one hadron and an antiquark[6] of the other hadron annihilate to a virtual photon which decays afterwards into a lepton pair ($q\overline{q} \to \gamma^* \to \ell^+\ell^-$). Figure 2.4 shows the scheme of the Drell-Yan process.

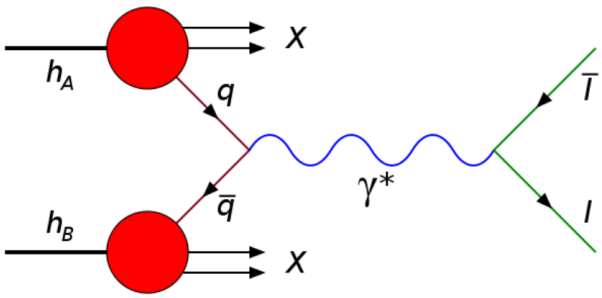

Figure 2.4: Scheme of the Drell-Yan process [39].

The intermediate state decays into all kinematically accessible fermions, but only the electron-positron final state is part of this thesis. The cross-section for this process can be calculated from the fundamental QED $e^+e^- \to \mu^+\mu^-$ cross-section by adding a charge factor [40]:

$$\hat{\sigma}\left(q\overline{q} \to \ell^+\ell^-\right) = \frac{4\pi\alpha^2}{3Q^2} e_q^2 \,, \tag{2.19}$$

where Q^2 is the squared center of mass energy of the incoming partons and e_q^2 is the square of the electric charge of the quarks (in units of e). The differential cross-section, $d\hat{\sigma}/dQ^2$, for the production of lepton pairs having an invariant mass $\sqrt{Q^2}$, where

$$Q^2 = \hat{s} = m^2_{e^+e^-} = (p_q + p_{\overline{q}})^2 \tag{2.20}$$

is,

5 Named after Sidney Drell and Tung-Mow Yan, which suggested the process in 1970.
6 Since a proton consist only of quarks the antiquark has to come from "the quark sea".

$$\frac{d\hat{\sigma}}{dQ^2} = \frac{4\pi\alpha^2}{3Q^2} e_q^2 \delta\left(Q^2 - \hat{s}\right) \tag{2.21}$$

To get the corresponding cross-section for a proton-proton collision, the parton distribution in the protons $f_i(x,\mu)$ has to be considered. This is done with help of the factorization theorem. This is described in detail in Ref. [41]. The corresponding cross-section is written as:

$$\frac{d\sigma}{dQ^2}(pp \to \ell^+\ell^- X) = \left(\frac{1}{3}\right)\left(\frac{1}{3}\right) 3 \sum_q \int dx \int dy f_q(x,\mu) f_{\overline{q}}(y,\mu) \frac{d\hat{\sigma}}{dQ^2}(\mu)\,, \tag{2.22}$$

where the sum is over quark flavor. The factors of $\frac{1}{3}$ average over the initial q and $\overline{q}$ colors and the factor 3 sums over the quark-antiquark combinations which can annihilate to form the colorless virtual photon. The quark and antiquark carry fractions x and y of the momenta of the protons, respectively. The idea of the factorization theorem is that the cross-section is separated into two parts: The process dependent short-distance parton cross section ($\frac{d\hat{\sigma}}{dQ^2}(\mu)$), which is calculable by perturbative QCD, and the universal long-distance functions ($f_q(x,\mu) f_{\overline{q}}(y,\mu)$), which for examples includes the PDFs and have to extracted from global fits. Both terms can be calculated at an arbitrarily chosen factorization scale denoted with μ. If all higher orders[7] are included in the calculation μ cancels out and the calculation is independent of μ. In reality the cross-section is only calculable to next-to-leading order (NLO) or next-to-next-to-leading order (NNLO). This introduce a theoretical uncertainty which is estimated by calculating the cross-section for different μ values. Normally the mass of the intermediate state is chosen as default, in this case $\mu \approx M_{Z/\gamma}$, to reflect the physical process. The uncertainty can be minimized by adding higher order of α_s.
Equation 2.20 can now be written as

$$\hat{s} = (xp_1 + yp_2)^2 \simeq xys\,, \tag{2.23}$$

where $s \simeq 2p_1 \cdot p_2$ is the center-of-mass energy squared of the colliding protons. Combination of Equations 2.21 - 2.23 leads to the final cross-section

$$\frac{d\sigma}{dQ^2}(pp \to \ell^+\ell^- X) = \frac{4\pi\alpha^2}{9Q^2} \sum_q e_q^2 \int dx \int dy f_q(x,\mu) f_{\overline{q}}(y,\mu) \delta\left(1 - xy\frac{s}{Q^2}\right)(\mu)\,. \tag{2.24}$$

2.3.1 *Previous Measurements*

The differential cross-section for Drell-Yan e^+e^- pair production in the high mass range has been reported previously by ATLAS[8] [42], CMS [43], CDF [44] and DØ

7 The rang of the order is defined by the number of involved matrix elements. Additional matrix elements are coming from loop corrections or particle radiations.

8 The analysis in this thesis is a detailed summary of the publication already published by ATLAS.

[45]. With the ATLAS detector a measurement of this channel at the Z-pole ($66\,\mathrm{GeV} < m_{ee} < 116\,\mathrm{GeV}$) with the 2010 dataset was also performed [46]. In addition, searches for physics beyond the Standard Model in the high-mass range of the m_{ee} distribution have been performed [47][48][49] and no deviation from the Standard Model prediction was observed.

2.4 PROCESSES WITH MULTI ELECTRON/POSITRON FINAL STATES

In this section the Standard Model processes which contribute to multi electron/-positron final states are described and some theoretical extensions of the SM which leads to such final states are motivated.

2.4.1 *Processes within the Standard Model*

In the Standard Model only a few processes leads to final states with three or more electrons and/or positrons. The dominant processes with the highest production cross sections are the WZ and ZZ production. In Figure 2.5 the Feynman diagrams of two production channels of these processes are shown.

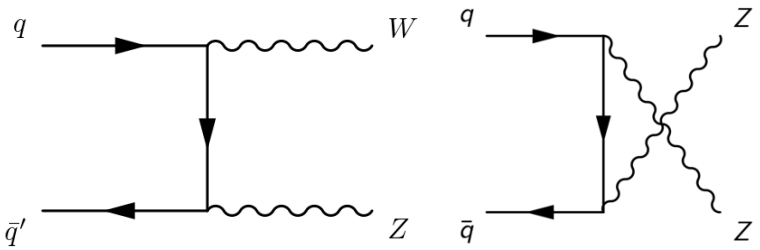

Figure 2.5: On the left side the WZ production in the t-channel and on the right side the ZZ production in the u-channel are shown. The diagrams are taken from Ref. [50] and Ref. [51].

If the Z-boson decays into an electron-positron pair and the W-boson decays into an electron (positron) and a neutrino (anti-neutrino) this processes lead to final states with three and four electrons/positrons. Additional processes, but with much lower production cross-sections[9] are the production of a $t\bar{t}$-pair in association with one or two vector bosons ($t\bar{t}W$, $t\bar{t}Z$, $t\bar{t}WW$). The top quarks can decay via W-bosons into two electrons/positrons and with the associated vector bosons this can leads to three or four electrons/positrons in the final state. The Feynman diagrams of two of these processes are shown in Figure 2.6.
The decay of the Higgs-boson via two Z-bosons is also a process which can lead to final states with four electrons/positrons. In Figure 2.7 the Feynman diagrams of the production via gluon-gluon fusion is shown. This production channel has the highest cross-section for proton-proton collisions at $\sqrt{s} = 7$ TeV.
The last processes which can lead to final states with multi electrons/positrons in the SM are the production of triple vector bosons (WWW^*, ZZZ^*, ZWW^*).

9 The cross-sections are smaller by one order of magnitude for $t\bar{t}W$ and by three orders for $t\bar{t}WW$.

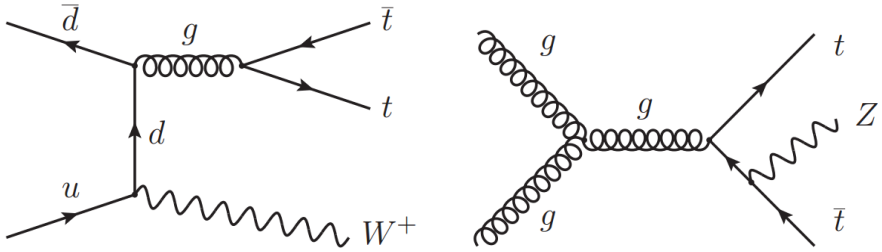

Figure 2.6: The Feynman diagrams of $t\bar{t}$ production in association with a W-boson (left) and with a Z-boson (right). The diagrams are taken from Ref. [52].

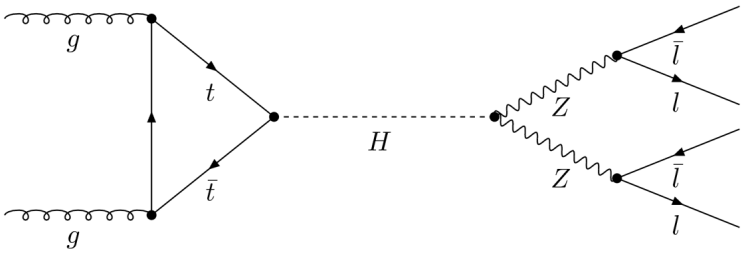

Figure 2.7: This Feynman diagram shows the production of a Higgs-boson via gluon-gluon fusion and the decay via ZZ into four leptons. The diagrams are taken from Ref. [53].

2.4.2 *Theories Beyond the Standard Model*

There are several physics models beyond the Standard Model which have multi lepton final states. Some of these models will be discussed in this section.

Heavy Neutrinos

A well-motivated extension of the Standard Model are models for neutrino masses. If they are explained through a Seesaw mechanism[10] with right-handed neutrinos (Seesaw type I or III), new heavy neutrinos are predicted. They are dominantly produced through $q\bar{q}' \to W_R^{\pm} \to N\ell^{\pm}$ and also decay through weak interactions, via $N \to W^{\pm}\ell^{\mp} \to \ell^{\mp}\ell^{\pm}\nu(\ell q\bar{q})$. The index R indicates that this W-boson couples on right-handed fermions. These models can be probed through final states with three leptons and missing energy. With no lepton-mixing W_R-bosons with masses below ≈ 1.8 TeV are excluded for mass differences between the W_R and N masses larger than 0.3 TeV by previous ATLAS measurements [54]. In this measurements final states with two leptons and jets were analyzed. More informations about the different types of the Seesaw mechanism can be found in Ref. [55].

In type II Seesaw models, the left-handed neutrinos acquire a mass through couplings to a $SU(2)_L$ Higgs triplet with hypercharge $Y = 1$,

10 The Seesaw mechanism is a generic model used to understand the relative sizes of observed neutrino masses, of the order of eV. The simplest version, type I, extends the Standard Model by assuming additional right-handed neutrino fields inert under the electroweak interactions, and the existence of a very large mass scale.

$$\Delta = \begin{pmatrix} \Delta^0 \\ \Delta^+ \\ \Delta^{++} \end{pmatrix} . \tag{2.25}$$

The doubly charged component of this triplet decays either directly into two charged leptons $\Delta^{++} \to \ell^+\ell^+$ or into two W-bosons (which than can decay leptonically). Pair production or production in association with a W-boson can then lead to four or three lepton final states respectively [16]. For a democratic scenario where the branching ratio to each pair of lepton flavors is the same, doubly charged Higgs ($\Delta^{\pm\pm}$) decaying into $e^\pm e^\pm$ pairs are excluded for masses below 258 GeV [56].

Multi-Charged Leptons

Another class of models that can be probed with multi lepton final states are extensions of the SM with double (or higher) charged leptons. Higher charged leptons decay through cascades $L^{++} \to W^+\ell^+ \to \ell^+\ell^+\nu_\ell$. The dominant production mechanism at the LHC is single production $q\bar{q}' \to L^{++}\ell^-$ through a W-boson, but they can also be pair produced through a Z-boson via Drell Yan or gluon fusion processes. The first case results in three leptons with missing energy from the decay of the W-boson, the latter in four lepton final states. A model-independent analysis can be found for example in Ref. [57].

Another obvious example is the supersymmetric completion of the Seesaw II mechanism described above. The fermionic super-partners of the Δ^{++} are candidates for such a multi-charged lepton. Multi-charged leptons are also well motivated by new physics that embed the Standard Model fermions into higher representations of $SU(2)$. In composite Higgs models for example, the fundamental theory has a larger global symmetry than the Standard Model from which only a subgroup is gauged. For example the model discussed in Ref. [58] has a global $SU(2)_L \times SU(2)_R \times U(1)_X$, but there are only gauge bosons for $SU(2)_L \times U(1)_Y$. In order for the global symmetry to be exact, the fermions need to be embedded in representations of $SU(2)_L \times SU(2)_R \times U(1)_X$. In this paper, the left-handed top quark is embedded into a $SU(2)_L \times SU(2)_R$ bi-doublet with new quantum number $X = 2/3$,

$$Q_L = \begin{pmatrix} T & T_{5/3} \\ B & T_{2/3} \end{pmatrix} . \tag{2.26}$$

The heavy top partner with electric charge 5/3 decays into a bottom quark by radiating off two W-bosons, $T_{5/3} \to W^-t \to W^-W^-b$. If it is pair-produced one expects final states with four or more final state leptons and jets. Cleaner final states with multiple leptons result from the decay of the heavy double charged partners of the leptons [59].

Supersymmetric Particles

In SUSY models without R parity, the lightest supersymmetric particle (LSP) is not stable and decays into Standard Model final states. If it is a neutralino, it can decay

into the same final states as the heavy neutrinos discussed above, but could also be buried in jets, depending on its couplings [60]. If R parity is violated, the lightest supersymmetric particle must no longer be neutral. It could be a slepton[11] which has to decay into charged lepton final states. In the model described in Ref. [20] for example, the LSP is the stau with a decay chain that has three final state leptons.

11 The supersymmetric particles are always named like their Standard Model partner, but with an additional "s" in front.

PDF-XChange Editor
Click to BUY NOW!
tracker-software.com

PDF-XChange Editor
Click to BUY NOW!
tracker-software.com

Part II

EXPERIMENT AND SIMULATION

PDF-XChange Editor
Click to BUY NOW!
tracker-software.com

3

THE LARGE HADRON COLLIDER AND THE ATLAS EXPERIMENT

In this chapter, the Large Hadron Collider (LHC) and the associated experiments will be briefly described. The ATLAS[1] detector, with all important components relevant for the analyses will be introduced. Also the way how data is collected and processed at ATLAS and how the luminosity is determined is described in this section.

3.1 LARGE HADRON COLLIDER

The Large Hadron Collider (LHC) is a two-ring superconducting hadron accelerator and collider which was built and is operated by the European Organization for Nuclear Research (CERN[2]). The accelerator is placed in a tunnel below the border of Switzerland and France. This tunnel with a length of 26.7 km and a diameter of 3.7 m was originally constructed between 1984 and 1989 for the LEP[3] collider and lies between 45 m and 170 m below the surface.
The LHC is designed for proton-proton collisions[4] at a center of mass energy of $\sqrt{s} = 14\,\text{TeV}$ and a luminosity of $\mathcal{L} = 10^{34}\text{cm}^{-2}\text{s}^{-1}$. In 2010 and 2011, the LHC was running at $\sqrt{s} = 7\,\text{TeV}$ and with a peak luminosity of $\mathcal{L} = 3.7 \times 10^{33}\text{cm}^{-2}\text{s}^{-1}$. In 2012, the center of mass energy was increased to 8 TeV, and a peak luminosity of $\mathcal{L} = 7.7 \times 10^{33}\text{cm}^{-2}\text{s}^{-1}$ was reached, which is already close to the design luminosity. After a two year shutdown, it is planned to have collisions in 2015 at a center of mass energy of 13 TeV.
The injection chain which pre-accelerates the protons to an energy of 450 GeV is built in several steps. In this chain, the old accelerators PS[5] and SPS[6] are re-used. In the LHC the protons get accelerated to the final energy, which takes about 30 min. After that, another 20 min are needed to perform stability tests of the beams and prepare them for physics collisions. The number of protons in each beam decreases with time due to beam collisions and beam self-interactions. After approximately 15 hours the instantaneous luminosity is so low, that it is more efficient to dump the beams and start a new

1 **A** **T**oridal **L**HC **A**pparatu**S**
2 The acronym CERN stands for the name of the council (Conseil Européen pour la Recherche Nucléaire) which was assigned with the founding of the organization.
3 The **L**arge **E**lectron **P**ositron Collider was an electron-positron accelerator operating with a center of mass between 90 GeV and 209 GeV.
4 Alternatively also heavy ions (usually lead ions) are accelerated, but these collisions are not described further in this work.
5 The **P**roton **S**ynchrotron is the oldest major particle accelerator at CERN, operating since 1959.
6 The **S**uper **P**roton **S**ynchrotron (SPS) was starting operating 1976. Between 1981 and 1984 the SPS operated as a proton–antiproton collider (as such it was called SppS) and provided the data for the discovery of the W and Z bosons.

filling.
Figure 3.1 shows the LHC with the four major experiments and the injection chain.

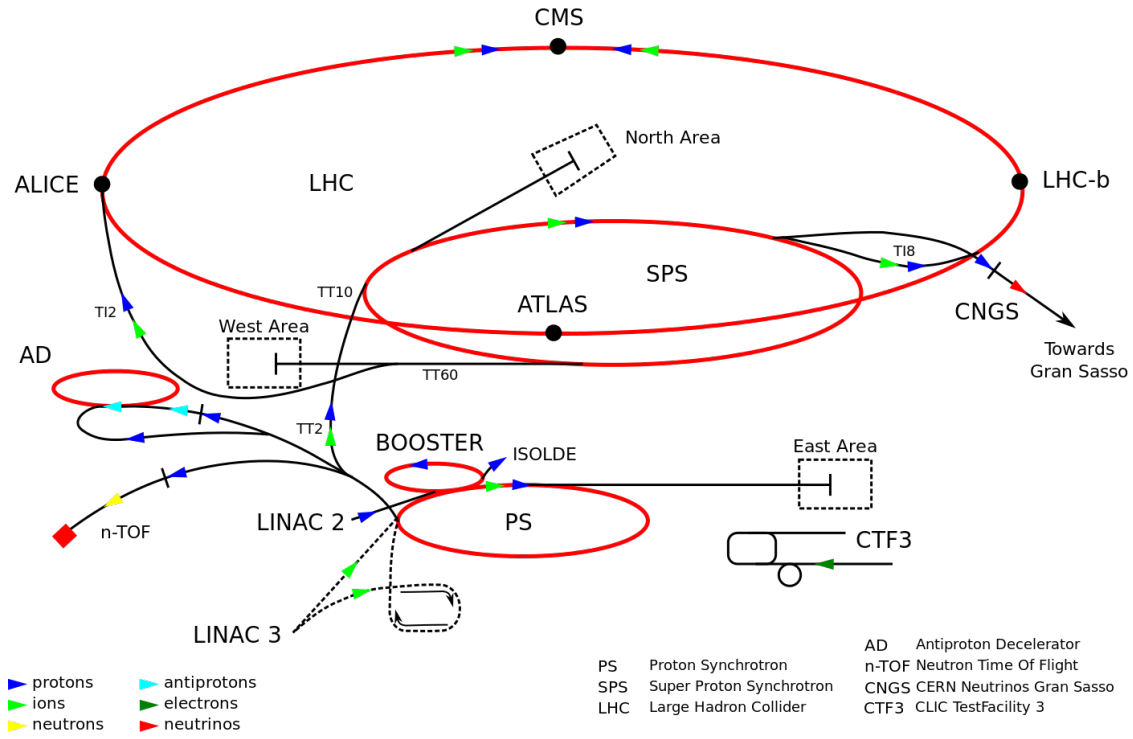

Figure 3.1: The LHC with its experiments and the injector complex [61].

3.1.1 *Experiments at the LHC*

Besides the ATLAS detector [62], which will be described in detail in the next section, there are three other major and three smaller experiments probing the collisions at the LHC. The CMS[7] [63] and the ATLAS experiments are multi-purpose particle detectors. LHCb[8] [64] is a specialized bottom-physics experiment that measures the parameters of CP violation in the interactions of bottom hadrons. The ALICE[9] experiment [65] is optimized to study heavy-ion collisions. LHCf[10] [66] and TOTEM[11] [67] are both small detectors designed to study particles in the region close to the beam pipe of collisions. The former shares the interaction point with the ATLAS experiment, the latter with the CMS detector. The MoEDAL experiment[12] searches for magnetic monopoles and stable massive particles and shares the cavern with LHCb.

7 **C**ompact **M**uon **S**olenoid
8 **L**arge **H**adron **C**ollider **b**eauty
9 **A** **L**arge **I**on **C**ollider **E**xperiment
10 **L**arge **H**adron **C**ollider **f**orward
11 **Tot**al **E**lastic and Diffractive Cross Section **M**easurement
12 **Mo**nopole and **E**xotics **D**etector **a**t the **L**HC

3.2 THE ATLAS DETECTOR

The ATLAS detector is a general purpose detector and was built to probe proton-proton and heavy ion collisions. With a length of 45 m, a diameter of 22 m and a weight of 7000 tons, it is the largest detector at the LHC. In Figure 3.2 a cut-away view of the ATLAS detector is shown.

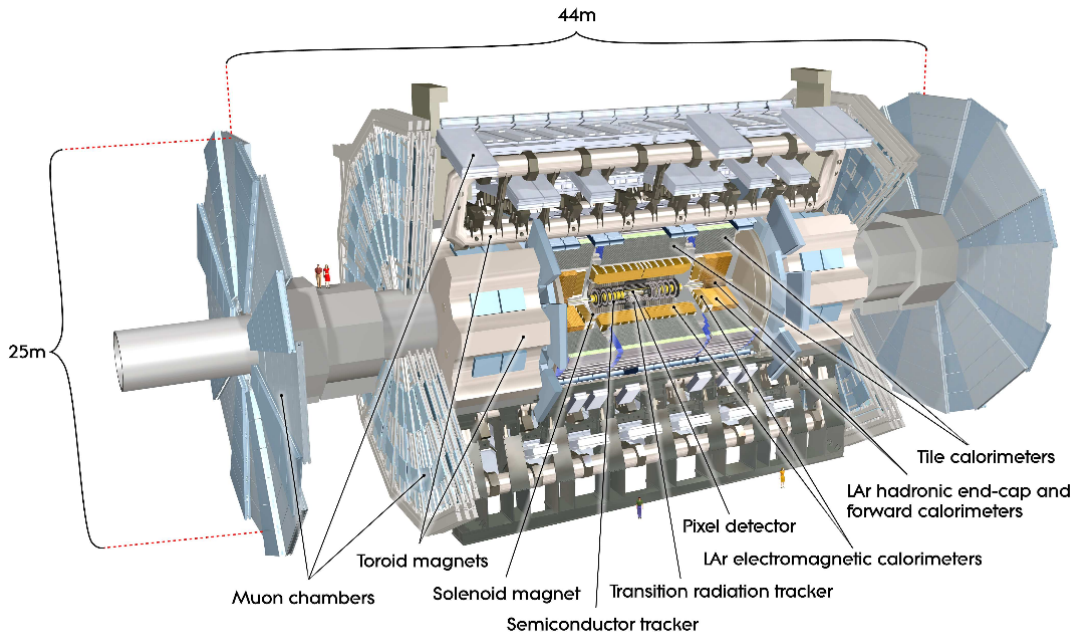

Figure 3.2: Cut-away view of the ATLAS detector [62]. The two persons on the left side are included to give a better idea of the dimension of the detector.

The detector consists of four major components which are placed concentrically around the beam pipe. The components are the inner detector with the tracking system[13], the calorimeters[14], the muon system, and the magnet system. The components which are important for the two analyses of this thesis will be described in detail in the following sections.

3.2.1 *The Coordinate System of ATLAS*

The coordinate system in the ATLAS detector is defined with its origin in the center of the detector. The z-axis is defined as the axis along the beam pipe and the x-axis points towards the center of the accelerator-ring. Together with the y-axis which points upwards to the surface, they form a right-handed Cartesian coordinate system. The azimuthal angle ϕ is defined around the beam pipe in the x-y plane. The range of ϕ is going from $-\pi$ to π with $\phi = 0$ pointing along the direction of the x-axis. Hence, the upper half of the detector is described by positive values of ϕ (0 to π) and the lower half by negative ϕ values ($-\pi$ to 0). Instead of the polar angle θ the pseudorapidity η is usually used which is defined as $\eta = -\ln(\tan\theta/2)$. For massless particles it is

13 This includes the pixel detector, semiconductor tracker and the transition radiation tracker.
14 Electromagnetic calorimeter and hadronic calorimeter.

numerically close to the rapidity $y = \frac{1}{2} \ln\left(\frac{E+p_z}{E-p_z}\right)$, where E is the energy and p_z the z component of the momentum. This is a valid approximation for electrons and positrons. The difference of the rapidity Δy of two particles is invariant under a Lorentz boost along the z-axis [68]. The particle production rate is nearly constant as a function of the pseudorapidity.
The parameter $\Delta R = \sqrt{\Delta\eta^2 + \Delta\phi^2}$ is used to describe the distance between two objects in the η-ϕ plane.

3.2.2 *Definition of* p_T, E_T *and* E_T^{miss}

The transverse momentum $p_T = \sqrt{p_x^2 + p_y^2}$, the transverse energy $E_T = \sqrt{p_T^2 + m^2}$ and the missing transverse energy E_T^{miss} are measured in the x-y plane. For massless particles p_T and E_T are the same. Particles such as the Standard Model neutrino are not directly detectable with the detector and are only indicated by missing energy due to energy conservation. In hadron colliders the energy of the colliding partons is not known, however the transverse energy of the initial partons traveling along the z-axis has to be approximately zero. Therefore the missing transverse energy, which is defined as $E_T^{miss} = \left|\vec{p}_T^{miss}\right|$, where $\vec{p}_T^{miss}$ is the negative vector sum of the transverse momenta of all reconstructed particles $\vec{p}_T^{miss} = -\sum_i \vec{p}_{T,i}^{rec}$ can be used.

3.2.3 *The Inner Detector*

The inner detector is the innermost part of the ATLAS detector. Figure 3.3 shows the components of this sub-detector.

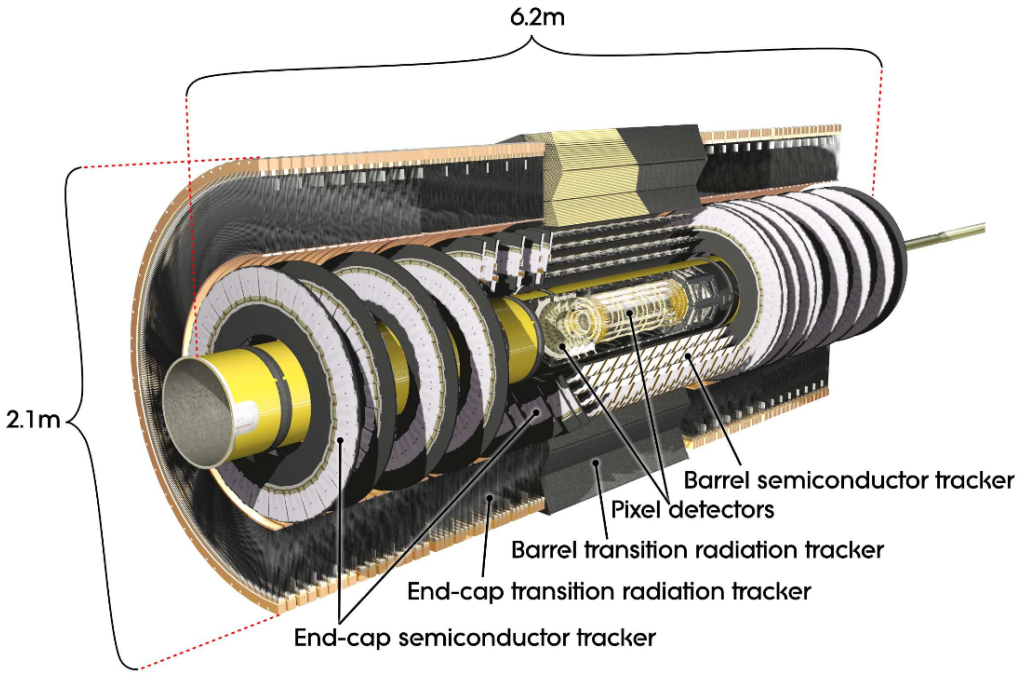

Figure 3.3: Cut-away view of the ATLAS inner detector [62].

The inner detector is divided into three different subsystems. Closest to the beam pipe, there is the pixel detector which is used to reconstruct the interaction point (primary vertex) and possible secondary vertices, which indicate long-lived particles such as bottom quarks. The other two components are the semiconductor tracker (SCT) and the transition radiation tracker (TRT). The pixel- and the SCT-detector are covering a range of $|\eta| < 2.5$, while the TRT-detector ends at $|\eta| = 2.0$. The exact functionality and the setup of these sub-detectors is described in the following. The resolution of the complete tracking system is $\sigma_{p_T}/p_T = 0.05\%\, p_T \oplus 1\%$ [62].

Pixel Detector
The pixel detector is a semiconductor detector made of silicon and is the innermost part of the tracking system. With a length of 1.3 m, a diameter of 34 cm and a weight of 4.4 kg, it is the smallest component of the ATLAS detector. It is built of three cylindric pixel-layers in the barrel region and three discs in the more forward region. The layers in the central region are around 5, 9 and 12 cm away from the beam pipe and have a length of 80 cm. The discs are placed in a distance of 50, 58 and 65 cm from the interaction point. The radii of the discs are between 9 cm and 15 cm. The complete pixel detector is built out of 1744 modules, which have around 47000 pixels each. Together this gives around 80 million readout-channels. The resolution of the pixel detector system is around 12 µm in the x-y plane and 100 µm along the z-axis.

SCT Detector
The semiconductor tracker (SCT) is build out of eight silicon-strip modules in the central region. The intrinsic accuracies of these modules is 17 µm radial to the beam and 580 µm along the beam-axis. To get a better spatial resolution in R-ϕ and R[15], half of the strips are distorted at an angle of 40 mrad. There are also additional discs for the SCT in the forward region, which are perpendicular to the beam pipe. These discs have the same resolution as the modules in the barrel region. The total number of readout channels in the SCT is approximately 6.3 million.

TRT Straw Tubes
The transition radiation tracker (TRT) is the outermost component of the tracking system. It is built out of straw tubes with a diameter of 4 mm and provides coverage up to $|\eta| = 2.0$. The TRT barrel only provides information in the x-y plane with a position resolution of 130 µm per straw. In the central region, the straw tubes have a length of 144 cm and 73 straws are mounted parallel to the beam axis. In the endcap region 160 straw planes with a length of 37 cm are arranged perpendicular to the beam axis. The total number of readout channels of the TRT is approximately 3.5×10^5. The space between successive straw tubes is filled with layers of 15 µm thick polypropylene radiator foils. Electrons and positrons traveling through the foils produce transition-radiation photons which have wavelengths with energies typically of the order of 5 to 15 keV. In the Xenon-based gas mixture of the straw tubes, these photons are detected. Therefore, the electron and positron identification capability is enhanced in the region covered by the TRT detector.

15 R is the distance from the beam-axis in cylinder coordinates.

The inner detector is surrounded by a superconducting solenoid, which leads to a homogeneous magnetic field of two Tesla within the detector. Charged particles, traveling through the inner detector, will describe a circular trajectory due to the electromagnetic force. The transverse momentum (p_T) and the charge (q) of the particle are related to the radius (ρ) of the circle using the relation

$$p_T[\mathrm{GeV}] = \rho[\mathrm{mm}] \cdot 3 \times 10^{-4} \cdot q[e] \cdot B[\mathrm{T}]\,, \tag{3.1}$$

with the assumption that the magnetic field B is homogeneous parallel to the beam-axis.

3.2.4 *Calorimeter*

The calorimeter of the ATLAS detector is a sampling calorimeter with alternating layers of passive and active material. All particles interact with the passive material when passing through the calorimeter. The interaction cross-section of neutrinos is so small that a direct detection is almost impossible. Instead, they are reconstructed with help of the missing transverse energy as described in Section 3.2.2. In the passive layers, the incident particles (electrons, positrons, photons and hadrons) lead to particle showers. The deposited energy of these showers, which are also called clusters, can be measured in the active layers. This gives the information about the energy of the incident particles. Since there is a large difference between the energy deposition of electromagnetic and hadronic particles, there are two different calorimeters. One for electron, positrons and photons and another for hadrons. In addition, there is a third calorimeter in the forward region of the detector, where the first layer is used as electromagnetic calorimeter and and the second and third layer as hadronic calorimeter. Figure 3.4 shows a cut-away view of the ATLAS calorimeter.

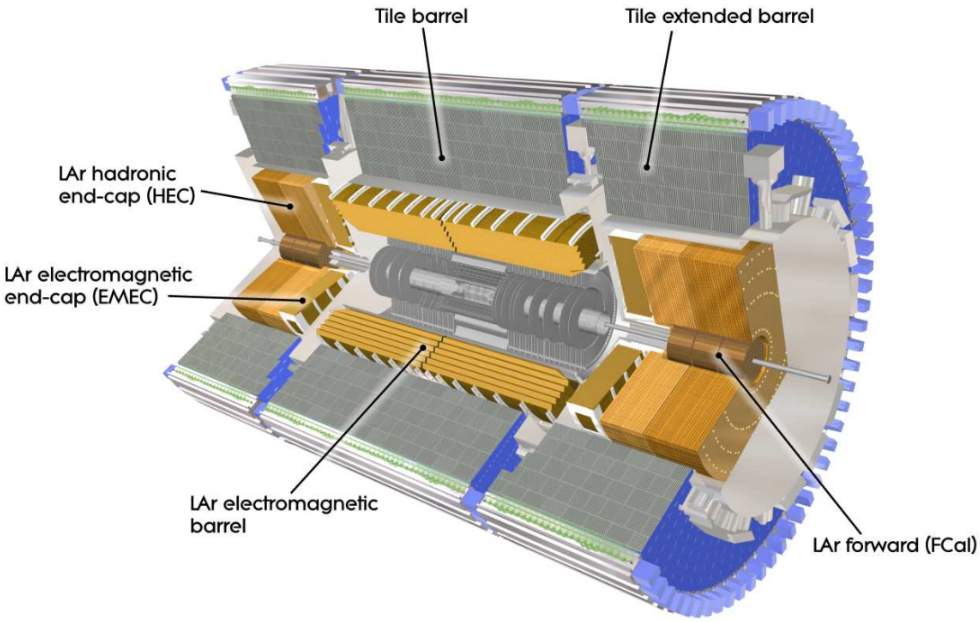

Figure 3.4: Cut-away view of the ATLAS calorimeter [62].

The orange colored region is the electromagnetic calorimeter, the gray area is the hadronic calorimeter and the the forward calorimeter (FCAL) is shown in brown. The different calorimeters will be discussed in the following.

Electromagnetic Calorimeter

In the electromagnetic calorimeter, the particles interact electromagnetically. The dominant processes for high energy particles (above 10 MeV) are pair production and Bremsstrahlung. Photons pair produces electrons and positrons, while in case of electrons or positrons photons are radiated via Bremsstrahlung. This leads to a shower of electrons, positrons, and photons which are stopped by ionization. The energy of the initial electron or positron E_0 decreases exponentially until it is completely stopped with $E(x) = E_0 e^{-x/X_0}$, were X_0 is the material dependent parameter called radiation length.

The electromagentic calorimeter covered a range of $|\eta| < 3.2$ and is separated into a barrel part ($|\eta| < 1.475$) and two end-cap components ($1.375 < |\eta| < 3.2$). The barrel and the two end-caps are build of the same materials. They are made of 1.9 mm thick lead absorber plates, with a stainless steel surface coating. Between the plates, liquid Argon (LAr) is used as active medium. Liquid Argon has a linear behavior, a stable response and radiation hardness and is therefore a very good choice. The absorber plates and the electrodes are ordered in an accordion geometry. This geometry provides naturally a full coverage in Φ without any crack and allows a fast extraction of the signal at the rear or at the front of the electrodes. Particles traveling through the LAr produce ionization electrons which will drift to the electrodes. The measured electric current at the electrodes is proportional to the deposited energy in the calorimeter.

Figure 3.5 shows the different layers and the granularity of the electromagnetic calorimeter.

In the central region, the calorimeter has three layers with different cell size. Each layer is designed and used for a different function. In the first layer, the cells have a size of $\eta \times \phi = 0.0031 \times 0.982$. This gives a very precise shower-resolution in η, which is important for the suppression of neutral pions ($\pi^0 \to \gamma\gamma$). The second layer is used to estimate the exact position of the particle and should absorb most of the energy of electrons, positrons and photons. In this layer, the size of a single cell is 0.025×0.0245. The third layer is in the boarder area of the hadronic calorimeter with a cell size of 0.050×0.0245. These cells are used to correct the energy if the shower has passed the sensitive part of the calorimeter. The complete electromagnetic calorimeter has a thickness between $22X_0$ and $33X_0$, while the second layer is at least $16X_0$ thick. This ensures that electron, positrons, and photons mostly lose their complete energy within the electromagnetic calorimeter.

The granularity and functionality in both end-caps of the calorimeter is compatible with the central region. In the transition region ($1.52 < |\eta| < 2.47$) and in the region which is not covered by the tracking system ($2.47 < |\eta| < 3.2$), the calorimeter consists only of two layers. In this region, the functionality of the first and second layer are merged. Most of the energy of an electromagnetic shower is deposited in the first layer and the second layer is used for energy corrections.

A presampler detector with one active LAr layer is mounted in front of the electromagnetic calorimeter in the region $|\eta| < 1.8$. With a thickness of 1.1 cm (0.5 cm)

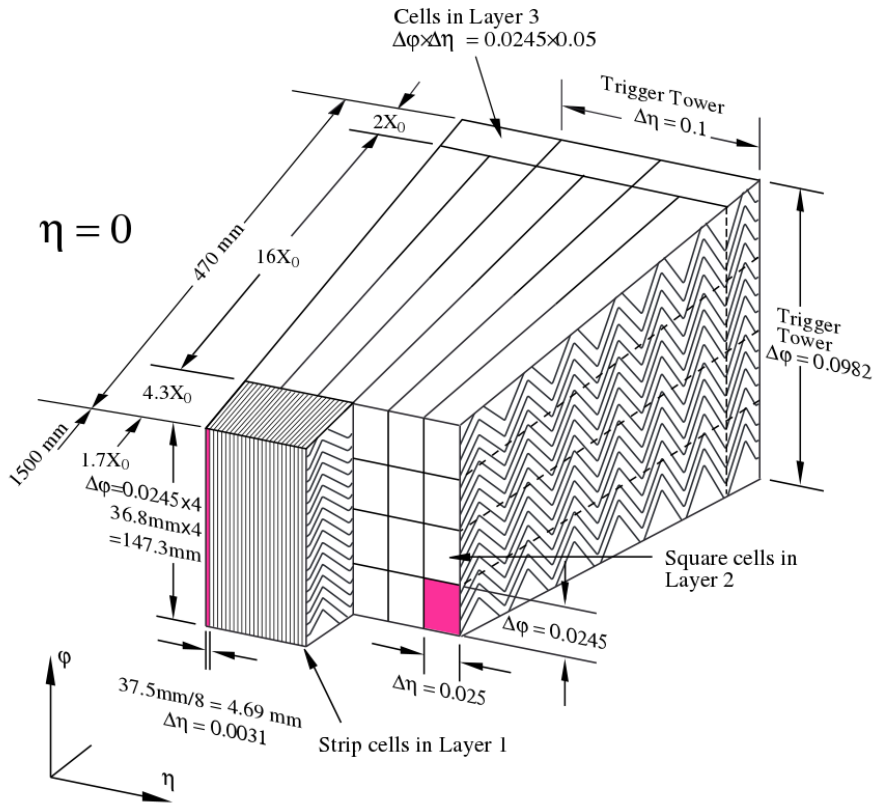

Figure 3.5: Sketch of a barrel module of the electromagentic calorimeter, where the different layers are clearly visible with the of electrodes in ϕ. The granularity in η and ϕ of the cells of each of the three layers is shown [62].

for the barrel (end-cap) region, it is used to correct for the energy lost by electrons, positrons, and photons upstream of the calorimeter.
There are around 190 thousand readout cells in the complete electromagnetic calorimeter, each having an individual readout electronic. The energy resolution of the electromagnetic calorimeter is $\sigma_E/E = 10\%/\sqrt{E\,[\mathrm{GeV}]} \oplus 0.7\%$ [62].

Hadronic Calorimeter

In the hadronic calorimeter, the showering is dominated by a succession of inelastic hadronic interactions via the strong force. A characteristic quantity for the length of the hadronic shower is the nuclear interaction length λ, which is a material dependent parameter. After one interaction length the energy of the shower is reduced by a factor of $1/e$.
The hadronic calorimeter is a sampling calorimeter which is divided into three parts. The barrel covers the region $|\eta| < 0.8$ and its two extended barrels for each side $0.8 < |\eta| < 1.7$. In addition, there is an end-cap calorimeter on each side of the detector covering the more forward region ($1.7 < |\eta| < 3.2$). In the barrel and the extended barrel region, steel is used as an absorber and scintillating tiles as active material. The central region is segmented into three layers in depth, which are approximately 1.5, 4.1 and 1.8 interaction lengths (λ) thick for the barrel and 1.5, 2.6 and 4.4 λ for the extended barrel.

The hadronic end-cap calorimeter (HEC) is located on both sides of the detector directly behind the end-cap of the electromagnetic calorimeter sharing the same Liquid Argon (LAr) cryostats. As passive material copper plates with a thickness of 25 mm, for wheels closest to the interaction point, and 50 mm for those further away, are used.
The hadronic calorimeter has a jet energy resolution of $\sigma_E/E = 50\%/\sqrt{E\,[\text{GeV}]} \oplus 3\%$ [62].

Forward Calorimeter
The forward calorimeter (FCAL) is mounted very close to the beam pipe and is integrated into the end-cap cryostats. It covers the region $3.1 < |\eta| < 4.9$ and is used as electromagentic and hadronic calorimeter. The FCAL is approximately ten interaction lengths deep and consists of three modules in each end-cap. The first module made of copper is optimized for electromagentic particles, while the other two are made of tungsten and are designed to measure the energy of hadrons. Each module consists of a metal matrix with liquid argon as active material in the gaps.

3.2.5 *Muon System*

The calorimeter is surrounded by the muon spectrometer which defines the overall dimension of the ATLAS detector. It consists of a superconducting air-core toroid magnet system and tracking chambers. The magnetic field deflects the mouns and their tracks are reconstructed of hits in three layers of high-precision tracking chambers. The muon system has a coverage of $|\eta| = 2.7$ and the resolution is $\sigma_{p_T}/p_T = 10\%$ at $p_T = 1\text{TeV}$ [62]. More information about the muon system can be found in Ref. [69].

3.2.6 *The Trigger System and Data Acquisition*

The three level trigger system of the ATLAS detector and the way how data is acquired is explained in this section. Figure 3.6 shows a block diagram of the trigger and data acquisition (DAQ) system. The trigger system will be described for an electromagnetic object but the procedure is very similar for jets. Muon triggers work slightly different but are beyond the scope of this thesis.
The Level 1 (L1) trigger is hardware based and performs a very fast event selection by using the energy information from the calorimeter with reduced granularity[16] and the muon system. It has about 2.5 µs to make a decision and reduces the event rate from ~ 40 MHz to 75 kHz. Electromagnetic objects are selected if the total transverse energy in two Trigger Towers[17] next to each other is above a certain threshold. Each Trigger Tower has a size of $\Delta\eta \times \Delta\phi = 0.1 \times 0.1$. During the L1 trigger decision, all information from the sub-detectors are stored in buffer pipelines. If the event is accepted by the L1 trigger, the signals are digitized and transferred off the detector to the data acquisition (DAQ) system. The first stage of the DAQ system is the readout system, where the data is received and stored in local buffers. The Level 2 (L2) trigger is seeded by regions of interest (RoI) which are defined by the L1 trigger. The stored data of the RoI's is then subsequently solicited by the L2 trigger system. The L2 trigger is a software based

16 In figure 3.5 the reduced granularity for the electromagnetic calorimeter is marked with "Trigger Tower".
17 For the reduced granularity calorimeter cells are combined to so called Trigger Towers.

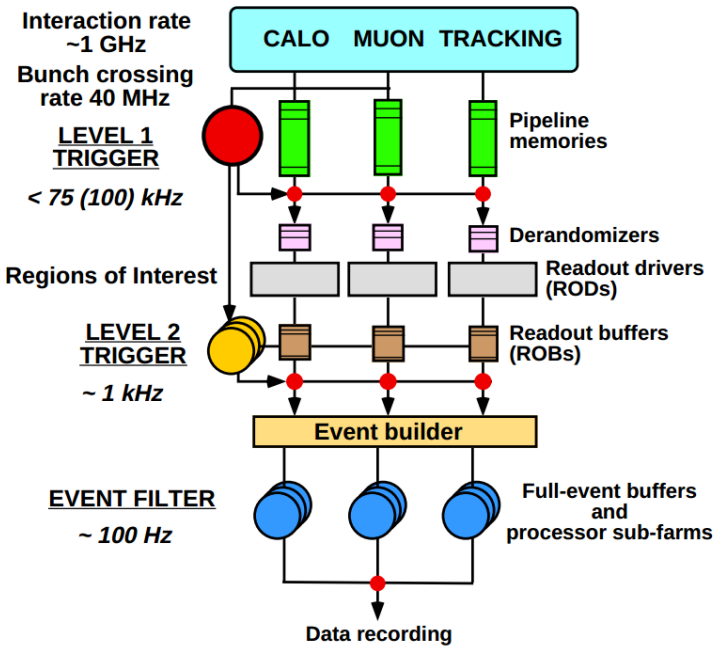

Figure 3.6: Block diagram of the Trigger/DAQ system [70]. On the left side, the typical interaction rate and the data equivalent at the different stages of triggering are shown, while on the right side, the different components of the trigger system are shown schematically.

trigger which uses the full granularity and precision of all detector systems, but only in the RoI which was defined by L1. The L2 trigger has some milliseconds for the decision and reduces the rate to about 3 kHz. The data of events selected by L2 are then transferred to the event-building system and subsequently to the EF for the final decision. This is done by the Event Filter trigger (EF) which is seeded by the decision of the L2 trigger and performs a further reduction to the final rate of 200 Hz. For the decision of the EF, the complete event with all available information is reconstructed. Even some calibrations and corrections are already applied. If at least one EF trigger accepted the event, all information from the single detector components are recorded. The events are sorted with help of the trigger information in different streams. For example the "Egamma" stream which is used in the following analyses contains all events where at least one electron, positron or photon trigger had fired. After a positive decision, all data is moved to a permanent storage (on magnetic tapes) at the CERN computer center.

3.2.7 *Computing*

The further processing is done on the LHC Computing Grid [71]. The grid is a large network of computer clusters which is organized in four levels. These different levels are called "Tiers". The CERN computer center is called Tier-0. This is the point where the reconstruction algorithm and calibrations to the data is applied. The information is transformed on object level in a format called "Event Summary Data", short ESD. Afterwards, the data in ESD format, together with a copy of the raw data (in the Raw

Data Objects (RDOs) format), are distributed all over the world to the Tier-1 centers. This provides a large amount of storage space and also additional processing power, for example for a recalibration of the data. As a next step, Analysis Object Data (AOD) are derived from the ESD. This kind of data contains only information about the different physics objects, like electrons, positrons, photons or jets. From the AODs, a further extraction to the Derived Physics Data (DPD) is done. The DPDs are transfered to Tier-2 centers, where processing power for physics analysis and Monte Carlo production is provided. All data needed for analyses can be copied to local Tier-3 centers. D3PDs, a special type of a DPD, which stores the information in ROOT Ntuples, were used for these analyses. ROOT Ntuples are a commonly used data format in high energy physics. ROOT [72] is an object-oriented program developed by CERN. It provides a large set of packages and libraries which are very helpful in analyzing and visualizing data. All histograms shown in this thesis were produced using ROOT.

3.3 LUMINOSITY DETERMINATION

The luminosity $\mathcal{L}$ is defined as the ratio of the number of detected events N in a certain time t to the interaction cross-section σ.

$$\mathcal{L} = \frac{1}{\sigma}\frac{dN}{dt} \tag{3.2}$$

For a proton-proton collider, such as the LHC, the luminosity can be determined by

$$\mathcal{L} = \frac{R_{inel}}{\sigma_{inel}} = \frac{\mu n_b f_r}{\sigma_{inel}}, \tag{3.3}$$

where the rate of inelastic collisions R_{inel} is expressed by the number of average interactions per bunch crossing μ , the number of bunch pairs colliding per circulation n_b and the circulation frequency f_r. The inelastic proton-proton cross-section is denoted by σ_{inel}. ATLAS monitors delivered luminosity by measuring the observed interaction rate per crossing (μ_{vis}) independently with several detectors. Two of these detectors are LUCID[18] [73] and BCM[19][62]. This measured value μ_{vis} has to be corrected with the efficiency of the detectors and the used algorithm to obtain μ.
This is done with help of so called van der Meer (vdM) scans [74]. The luminosity can expressed in terms of machine parameters as

$$\mathcal{L} = \frac{n_b f_r n_1 n_2}{2\pi \Sigma_x \Sigma_y}, \tag{3.4}$$

where n_1 and n_2 are the number of protons per bunch in beam 1 and beam 2 respectively, and Σ_x and Σ_y characterize the horizontal and vertical convolved beam widths. The parameters Σ_x and Σ_y can be directly measured with a van der Meer (vdM) scan and the number of protons are provided by an external measurement. For the vdM scan, the two beams are separated in steps of a known distance and the beam width is measured. The largest uncertainty contribution is coming from the vdM scan. For 2011

18 **Lu**minosity measurement using **C**herenkov **I**ntegrating **D**etector
19 The ATLAS **B**eam **C**onditions **M**onitor

PDF-XChange Editor
Click to BUY NOW!
tracker-software.com

ATLAS was able to determine the luminosity with an uncertainty of 1.8% and for 2012 the uncertainty was 2.8%. For more information about the luminosity measurement at ATLAS and how the uncertainties were estimated, see Ref. [75].

4

ELECTRONS IN ATLAS

Further on electrons refers to electrons and positrons if not explicitly mentioned otherwise. In a particle detector such as the ATLAS detector, it is not possible to directly identify particles like electrons, other fermions or hadrons. Only energy depositions in the calorimeters and hits in the silicon and TRT detectors are recorded. With help of these signatures, it is possible to reconstruct electron candidate objects. Further cuts on, e.g. the shape of the energy deposition or the number of hits used for the track reconstruction are used to distinguish between real electrons and fake signatures[1]. How this is done is subject of this chapter.

4.1 RECONSTRUCTION

At ATLAS, there are three different algorithms used to reconstruct electron objects. Two possibilities to reconstruct electron candidates in the central region ($|\eta| < 2.47$) of the detector and one algorithm for electron candidates in the forward region ($2.5 < |\eta| < 4.9$).

Central Electrons
For the central region of the detector, there are two different methods available to reconstruct an electron candidate: the standard algorithm and the so-called "soft" reconstruction algorithm. The latter one was not used for this analysis and is only mentioned for the sake of completeness.
The standard algorithm starts from an energy deposition in the electromagnetic calorimeter and is looking for an associated reconstructed track, pointing to the calorimeter cluster. The electromagnetic cluster is built by using a sliding-window algorithm [62]: Calorimeter cells are summed up to a granularity of size $\Delta\eta \times \Delta\phi = 0.025 \times 0.025$. In this matrix, the algorithm is searching with a window size of 3 x 5 in units of the matrix elements for an energy deposition with a transverse momentum larger than 2.5 GeV. The efficiency of the initial cluster reconstruction was found to be almost 100% for electrons with $E_T > 20$ GeV [76].
Track reconstruction: The information from the hits in the inner detector by converting them into three dimensional space points is used to reconstruct tracks. Two successive hits in the pixel detector are used for the seed of a track. Additional space points from the area where the seed is pointing to are added up successively. After each added point a fit with a parametrized track function is performed to judge whether the track is compatible with a particle trajectory. This is done for all space points in the silicon detector and afterwards the track reconstruction is extrapolated

1 Signatures which are reconstructed as electrons but are in reality other particles.

to the TRT detector which only provides information in the x-y-plane.
After the track reconstruction is finished, the track is extrapolated to the middle layer of the electromagnetic calorimeter. The extrapolated η and ϕ coordinates of the track are then compared to the position of the seed cluster position in this layer. If the track impact point and the electromagnetic cluster position is within $|\Delta R|^2 < 0.05$, the track and the cluster are considered as matched. If there is more than one track within the $|\Delta R| < 0.05$, the one with the smallest $|\Delta R|$ is taken into account. Without a matching track, the candidate is rejected.
After a successful cluster-track matching, the size of the cluster is optimized to get a better description of the energy distribution in the different regions of the calorimeter. The size of the cluster seed is enlarged to 3×7 (5×5) for the barrel (endcap) region of the detector. To determine the total energy of the electron candidate from this cluster, three other effects are taken into account: the estimated energy deposition in material in front of the electromagnetic calorimeter, the estimated energy deposition outside the cluster (lateral leakage) and the estimated energy deposition beyond the electromagnetic calorimeter (longitudinal leakage). Also some offline calibration corrections are applied, which are discussed below.
The three-momentum of an electron candidate in the central region is derived using the energy as described above and the measured η and ϕ position. The geometric values are taken from the track measurement because of the better resolution. In this context, the electrons are treated as massless particles. It is not possible to resolve the mass of the electrons (511 keV) with the ATLAS detector and all other energies considered in this analysis are on the order of GeV. Therefore, the mass of the electrons is negligible.

Forward Electrons

The forward region of the detector is not covered by the tracking system of the inner detector. Therefore, only information from the inner wheel of the electromagnetic endcap calorimeter and from the forward calorimeter are available. This allows no distinction between electrons and photons and also no information about the charge of the particle is available. The energy clustering in the forward region is done by using a topological clustering algorithm [77]: Starting from a seed cell[3], all cells with an energy deposition, which is significantly above the noise threshold, are added up in a iterative way in all three dimensions. There is no limit on the number of corresponding cells and the energy of the cluster is defined as the sum of all cells. Corrections to the energy are applied for the energy loss due to passive material in front of the calorimeter.
An electron candidate is reconstructed if the transverse energy (E_T) is larger than 5 GeV and the energy component in the hadronic calorimeter is small. The geometric values of the reconstructed electron candidate are given by the barycenter of the cluster.
Due to the absence of tracking information in the forward region, the three-momentum of the electron candidate is derived by using the energy and position information of the calorimeter cluster.

2 $\Delta R = \sqrt{\Delta\eta^2 + \Delta\phi^2}$.
3 The energy deposition in this cell needs to be above a rather high signal over noise ratio threshold.

PDF-XChange Editor Click to BUY NOW! tracker-software.com

4.2 IDENTIFICATION CRITERIA

The identification criteria for central and forward electrons will be discussed in this section.

Central Electrons

For the central detector region, there are three reference sets defined, labeled with *loose, medium* and *tight*. They provide increasing background suppression power at cost of signal efficiency. The reference sets are defined in a way that the signal efficiency is ~ 90% for loose, ~ 80% for medium and ~ 70% for tight. The loose selection increases the rejection of hadronic background by a factor of ~ 5 with respect to the reconstruction level. The medium set increases the background rejection by an order of magnitude with respect to loose and tight by a factor of two with respect to medium. The identification criteria are based on cuts on cluster, track, and on combined track-cluster variables which are described in Table 4.1. All cuts used for loose are also part of the medium selection and all cuts used for medium are also part of the tight selection. The different identification criteria are binned in eleven p_T bins and ten bins of cluster-η.

For 2011 and 2012, the same set of variables were used with only small changes for the b-layer cut which is indicated in the table. With increased center of mass energy and higher instantaneous luminosity in 2012, the background contribution becomes larger due to more pile-up. Therefore most of the p_T and η dependent cuts were tightened with respect to 2011 to stay with the same signal efficiency.

Forward Electrons

As for the central region, three reference sets of selection criteria are defined in the forward region. They are also called *loose, medium and tight*, but a prefix fwd- will be applied to be able to distinguish them from the central ones. All three reference sets use the same six variables, which are defined in Table 4.2, but with increasing background rejection power. This is done by tighter cut requirements for each set. To define *fwd-loose, fwd-medium* and *fwd-tight*, a multivariate method using a fisher discriminant was used.

To consider the significantly harsher pileup conditions at high η, the identification criteria are not only binned in nine cluster-η bins (six bins in the endcap of the electromagnetic calorimeter ($2.5 < |\eta| < 3.16$)) and three in the forward calorimeter ($3.35 < |\eta| < 4.9$), but also in four bins of number of primary vertices[4] (N_{PV}). The transition region between the electromagnetic and forward calorimeter ($3.16 < |\eta| < 3.35$) is not well-described and will be neglected for all further studies. However, no explicit dependence on the transverse momentum is introduced as the dependence was found to be small.

4.3 ELECTRON ENERGY CORRECTION

The measured energy in the electromagnetic calorimeter is not the true energy of the electrons. Therefore, a final calibration after the reconstruction is needed. A calibration factor α_i is defined which corrects for this effect. Different values of α_i for different

4 The number of primary vertices is a good parameter to describe the pileup conditions.

Table 4.1: Selection and variables used in the loose, medium and tight electron identification criteria in the central region of the detector ($|\eta| < 2.47$) [78].

Category	Description	Variable
	loose	
Hadronic leakage	Ratio of E_T in the first layer of the hadronic calorimeter ($|\eta| < 0.8$ or $|\eta| > 1.37$) or E_T in whole hadronic calorimeter ($|\eta| > 0.8$ and $|\eta| < 1.37$) to E_T of the EM cluster	$R_{had,1}$, R_{had}
Middle layer of the EM	Ratio of the energy deposition in 3 x 7 cells to 7 x 7 cells	R_η
	Lateral width of the shower	w_{η^2}
Front layer of the EM	Total shower width	w_{stot}
	Energy difference associated with the largest and second largest energy deposition in the cluster devided by their sum	E_{ratio}
Track quality and track-cluster matching	Number of hits in the pixel detector ($\geqslant 1$)	
	Number of hits in the silicon (pixel + SCT) detectors ($\geqslant 7$)	
	$|\Delta\eta|$ between the cluster position in the first layer and the extrapolated track ($\Delta|\eta_1| < 0.015$)	Δ_{η_1}
	medium (includes loose)	
Track quality and track-cluster matching	Number of hits in the b-layer > 0 for $|\eta| < 2.01$ (2011)	
	Number of hits in the b-layer > 0 for $|\eta| < 2.37$ (2012)	
	Number of hits in the pixel detector > 1 for $|\eta| > 2.01$ (2011)	
	Transverse impact parameter $|d_0| < 5$ mm	d_0
	Tighter $|\Delta_{\eta_1}|$ cut (< 0.005)	
TRT	Loose cut on TRT high-threshold fraction	
	tight (includes medium)	
Track quality and track-cluster matching	Tighter transverse impact parameter cut ($|d_0| < 1$ mm)	
	Asymmetric cut on $\Delta\phi$ between the cluster position in the middle layer and the extrapolated track	$\Delta\phi$
	Ratio of the cluster energy to the track momentum	E/p
TRT	Total number of hits in the TRT	
	Tighter cut on the TRT high-threshold fraction	
Conversions	Reject electron candidates matched to reconstructed photon conversions	

η regions are provided by an internal group of ATLAS [79]. The energy correction is applied with the relation $E_{new} = E_{old}/(1 - \alpha_i)$ to each electron separately and the new transverse momentum is calculated using $p_T = E_{new}/\cosh(\eta_{track})$, where η_{track} is the pseudorapidity of the electron extracted from the tracking system. The correction α_i was estimated by comparing the Z and J/Ψ resonance in data and Monte Carlo simulation and is less than one percent.

Table 4.2: Variables used to identify electrons in the forward region of the detector ($2.5 < |\eta| < 4.9$) [78].

Category	Description	Variable
Shower depth	Distance of the shower barycenter from the calorimeter front face measured along the shower axis	λ_{centre}
Maximum cell energy	Fraction of cluster energy in the most energetic cell	f_{max}
Longitudinal second moment	Second moment of the distance of each cell to the shower center in the longitudinal direction (λ_i)	$\langle \lambda^2 \rangle$
Transverse second moment	Second moment of the distance of each cell to the shower center in the transverse direction (r_i)	$\langle r^2 \rangle$
Normalized lateral moment	lat_2 and lat_{max} are second moments of r_i for different weights per cell	$\frac{lat_2}{lat_2+lat_{max}}$
Normalized longitudinal moment	$long_2$ and $long_{max}$ are second moments of λ_i for different weights per cell	$\frac{long_2}{long_2+long_{max}}$

PDF-XChange Editor
Click to BUY NOW!
tracker-software.com

5

MONTE CARLO SIMULATION OF PSEUDO DATA

For high energy particle physics it is very important to have a solid computer-based method to simulate known or theoretically predicted physical processes. Goal of these simulations is to get a set of pseudo data which is comparable to data collected with a detector. The simulation is divided into two parts. On the one hand, the event generation where the physical process is simulated independent of the detector. This stage is called generator level. On the other hand, the detector simulation which simulates the way of the generated particles through the detector and the interaction with the detector. After this stage, the events are reconstructed using the same algorithms as for real data (For electrons this is described in detail in Chapter 4).
The description of the different generators for the physical processes and the detector simulation is part of this chapter. Furthermore, the corrections which were applied to the samples used in this thesis are presented.

5.1 EVENT GENERATION WITH MONTE CARLO GENERATORS

The simulation of a interaction process is described by generators and can be divided into five parts which are the hard process, the parton shower, the hadronization, the underlying event, and the decay of unstable particles. A schematic drawing of the event generation is shown in Figure 5.1.
In the first part, the matrix element of the hard process is calculated and the probability of the hard scatter process is derived from perturbation theory. To get the final probability, the result is convoluted with the PDFs of the incoming partons. Afterwards, the four-vectors of the out-coming particles can be determined. This is done with a random number generator and is the reason why these programs are called Monte Carlo generators.
As next step, the gluons, radiated from the incoming and outcoming colored particles[1], are simulated. For incoming particles this is called initial state radiation (ISR) and for outcoming particles final state radiation (FSR). These gluons can then split into $q\bar{q}$-pairs or radiate further gluons, and so on. This process is called parton shower and is simulated as a sequential step-by-step process, starting from the momentum transfer scale of the hard process, downwards to lower momentum scales until the perturbation theory breaks down at around 1 GeV. The emission of real photons of the outcoming particles (FSR) is simulated using the program PHOTOS [81].
At the point where the perturbation theory breaks down, it is necessary to switch to a hadronization model. This model takes care of the confinement and turns the system

1 These are gluons and quarks.

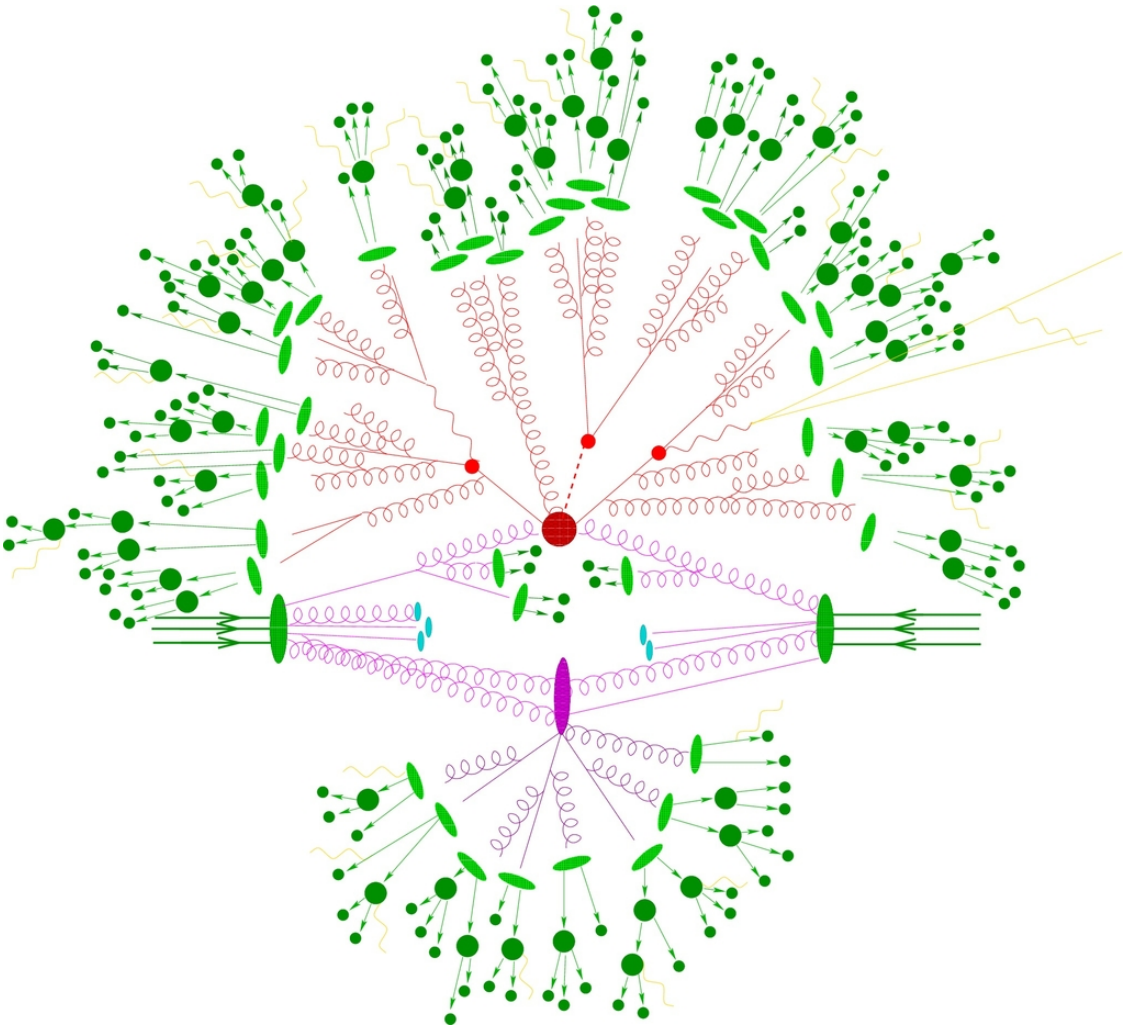

Figure 5.1: Diagram showing the different stages involved in the event generation. The hard process (red), the parton shower (brown), hadronization (light green), and the decay of unstable particles (dark green) are shown together with the underlying event (purple) [80].

of partons into hadrons. In this stage, it is important that only one colored parton of the uncolored proton was involved in the hard process and the proton has been left in a colored state. In the moment of the collision, both protons are overlapping and there is a very high probability that there will be other interactions by the parton remnants. Everything coming out of these additional interactions is called the underlying event. As last stage of the event generation, the decay of all short living particles into long living particles is simulated. For more information about the Monte Carlo event generation, see Ref. [82].
The generators used for the analyses are the following:

- Pythia [83][84], Herwig [85] and Sherpa [86] are leading order (LO) multi-purpose generators which are able to simulate all of the five steps.

- To generate Monte Carlo samples at next-to-leading order, the POWHEG[2] [87] or the MC@NLO [88] generator were used. These generators are able to calculate the matrix element at NLO, but are specialized for the hard process. The output of these generators is compatible with the LO generators mentioned above and typically combined for the last steps. For these NLO generators, an additional matching between the matrix element and the parton shower is needed, since the matrix element already includes Feynman diagrams for initial and final state radiation.

- ALPGEN [89] is a generator specialized for multiparton hard processes in hadronic collisions. The matrix elements for a large set of parton-level processes, e.g. W-boson production with 0-5 additional jets, is calculated at leading order in QCD and EW interactions.

5.2 DETECTOR SIMULATION WITH GEANT4

In high energy physics, the physical processes can only be studied with the help of a detector. No direct information of the hard process is available. Therefore, it is crucial to have a very precise understanding of the behavior of the detector. The description and simulation of a complex detector such as ATLAS within a software framework is a large challenge and is done with the GEANT4 toolkit [90]. The requirements, which are fulfilled by GEANT4, are the following:

- Description of the ATLAS geometry and its material distribution.
- Tracking of the particles through the detector, considering the magnetic fields.
- Correct handling of the particle interactions with the detector components.
- Simulation of the detector response for active components.
- Provide an event output format which is compatible with the actual detector output (RDO).

As input of the detector simulations the output of an event generator, as described in the last section, is used. The output of the simulation is stored in the Raw Data Objects (RDO) format and can be analyzed by the reconstruction software.
The simulation of the detector is very time-consuming and is the limiting factor for the Monte Carlo production at ATLAS. For example, the full simulation of a single event takes about 19 CPU minutes [91]. The correctness of the implementation of the ATLAS detector in the software was tested with dedicated test beams. Further tests were done by adding additional material in the simulation or an intentional misalignment of detector parts.

5.3 MONTE CARLO CORRECTIONS

Several corrections are applied to the produced Monte Carlo samples to get a better agreement with data events. These corrections include adjustments to the pile-up

2 **Po**sitive **W**eight **H**ardest **E**mmsion **G**enerator

effect, electron momentum resolution and also corrections for inefficiencies of the reconstruction and identification of electrons, as well as for the trigger. These corrections are discussed in more detail below, together with the corrections for higher order cross-sections. Also the reweighting of the transverse momentum of Z^0/γ^* for the 2011 Pythia Drell-Yan Monte Carlo sample is described.

5.3.1 *Pile-Up Reweighting*

In 2011, there was an average of approximately 9 proton-proton interactions per bunch crossing, while in 2012 this number increased to 21. This effect is called pile-up. There are also influences from previous and later bunch crossings, generally known as "out of time pile-up".
The pile-up effect is included in the Monte Carlo samples, but the pile-up conditions in the detector were changing over time[3]. Since the true pile-up conditions in data are unknown during the Monte Carlo production[4], a wide distribution in the number of pile-up collisions per event is used to generate the Monte Carlo events. To adjust the Monte Carlo simulation to fit the data, each event was reweighted using the official reweighting tool, provided by ATLAS. Figure 5.2, shows the distribution of average interactions per bunch crossing (BX) in data, together with the distribution in Monte Carlo before and after the reweighting.

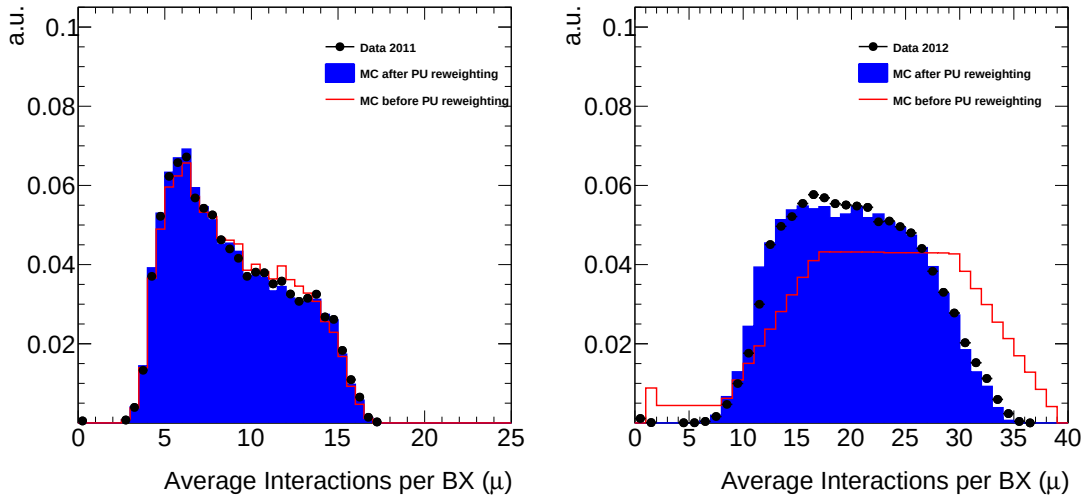

Figure 5.2: Distribution of average interactions per bunch crossing (BX) in the data of 2011 (left) and 2012 (right), together with the distributions of Monte Carlo samples before (blue) and after reweighting (red).

5.3.2 *K-Factors*

The Monte Carlo samples which were used, are generated at leading order (LO) or next-to-leading order (NLO), but the cross-section of the physical processes is known at next-

3 This is strongly dependent on the instantaneous luminosity.
4 Due to the fact that the Monte Carlo production is very time-consuming the samples are normally produced before the start of data taking.

to-leading order (NLO) or even at next-to-next-to-leading order (NNLO). To correct for the higher orders, so-called k-factors are applied to the Monte Carlo samples. For the $pp \to Z/\gamma^* + X \to e^+e^- + X$ process, which is the signal process for the Drell-Yan cross-section measurement, mass dependent k-factors were applied. The k-factors estimated for the PYTHIA and MC@NLO generators are shown in Figure 5.3 and Figure 5.4. For all other samples, flat k-factors were applied which are listed in Table 7.1 in Appendix A for each Monte Carlo sample separately.

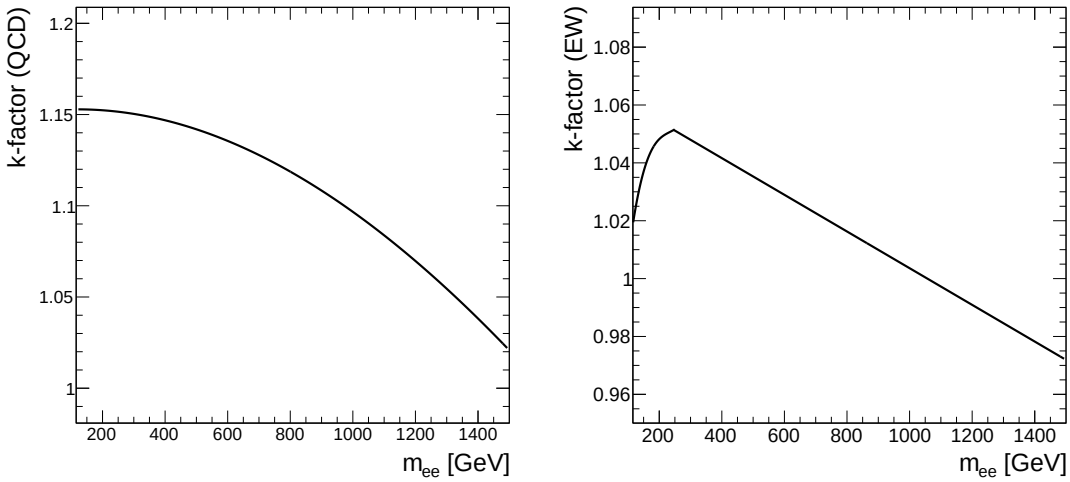

Figure 5.3: QCD (left) and EW (right) k-factors for PYTHIA Monte Carlo samples.

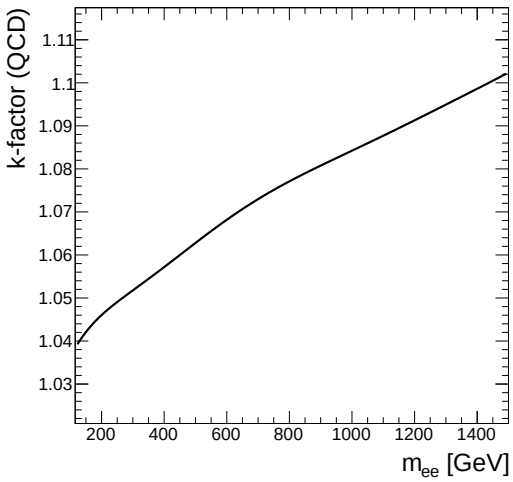

Figure 5.4: QCD k-factor for MC@NLO Monte Carlo samples.

5.3.3 *Energy Smearing*

The electron energy resolution simulated in the Monte Carlo samples is better than the real energy resolution of the detector. Therefore, a Gaussian distributed smearing for each electron object was applied. The width of the Gaussian was estimated using

$Z \to ee$ and $J/\Psi \to ee$ processes. A very tight selection was applied to data and Monte Carlo simulation and the reconstructed widths of the peaks were compared. This determination was done by the electron performance group of ATLAS [79]. The corrections are on the order of one percent and are applied to the Monte Carlo samples with help of a tool, provided by ATLAS. This is done before the p_T of the electrons is calculated or any cut on the objects is applied.

5.3.4 Z/γ^* p_T *Reweighting*

For 2011, the distribution of the transverse momenta of Z-bosons and virtual photons, generated with the PYTHIA generator, shows a large discrepancy when compared to data[5]. Therefore, a reweighting to the Pythia Monte Carlo sample of 2010 was performed to get a better description. The Z/γ^* p_T reweighting was done as a function of invariant mass of the dielectron system (M_{ee}). For all other samples, e.g. the sample from the MC@NLO generator or the samples for 2012, no attempt of a reweighting was made in order to better match the data, as the difference between the other Monte Carlo samples and data is similar to the difference observed for the reweighted PYTHIA Monte Carlo sample. Figure 5.5 shows the comparison between data and the PYTHIA simulation before and after the reweighting.

5.3.5 *Scale Factors for Reconstruction, Identification, and Trigger*

The probability to select a real electron is the product of the reconstruction, identification, and trigger efficiencies, which are slightly different for data and Monte Carlo simulation. To correct these small differences, scale factors $SF = \epsilon_{data}/\epsilon_{MC}$ are applied to the Monte Carlo simulation. The efficiency in data ϵ_{data} is measured in a sample of Z candidates with a so-called "tag and probe" method. An electron candidate with very strict identification is selected and called tag. Afterwards, all other electron candidates in the event are tested as a so-called probe. Together with the tag electron they are required to build a pair with invariant mass in a window around the Z-peak. This provides a clean sample of probe electrons, since the Z-peak region is dominated by real electrons. With this probe objects, the efficiency is studied. The efficiency in simulation is measured by using a Monte Carlo sample, simulating the process $pp \to Z/\gamma^* + X \to e^+e^- + X$ and applying the same tag and probe method. All scale factors were derived and are provided by the ATLAS electron performance group [78]. The scale factors are provided in bins of electron p_T and cluster-η. They typically differ from one by the order of one percent and are applied as weights on a single object basis.

5 This is caused by a bad tuning during the event generation.

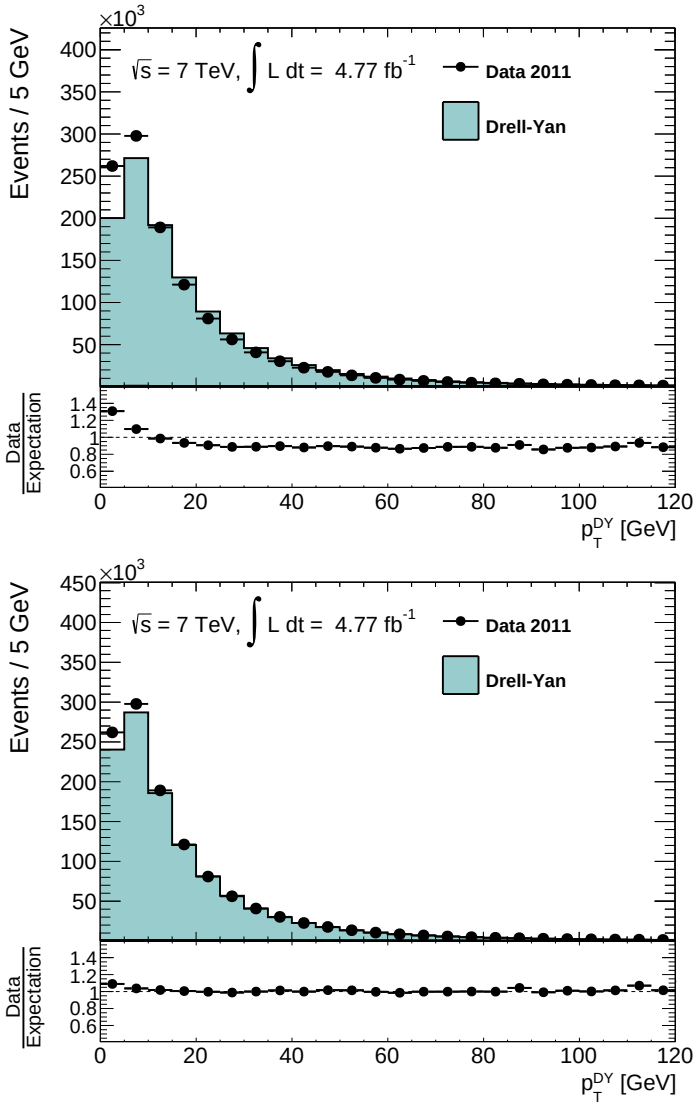

Figure 5.5: Comparison between data and PYTHIA 2011 Monte Carlo sample before (top) and after reweighting (bottom) of the transverse momentum of the Z/γ^* is shown.

PDF-XChange Editor
Click to BUY NOW!
tracker-software.com

PDF-XChange Editor
Click to BUY NOW!
tracker-software.com

Part III

HIGH MASS DRELL-YAN CROSS-SECTION MEASUREMENT

PDF-XChange Editor
Click to BUY NOW!
tracker-software.com

6

INTRODUCTION

In this part the differential measurement of the Drell-Yan cross-section in an invariant mass region between 116 GeV and 1500 GeV at a center-of-mass energy of $\sqrt{s} = 7$ TeV is presented. The measurement is performed in bins of the invariant mass of the di-electron system (m_{ee}) with the following binning in GeV:

- 116, 130, 150, 170, 190, 210, 230, 250, 300, 400, 500, 700, 1000, 15000

This binning was chosen, motivated by the energy resolution of the electrons and migration effects as discussed later.

The Drell-Yan production of e^+e^- pairs leads to a very clean experimental signature with low background contributions and small experimental uncertainties. Due to this and the fact, that the process is described by perturbative quantum chromodynamics (pQCD) at next-to-next-to-leading oder (NNLO) it can be used to perform a precision test of the theory. The process is also a source of background for other Standard Model processes and new physics phenomena may modify the invariant mass spectrum. Furthermore, the invariant mass spectrum is also sensitive to parton distribution functions (PFDs), in particular to the poorly known distribution of antiquarks at large Bjoerken x, where x can be interpreted at leading order as the momentum fraction of the proton carried by the interacting parton.

The result of this analysis was published in Ref. [42] in the summer of 2013. In this part the analysis is described in detail. With respect to the published measurement a number of changes were applied with the goal to optimize the result and to reduce the experimental uncertainties. The largest change is the use of a new set of cuts to identify the electrons as described in Section 4.2. These new cuts are much more efficient to suppress background from misidentified electrons with only small loss of signal efficiency with respect to the old measurement. In addition a more precise energy calibration was used which also provides uncertainties separated in statistical and systematic components. Also the fake background estimation, which were not done by myself for the publication were redone and optimized for this thesis. Furthermore, the instantaneous luminosity, provided by ATLAS, was recalculated last year and is now reduced by 1.7% with respect to the previous result.

PDF-XChange Editor
Click to BUY NOW!
tracker-software.com

7

SELECTION OF DI-ELECTRON EVENTS

In this chapter the dataset used and the triggers for the high-mass Drell-Yan cross-section measurement are presented and the cuts to select the di-electron signal will be discussed. All cuts are identical for data, signal and background Monte Carlo.

7.1 DATASET

For this analysis the complete dataset of proton-proton collisions collected with the ATLAS detector in 2011 at a center of mass energy of $\sqrt{s} = 7$ TeV was used. In Figure 7.1 the cumulative luminosity delivered to and recorded by ATLAS is shown as a function of time.

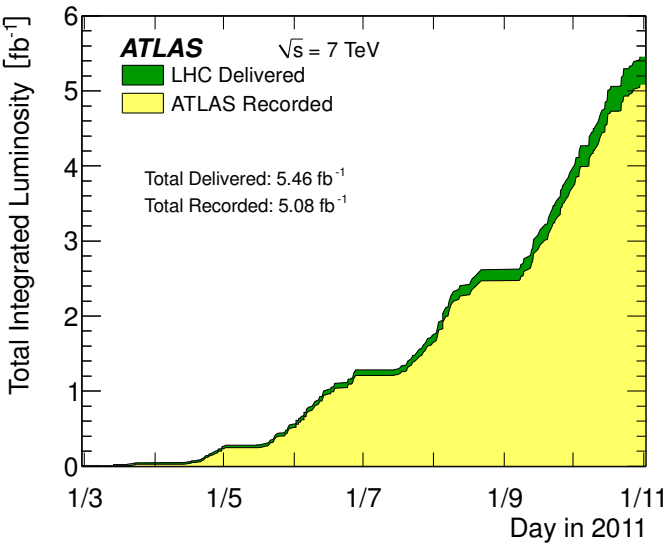

Figure 7.1: Cumulative luminosity versus time delivered to (green), and recorded by ATLAS (yellow) during stable beams and for pp collisions at $\sqrt{s} = 7$ TeV in 2011.

After applying all quality cuts the amount of data corresponds to an integrated luminosity of 4.77 fb^{-1}. For the event selection all data collected in the so-called "EGamma"[1] stream were used. In this stream all events which had fired at least one electron or photon trigger are collected. For the data-driven background estimation, presented in the next chapter, the so-called "JetTauEtMiss" collection was used additionally. As indicated by the name of the stream it contains all events were a jet, tau or missing transverse energy trigger had fired.

1 The "E" denotes electron and the "Gamma" denotes the photon.

7.2 SIGNAL MONTE CARLO SAMPLES

The signal Monte Carlo sample was generated with PYTHIA. To have good statistics over the whole mass range different samples with different mass restrictions were generated. In Table 7.1 the different Monte Carlo samples with their mass restrictions are shown.

Table 7.1: Table of the DY $\rightarrow$ ee Monte Carlo samples generated with PHYTHIA in different regions of invariant mass. Beside the ATLAS internal run number in column two, the cross-sections times branching ratios (column three), the filter efficiency (column four), the number of generated events N_{event} (column five), the corresponding luminosity $\mathcal{L}_{MC}$ is given in column six.

Signature	m_{ee} [GeV]	MC runnumber	$\sigma \times$ BR [pb] PYTHIA	ϵ_F [%]	N_{event} [k]	$\mathcal{L}_{MC}$ [fb^{-1}]
$Z \rightarrow ee$	60-	106046	8.34×10^{2}	100	9991	10.7
DY $\rightarrow$ ee	120-250	105467	8.52	100	299	35.1
DY $\rightarrow$ ee	250-400	105468	4.10×10^{-1}	100	100	243.9
DY $\rightarrow$ ee	400-600	105469	6.64×10^{-2}	100	100	1506.1
DY $\rightarrow$ ee	600-800	105470	1.10×10^{-2}	100	100	9124.9
DY $\rightarrow$ ee	800-1000	105471	2.65×10^{-3}	100	100	37781.1
DY $\rightarrow$ ee	1000-1250	105472	8.92×10^{-4}	100	100	112319.4
DY $\rightarrow$ ee	1250-1500	105473	2.40×10^{-4}	100	100	418012.7
DY $\rightarrow$ ee	1500-1750	105474	7.34×10^{-5}	100	100	1361647.1
DY $\rightarrow$ ee	1750-2000	105475	2.46×10^{-5}	100	100	4057785.2

Each sample was normalized to the luminosity of the data and was corrected to NNLO with help of the k-factors as introduced in Section 5.3.2. The samples are generated in such a way that they can easily stiched together. Only for the inclusive $Z \rightarrow ee$ sample which has no upper mass range a cut on truth level was applied. All events with a Z-boson above a mass of 120 GeV were cutted away. For cross checks of the unfolding method and for comparison to the final result also samples generated with MC@NLO and SHERPA were used. These samples can be found in Table A.2 and Table A.3 in Appendix A.

7.3 TRIGGERS

For the high-mass Drell-Yan cross-section measurement the so called "EF_2g20_loose" trigger was used for the signal selection. This is a diphoton (2g) trigger, with a threshold on transverse energy deposition in the electromagnetic calorimeter of 20 GeV and loose photon ID requirement. That means that all events, accepted by this trigger, contains at least two photon objects with a p_T larger 20 GeV. The loose photon ID is the same as the loose electron ID (see Section 4.2), but without the track requirements. The requirements of the loose photon ID are also part of the loose electron ID. Therefore, this trigger is a good choice for the signal selection and for parts of the data-driven

background method. This trigger is unprescaled[2] for the complete 2011 dataset. For the other part of the background method, where the "JetTauEtmiss" stream was used, a set of single jet triggers was used. The triggers are named "EF_jX_a4tc_EFFS" were X[3] is giving the minimum transverse momentum of a jet in GeV. The jets are reconstructed with a anti-kt [92] algorithm (a), a radius parameter of 0.4 (4) and topological cluster information (tc). For the jet reconstruction on EF level the complete detector information was used (EFFS[4]).

7.4 EVENT BASED SELECTION

In a first step the following selection steps were applied on event level.

Good Run List
Only events collected during good beam conditions and with all important detector components on were taken into account. Therefore a "good run list"(GRL) was applied. The GRL contains information about each lumi block[5] and is provided by the ATLAS EGamma performance group. For this analysis a GRL which requires good conditions in the inner detector and the central calorimeters was used.[6]

Vertex Cut
To remove cosmic events and to be sure that all reconstructed events are coming from collisions in the beam pipe a vertex cut was applied. All events in the selection had to have at least one primary vertex with three or more associated tracks. The Primary Vertex is defined as the proton-proton interaction point.

Trigger
In order to select all events with two electrons the EF_2g20_loose trigger was used. See Section 3.2.6 and Section 7.3 for a detailed description of the trigger system and the triggers used. For the further selection this trigger has an efficiency of ~100% [78].

7.5 ELECTRON SELECTION

The following selection steps are applied on object level to have a high probability to select two real electrons.

Author and η Cut
The phase space of this analysis was restricted to the central region of the detector, which is covered by the inner detector. Therefore a cut on the pseudorapidity of the electron objects $|\eta_{elec}| < 2.47$ was applied. In addition, the transition region

2 Unprescaled means that all event which fulfill the requirements of the trigger are recorded. For some triggers the final rate is so high that only a fraction of all possible events are recorded.
3 X = 10, 15, 20, 30, 40, 55, 75, 100, 135, 180, 240, 320, 425
4 **E**vent **F**ilter **F**ull **S**can
5 A lumi block is defined as one minute of data taking.
6 The complete name of the GRL is "data11_7TeV.periodAllYear_DetStatus-v36-pro10_CoolRunQuery-00-04-08_Eg_standard.xml".

between barrel and end-cap ($1.37 < |\eta_{elec}| < 1.52$) was excluded[7]. With help of the author information only electrons, reconstructed by the standard algorithm[8] were taken into account. For more information about the reconstruction algorithm see Section 4.1.

p_T Cut
To be sure to be at a region where the trigger has an efficiency of 100% a cut on the transverse momentum of the objects $p_T > 25$ GeV was applied.

Object Quality
During the run period some of the optical transceivers (OTx) on the front end board of the Liquid Argon (LAr) calorimeter were broken. Electron objects which are detected close by such a channel were removed from the selection. Also events with LAr noise bursts were removed.

Electron Identification
The "medium" electron identification criteria were used as described in Section 4.2. This is the largest change with respect to the published measurement [42], where old identification cuts with smaller background suppression were used[9]. With this new set of cuts the background contribution from jets misidentified as electrons is reduced by 70%, where the signal efficiency is reduced by only 15%.

B-layer Hit
The innermost layer of the pixel detector, called "B-layer", is very efficient to suppress electrons from conversions. The probability that photons are interacting early in the pixel detector is small because they need some time and additional material to convert into electrons. To suppress background from converted photons the B-layer was required to have at least one hit. In some regions of the detector the innermost layer of the pixel detector was not properly working. If the electron was passing through such a region this cut was not applied.

7.6 FINAL SELECTION

For events with more than two objects passing this selection only the two objects with the individual highest p_T were selected. They are referred to as leading and subleading electrons in the following.
In addition the leading electron was required to be isolated, by demanding that the sum of calorimeter cell energies in a cone size $\Delta R = 0.2$ around the cluster barycenter, excluding a 5 x 7 grid of cells in the center of that cone, be less than 7 GeV. This was realized by using the "ETcone20_pt_NPVcorrected" variable. The suffixes denote corrections for p_T dependence and pile-up, by taking the number of primary vertices in the event into account.
There was no requirement on the charge of the two objects applied to avoid the related

7 The resolution in the transition region is very poor.
8 The variable "el_author" had to be 1 or 3.
9 ATLAS internal the new set of identification cuts is called "medium++" and the old one is called "medium".

systematic uncertainty due to charge-misidentification. This uncertainty is difficult to quantify and potentially large due to the limited resolution of the inner detector for objects with large transverse momenta.
The invariant mass of the dielectron system was calculated from the sum of the Lorentz-Vector of both electrons. The number of events after all selection steps in bins of the di-electron mass (m_{ee}) are shown in Table 7.2. A cut flow of the important selection cuts is given in Table A.1 in Appendix A.

Table 7.2: Number of candidate events in data passing the final selection in bins of m_{ee}.

m_{ee} [GeV]	116-130	130-150	150-170	170-190	190-210	210-230
data	8436	6056	3226	1930	1314	801

m_{ee} [GeV]	230-250	250-300	300-400	400-500	500-700	700-1000	1000-1500
data	604	870	629	198	110	29	5

PDF-XChange Editor
Click to BUY NOW!
tracker-software.com

PDF-XChange Editor Click to BUY NOW! tracker-software.com

8

BACKGROUND

In the following the different sources of background contributing to this analysis are presented. There are two different types of backgrounds which will be discussed. Background components from processes with two real[1] electrons in the final state and background sources with one or two "fake"[2] electrons in the final state.

8.1 REAL ELECTRON BACKGROUND

Three processes with two or more real electrons in the final state give a significant contribution to the background and will be discussed in this section. In detail these are the diboson (ZZ, WZ and WW), $t\bar{t}$ and single top production processes. The contribution of these backgrounds is estimated by using Monte Carlo generated samples. All corrections mentioned in Section 5.3 are applied. The samples are normalized to the integrated luminosity, using the best known production cross-section. In Table 8.1 and Table 8.2 the samples with generated and calculated cross-section, filter efficiency ϵ_f, number of generated events N_{event} and corresponding luminosity $\mathcal{L}_{MC}$ are listed. Contributions from $DY \to \tau\tau$ and $W\gamma$ production processes were tested and found to be negligible.

8.1.1 *Diboson Production*

Three production processes contribute to the diboson background. These are $pp \to ZZ + X$, $pp \to ZW + X$ and $pp \to WW + X$. In all cases a cut on the real electron number was applied to have only events with at least two real electrons in the final state. For each process there are three different Monte Carlo samples available. One, without restriction on the range of invariant mass[3] and two binned in invariant mass from 400 GeV to 1000 GeV and from 1000 GeV to 1600 GeV. For the samples without a restriction on the mass, the invariant mass of any combination of two electrons were calculated. Events with an invariant masses above 400 GeV were rejected to avoid overlap. Using these three samples leads to good statistics even at high invariant mass.
In Figure 8.1 the contribution of the different processes is shown.
For visibility the contributions of the single processes are summarized for all further plots to a diboson contribution. The WW distribution shows a smooth behavior over the

1 Real electrons refers to objects which are electrons and are reconstructed as electrons.
2 Fake electrons means that the object is reconstructed and identified as an electron, but is in reality not an electron.
3 Invariant mass refers to the invariant mass of the two electron system. In events with more than two electrons any combination had to be with in the mass range.

Table 8.1: Table of the simulated Monte Carlo diboson ($pp \to WW + X$, $pp \to WZ + X$, $pp \to ZZ + X$) samples. All samples are simulated with the HERWIG 6.520 generator. In the second column the corresponding ATLAS internal run number is given. In column three the cross-section times branching ratio times filter efficiency reported by the generator is given. Column four shows the corresponding theoretical calculated cross-section at next-to-leading (NLO) order [93]. In the last three columns the filter efficiency ϵ_f, the number of generated events N_{event} and the corresponding luminosity $\mathcal{L}_{MC}$ are listed.

Signature (filter)	MC runnumber	$\sigma B \times \epsilon_f$ [pb] HERWIG	NLO	ϵ_f [%]	N_{event} [k]	$\mathcal{L}_{MC}$ [fb^{-1}]
WW (1 lepton filter)	105985	12.12	17.49	38.95	2489	142.3
WZ (1 lepton filter)	105987	3.57	5.74	31.04	1000	174.1
ZZ (1 lepton filter)	105986	0.98	1.27	21.32	250	196.7
WW ($m_{ee} = 0.4 - 1$ TeV)	145487	2.13×10^{-3}	3.13×10^{-3}	0.589	20	6388
WW ($m_{ee} = 1 - 1.6$ TeV)	145488	2.2×10^{-5}	3.2×10^{-5}	0.006	20	625000
WZ ($m_{ee} = 0.4 - 1$ TeV)	145493	1.11×10^{-3}	1.56×10^{-3}	0.251	20	12836
WZ ($m_{ee} = 1 - 1.6$ TeV)	145494	3.2×10^{-5}	4.5×10^{-5}	0.007	20	444444
ZZ ($m_{ee} = 0.4 - 1$ TeV)	145499	3.83×10^{-4}	4.48×10^{-4}	0.114	20	44643
ZZ ($m_{ee} = 1 - 1.6$ TeV)	145500	6.9×10^{-6}	8.1×10^{-6}	0.002	20	2469136

Table 8.2: Table of the simulated Monte Carlo top production ($pp \to t\bar{t} \to \ell X$, $pp \to Wt \to X$) samples. All samples are simulated with the MC@NLO 4.01 generator. In the second column the corresponding ATLAS internal run number is given. In column three the cross-section times branching ratio times filter efficiency reported by the generator is given. Column four shows the corresponding theoretical calculated cross-section at next-to-next-to-leading (NNLO) order [94, 95]. In the last three columns the filter efficiency ϵ_f,the number of generated events N_{event} and the corresponding luminosity $\mathcal{L}_{MC}$ are listed.

Signature	MC runnumber	$\sigma \times$ BR [pb] MC@NLO 4.01	NNLO	ϵ_F [%]	N_{event} [k]	$\mathcal{L}_{MC}$ [fb^{-1}]
$t\bar{t} \to \ell X$	105200	1.45×10^2	1.65×10^2	54.26	11585	70.2
$Wt \to X$	108346	1.43×10^1	1.57×10^1	100	788	50.2

whole mass range, which decreases at higher invariant masses. The smooth distribution is expected because it is the combination of the electrons coming from the two W-decays.

The distribution of the WZ and ZZ contribution shows a different behavior. There is a clear peak at ≈ 91 GeV visible, followed by a falling spectrum. In the selection the two electrons with the individual highest p_T of an event are selected. In these two samples there can be three or more real electrons. If the two electrons from the Z-boson decay are selected they contribute to the peak, if not the combination of two electrons will lead to the smooth decreasing spectrum.

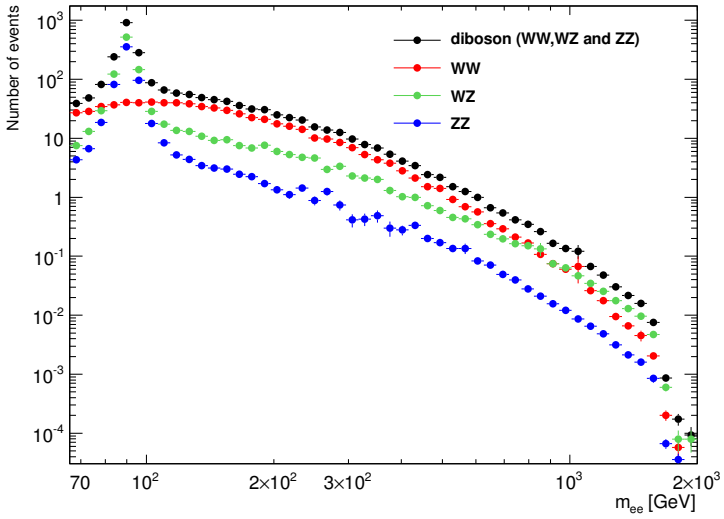

Figure 8.1: The three diboson background contributions WW (red), WZ (green), ZZ (blue) and the combination (black) are shown. The number of expected events for $L = 4.77\,fb^{-1}$ is plotted against the invariant mass of the di-electron system in an equidistant logarithmic binning.

The turn on at low invariant mass at all three spectra is due to the kinematic cuts (η and p_T) applied on the electrons. The statistics in the complete range of this measurement is good, therefore no further extrapolation is needed.

8.1.2 $t\bar{t}$ *Production*

At a center-of-mass energy of 7 TeV the cross-section for $t\bar{t}$ production is of the order of 1 nb. The top quark decays with $\approx$ 100% into a b-quark and a W-boson and the probability that both W-bosons decay into electrons is $\approx$ 1.2 %. Therefore the $t\bar{t}$ production is another important background source. Here, only events with two real electrons in the final state were taken into account to avoid an overlap with the fake background estimation. The spectrum of the $t\bar{t}$ contribution after all selection cuts is shown in Figure 8.2 on the left side. The distribution shows the same behavior as the spectrum of the WW process. In the region between 700 GeV and 1500 GeV the statistics gets worse, but this effect is covered by the binning of the measurement.

8.1.3 *Single Top Production*

The single top production was discovered at the Tevatron in 2009 [96]. The production in association with a W-boson (so called tW channel) is a non-negligible background source which can lead to two electrons in the final state. The other channels have at most one electron in the final state or the cross section is negligible small and are therefore not considered. The distribution extracted from the Monte Carlo sample is shown in Figure 8.2 on the right side. The shape is nearly the same as for the background resulting from the $t\bar{t}$ production, but due to the smaller production cross-section it is smaller by an order of magnitude.

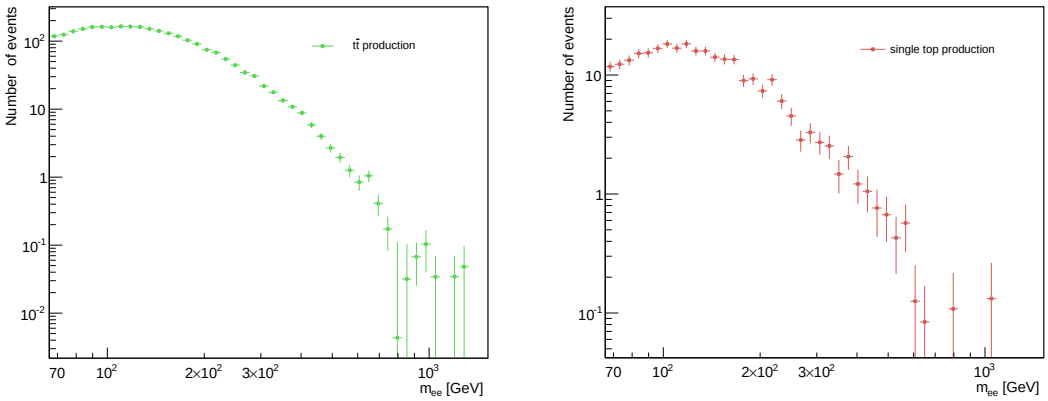

Figure 8.2: The $t\bar{t}$ contribution (left) and the single top contribution (right) after the final selection are shown. The number of expected events for $L = 4.77\,fb^{-1}$ is plotted against the invariant mass of the di-electron system in an equidistant logarithmic binning.

8.2 FAKE ELECTRON BACKGROUND

There is the possibility that an non electron object fakes an electron signature in the detector. In most of the cases these misidentified particles are jets, which consist mostly out of pions and kaons. Neutral pions, π^0, for example decaying into two photons will give an electron-like signature in the e.m. calorimeter. Photon can lead to tracks in the inner detector only after conversion , but there is the probability of an additional charged hadron in the jet, e.g. a charged pion, which gives a track pointing into the direction of the energy deposition of the photons.
The background with one or two fakes in the final state was estimated using a data driven method called matrix method. This method includes the di-jet background, the background from the leptonic decay of a W-Boson in association with a jet and all other processes with one real electron in the final state[4].

8.2.1 *Matrix Method*

The idea of the Matrix method is to loosen (or invert) certain criteria in the signal selection and estimate the rate with which these loose objects are reconstructed as signal-like objects. Afterwards these fake rates are applied to the selection.
There are four different possible configurations available after the selection. That both selected objects are real electrons (N_{RR}), that the selected object with the higher p_T is a real electron and the other object is not (N_{RF}), the other way around that the object with higher p_T is a "fake" and the sub-leading one is a real electron (N_{FR}) or that both selected objects are "fakes" (N_{FF}). The real configuration is not known and it is not possible to measure these quantities. Therefore new configurations are introduced, N_{TT}, N_{TL}, N_{LT} and N_{LL}. In this notation T stands for an object which is selected with an electron-like tight selection[5] and L means an object selected with a looser, more "fake"-

4 For example semi-leptonic $t\bar{t}$ events or single top production with an associated W-boson where one of the W-boson decays hadronic.

5 This selection is identical to the signal selection as described in Section 7.

like selection, but failing the tight selection. For the measurable quantities and the real configuration the first index is always related to the leading and the second index to the sub-leading electron.
The configuration with the measurable quantities is related via

$$\begin{pmatrix} N_{TT} \\ N_{TL} \\ N_{LT} \\ N_{LL} \end{pmatrix} = \begin{pmatrix} r_1 r_2 & r_1 f_2 & f_1 r_2 & f_1 f_2 \\ r_1(1-r_2) & r_1(1-f_2) & f_1(1-r_2) & f_1(1-f_2) \\ (1-r_1)r_2 & (1-r_1)f_2 & (1-f_1)r_2 & (1-f_1)f_2 \\ (1-r_1)(1-r_2) & (1-r_1)(1-f_2) & (1-f_1)(1-r_2) & (1-f_1)(1-f_2) \end{pmatrix} \begin{pmatrix} N_{RR} \\ N_{RF} \\ N_{FR} \\ N_{FF} \end{pmatrix} \tag{8.1}$$

to the real configuration. The coefficient $f_{1,2}$ (called fake rate) gives the probability that a fake object (F) is reconstructed as an electron-like object (T), while $(1-f_{1,2})$ gives the probability that the fake object only fulfill the looser selection (L). The other two possibilities that a real electron (R) is reconstructed as an electron-like object and that a real electron is reconstructed as a fake-like object, passing the looser selection but fails the tight selection is represented by $r_{1,2}$ (called real electron efficiency) and $(1-r_{1,2})$. The index 1 refers to the leading[6] electron and 2 to the sub-leading electron. Due to the fact that the selection between the leading and the sub-leading electron differs in the isolation cut, it is important to keep N_{TL}, N_{LT}, $f_{1,2}$ and $r_{1,2}$ separated.
This matrix can be inverted to replace the inaccessible truth quantities N_{RR}, N_{RF}, N_{FR} and N_{FF} with the measurable quantities N_{TT}, N_{TL}, N_{LT} and N_{LL}. The inversion of Equation 8.1 gives:

$$\begin{pmatrix} N_{RR} \\ N_{RF} \\ N_{FR} \\ N_{FF} \end{pmatrix} = \frac{1}{(r_1-f_1)(r_2-f_2)} \begin{pmatrix} (f_1-1)(f_2-1) & (f_1-1)f_2 & f_1(f_2-1) & f_1 f_2 \\ (f_1-1)(1-r_2) & (1-f_1)r_2 & f_1(1-r_2) & -f_1 r_2 \\ (r_1-1)(1-f_2) & (1-r_1)f_2 & r_1(1-f_2) & -f_2 r_1 \\ (1-r_1)(1-r_2) & (r_1-1)r_2 & r_1(r_2-1) & r_1 r_2 \end{pmatrix} \begin{pmatrix} N_{TT} \\ N_{TL} \\ N_{LT} \\ N_{LL} \end{pmatrix} \tag{8.2}$$

With help of Equation 8.1 it is possible to estimate the number of events which pass the signal selection but contain at least one fake object. This is given by N_{TT} without the term where two real electrons are selected.

$$N_{TT}^{Fake} = r_1 f_2 N_{RF} + f_1 r_2 N_{FR} + f_1 f_2 N_{FF} \tag{8.3}$$

Equation 8.2 is used to get rid of the inaccessible truth quantities N_{FF}, N_{FR} and N_{RF}. With the definition of $\alpha = \frac{1}{(r_1-f_1)(r_2-f_2)}$ Equation 8.3 can be expressed by

$$\begin{aligned} N_{TT}^{Fake} = {} & \alpha r_1 f_2[(f_1-1)(1-r_2)N_{TT} + (1-f_1)r_2 N_{TL} + f_1(1-r_2)N_{LT} - f_1 r_2 N_{LL}] \\ & + \alpha f_1 r_2[(r_1-1)(1-f_2)N_{TT} + (1-r_1)f_2 N_{TL} + r_1(1-f_2)N_{LT} - r_1 f_2 N_{LL}] \\ & + \alpha f_1 f_2[(1-r_1)(1-r_2)N_{TT} + (r_1-1)r_2 N_{TL} + r_1(r_2-1)N_{LT} + r_1 r_2 N_{LL}]. \end{aligned} \tag{8.4}$$

To get a feeling about the impact of the different measurable quantities and also to be able to apply all corrections corresponding to a measurable quantity in the analysis in one step the formula was transposed to:

6 The one with the higher p_T.

$$\begin{aligned} N_{TT}^{Fake} = \alpha[&r_1 f_2 (f_1 - 1)(1 - r_2) + f_1 r_2 (r_1 - 1)(1 - f_2) + f_1 f_2 (1 - r_1)(1 - r_2)]N_{TT} \\ &+\alpha f_2 r_2 [r_1 (1 - f_1) + f_1 (1 - r_1) + f_1 (r_1 - 1)]N_{TL} \\ &+\alpha f_1 r_1 [f_2 (1 - r_2) + r_2 (1 - f_2) + f_2 (r_2 - 1)]N_{LT} \\ &-\alpha f_1 f_2 r_1 r_2 N_{LL} \end{aligned} \tag{8.5}$$

In the following the background component N_{TT}^{Fake} estimated with this method is labeled with "Dijet & W+jets". This label was chosen, because the main contributions of the fake background are coming from events with two jets faking an electron or events where one real electron from a W-boson decay is selected together with a fake electron from an additional jet. Nevertheless it is important to keep in mind, that with this method all processes with only one or without real electrons are covered.
In this analysis the fake rate f_i is defined as

$$f_i = \frac{\left(N_{tight}^{fake}\right)_i}{\left(N_{loose}^{fake}\right)_i}. \tag{8.6}$$

8.2.1.1 *Variation of the Matrix Method*

In Equation 8.5 are a lot of coefficients. To simplify the equation and to get a feeling about the stability of the method the real electron efficiency $r_{1,2}$ can be set to one. This assumes that every real electron will be selected with the signal selection. This is not true, but the effect on the background estimation is small and the neglected inefficiency can be easily corrected with the help of Monte Carlo samples. For the final estimation of the fake background component the full matrix method using Equation 8.5 was used. The variation with $r_{1,2} = 1$ was only used to estimate the uncertainty on the background method. With $r_{1,2} = 1$ Equation 8.1 becomes

$$\begin{pmatrix} N_{TT} \\ N_{TL} \\ N_{LT} \\ N_{LL} \end{pmatrix} = \begin{pmatrix} 1 & f_2 & f_1 & f_1 f_2 \\ 0 & 1 - f_2 & 0 & f_1 (1 - f_2) \\ 0 & 0 & 1 - f_1 & (1 - f_1) f_2 \\ 0 & 0 & 0 & (1 - f_1)(1 - f_2) \end{pmatrix} \begin{pmatrix} N_{RR} \\ N_{RF} \\ N_{FR} \\ N_{FF} \end{pmatrix} \tag{8.7}$$

and the inverted matrix is given by

$$\begin{pmatrix} N_{RR} \\ N_{RF} \\ N_{FR} \\ N_{FF} \end{pmatrix} = \begin{pmatrix} 1 & \frac{f_2}{f_2 - 1} & \frac{f_1}{f_1 - 1} & \frac{f_1 f_2}{(f_1 - 1)(f_2 - 1)} \\ 0 & \frac{1}{1 - f_2} & 0 & -\frac{f_1}{(f_1 - 1)(f_2 - 1)} \\ 0 & 0 & \frac{1}{1 - f_1} & \frac{f_2}{(f_1 - 1)(f_2 - 1)} \\ 0 & 0 & 0 & \frac{1}{(f_1 - 1)(f_2 - 1)} \end{pmatrix} \begin{pmatrix} N_{TT} \\ N_{TL} \\ N_{LT} \\ N_{LL} \end{pmatrix}. \tag{8.8}$$

This matrix can further be simplified by the definition of the fake factor $F_i = \frac{f_i}{1 - f_i}$. With help of Equation 8.6 F_i can be written as

$$F_i = \frac{N_{tight}^{fake} / N_{loose}^{fake}}{1 - N_{tight}^{fake} / N_{loose}^{fake}} = \frac{N_{tight}^{fake}}{N_{loose}^{fake} - N_{tight}^{fake}}. \tag{8.9}$$

With this definition the three fake background configurations[7] are given by

$$f_2 N_{RF} = F_2 N_{TL} - F_1 F_2 N_{LL}, \tag{8.10}$$
$$f_1 N_{FR} = F_1 N_{TL} - F_1 F_2 N_{LL}, \tag{8.11}$$
$$f_1 f_2 N_{FF} = F_1 F_2 N_{LL} N_{LL}. \tag{8.12}$$

Equation 8.10 and Equation 8.11 are the contributions from background events with one real electron and one fake, N_{W+jet}, and Equation 8.12 corresponds to the background with two fake signatures, N_{Dijet}. After adding these components up the final formula to calculate the fake background is then given as

$$N_{Dijet\,\&\,W+jets} = F_2 N_{TL} + F_1 N_{LT} - F_1 F_2 N_{LL}. \tag{8.13}$$

To correct for the neglected inefficiency the simplified method was not only applied to the data, but also on all Monte Carlo samples with real electrons processes. Afterwards the result from the Monte Carlo samples was subtracted from the background estimation from data.

8.2.2 *Fake Rate Estimation*

To calculate the fake rates and the corresponding fake factors a sample which is dominated by fake objects is needed. Most of the time the fake objects are miss-identified jets. Two possible methods to get a jet enriched sample and three different methods to estimate the fake rates were used for this analysis. For the first method to get an enriched sample the same dataset and trigger as described in the event selection was used while for the second method the so-called "JetTauEtMiss" stream and a bunch of single jet triggers were used. See Section 7.1 and Section 7.3 for a more detailed description of the stream and the triggers used. The three different methods are discussed in the following and afterwards the resulting fake rates are presented.

Tag and Probe Method with Electron Trigger
For this method the same trigger as for the signal selection was used. The fake rates were estimated using a tag and probe method. The idea is to select an object with high probability to be a fake as tag and consider all other as an electron reconstructed objects as probes. Aim of this method is to get a clean sample of jets and to estimate the rate with which they are selected as electrons. To get a jet enriched sample the real electron contribution from W-boson decays were removed with a cut on the missing transverse energy. Only events with $E_T^{miss} < 25$ GeV were kept. To suppress electrons from the Z-boson decay events where the invariant mass of the tag and the probe object is within 20 GeV of the Z-boson mass were rejected. Furthermore only probes, which had the same charge as the tag objects were taken into account. These cuts have a high efficiency to remove non fake-like probe objects. To remove remaining contributions from miss-identified real electrons the fake rate and

7 With the assumption of the real electron efficiency to be equal one the component with two real electrons does not contribute any more.

fake factors were corrected with the help of Monte Carlo simulations. Therefore the tag and probe method was also applied to the signal and real electron background Monte Carlo simulations[8] and the resulting contributions were subtracted from the distributions obtained from the data sample.
To be selected as tag the object had to be in the central region of the detector, the transverse momentum of it had to be larger than 20 GeV and passed at least the loose identification without requiring the "loose" matching between track and the energy deposition in the calorimeter[9]. In addition it had to fail the matching between track and energy deposition in the calorimeter, which is a requirement of the medium identification. All other electron candidates in the event were then tested as probe objects. This was done for two different selections:

- N^{fake}_{loose}: For this selection the probe had to fulfill only the trigger requirements. Therefore the object had to be a p_T larger then 25 GeV and had to be identified with the loose ID selection as described in Section 4.2 without the requirement of the matching between track and cluster position.
- N^{fake}_{tight}: This selection was done using the same cuts as for the event selection as described in Section 7.4, with and without the isolation required for leading and sub-leading electron, respectively. Further on, this is quoted as "leading tight" (with isolation) and "sub-leading tight" (without isolation) and used to calculate the fake rates and fake factors for the leading and sub-leading object.

The different probe selections were binned in p_T and η. The selected events for the loose, leading tight and sub-leading tight probes are presented in Figure 8.3 binned in p_T. The probe objects extracted from data are shown together with a stack of all Monte Carlo samples which were used for the correction and were subtracted afterwards. As expected all distributions shows a falling spectrum for higher transverse momentum. The Monte Carlo contribution is on the order of 20% for the loose selection and a around 25% for the tight selections. The differences between "sub-leading tight" and "leading tight" is visible but since the selection differs only in the isolation cut it is only a small effect.

Single Object Method with Jet Trigger
To estimate the fake rates with a second method, data collected with the JetTauEtMiss stream was used. All events which fulfill the requirements of a single jet trigger were taken into account. At the Large Hadron Collider (LHC) the jet production rate is very high. Therefore, it is not possible to save all events which contains jets. Therefore, different triggers with different requirements on the transverse momentum (p_T) of the reconstructed objects are available. For this analysis thirteen different jet triggers[10] were used.
The jet objects in these selected events are reconstructed with the anti-k_T algorithm [97] and a size parameter of $R = 0.4$. A "medium" jet cleaning was applied to each object. This jet cleaning includes cuts against background from cosmic muons, a cut

8 Normalized to the integrated luminosity of the data.
9 These are the minimal trigger requirements.
10 "EF_jX_a4tc_EFFS" (X = 10, 15, 20, 30, 40, 55, 75, 100, 135, 180, 240, 320, 425), where X is the p_T requirement in GeV.

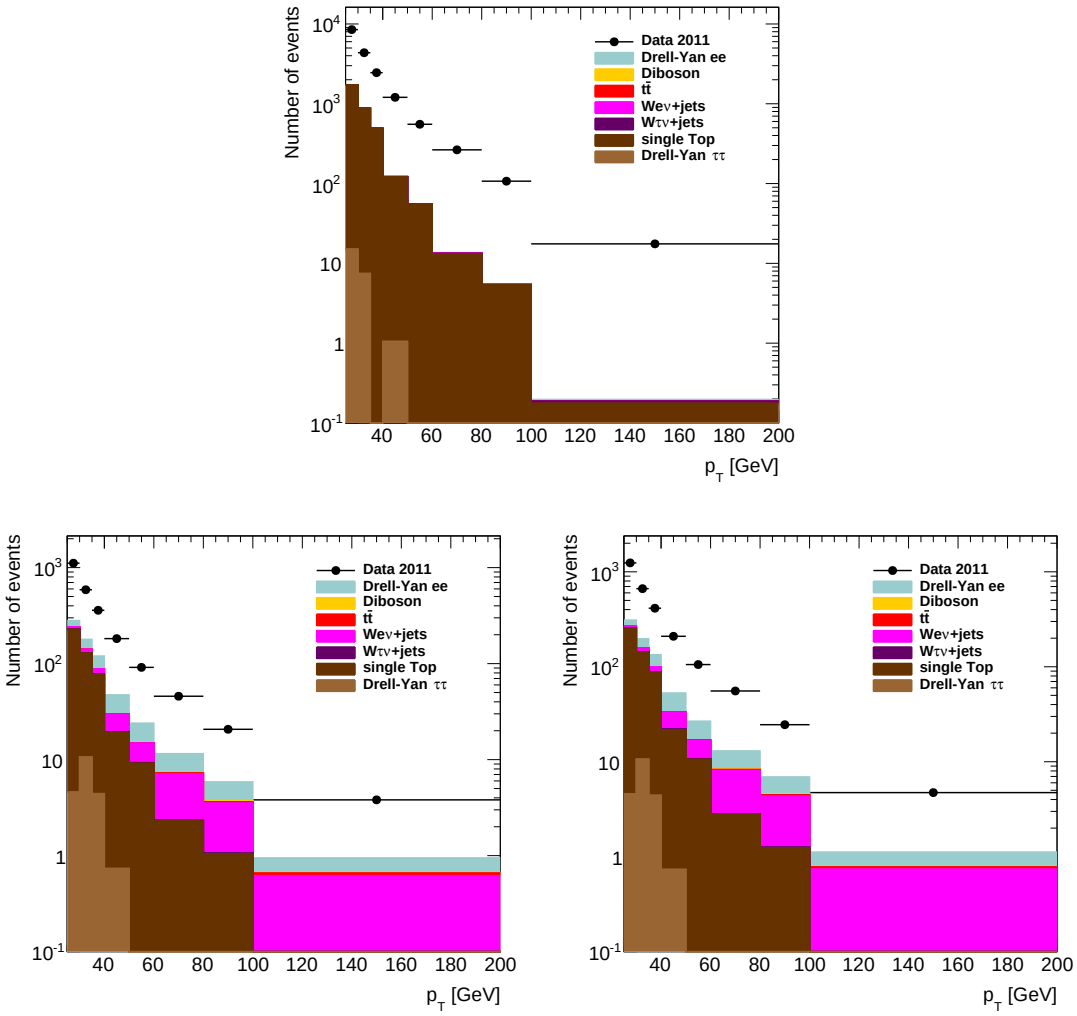

Figure 8.3: The p_T distributions of the "loose" (top), "leading-tight" (bottom left) and "subleading tight" (bottom right) probes estimated from the tag and probe method on the EGamma stream. In addition to the selection from data (black) the Monte Carlo corrections are shown stacked.

on the energy fraction in the electromagnetic calorimeter, and requires good quality of the shower in the hadronic calorimeters. To be sure that each selected object was reconstructed as a jet and also as an electron object, a $\Delta R < 0.1$ matching was applied to each object. These reconstructed electron objects were then used to estimate the fake rate.

In addition to the trigger requirements above, the events had to pass all the event based cuts as described in Section 7.4 to the same quality requirements as the signal selection. Although a jet trigger was used, there is a real electron contribution from Z and W-bosons which is not negligible. To get rid of these real electrons all events with two or more electron objects passing the medium identification criteria were rejected. Also events with two loose identified electrons were rejected when the invariant mass of these two objects was within 20 GeV of the Z-boson mass ($|m_{ee} - 91\,GeV| < 20\,GeV$). To suppress real electrons from $W \to e\nu$ decays the missing energy in the detector due to the neutrino was used and a cut on the missing

transverse energy ($E_T^{miss} < 25\,GeV$) was applied.
In the remaining events the objects of the categories N_{loose}^{fake} and N_{tight}^{fake} as defined above were selected. Again the tight selection were separated for the leading and sub-leading objects, with and without the isolation requirement.
To avoid a bias due to the different efficiencies of the different triggers the fake rate was calculated for each trigger separately and the weighted average was then calculated afterwards using

$$f = \frac{\sum_{i=1}^{i=n_{trig}} f_i/\Delta f_i^2}{\sum_{i=1}^{i=n_{trig}} 1/\Delta f_i^2}, \qquad \Delta f^2 = \frac{1}{\sum_{i=1}^{i=n_{trig}} 1/\Delta f_i^2} \tag{8.14}$$

where f and Δf are the resulting fake rate and uncertainty and f_i and Δf_i are the fake rates and uncertainties for each trigger.

Tag and Probe Method with Jet Trigger
The third method is a combination of the two previous methods. The same dataset and triggers as for the single object method above was used but the fake rate estimation was done with the tag and probe method. The advantage of this method with respect to the other tag and probe method is that no restrictions from the trigger have to be considered. To be selected as tag the object had to be in the central region of the detector, the transverse momentum had to be larger than 15 GeV and it had to fail the loose identification selection. All other electron candidates in the event were then tested as probe objects. To get rid of the real electron contributions probes were rejected where the invariant mass of the tag and the probe object is within 20 GeV to the Z-boson mass. Furthermore only probes, which had the same charge as the tag objects were taken into account. Also the cut on the missing transverse energy was applied to suppress electrons from the W-boson decay. In the remaining events again the objects of the categories N_{loose}^{fake} and N_{tight}^{fake} were selected and the fake rate was calculated for each trigger separately. Afterwards again Equation 8.14 was used to obtain the final fake rates.

8.2.2.1 *Comparison of the Different Methods*

The results of the different methods are shown in Figure 8.4 for the barrel region ($|\eta| < 1.37$) and in Figure 8.5 for the end-cap region ($1.52 < |\eta| < 2.47$).
In the two barrel regions the statistic of all methods is quite good. In general the two methods using the "jet" stream are in agreement. Only in bins with high statistical uncertainties the tag and probe method shows sometimes larger fluctuations. For higher values of p_T the method using the "Egamma" stream provides always higher fake rates than the two other methods. This is especially visible in the region $0.6 < |\eta| < 1.37$ for the leading electrons. Due to the missing isolation cut the fake rates for the sub-leading objects are slightly higher for all η regions.
The statistic for the three end-cap bins is quite low but the fine binning is needed due to the different coverage of the sub-detector systems. The end-cap region up to $|\eta| < 2.01$ is still covered by the TRT and therefore the conditions are nearly the same as for the two barrel regions. The region $|\eta| > 2.01$ is no longer covered by the TRT which leads to different fake rates and the last region of $|\eta| > 2.37$ is additionally not covered by the

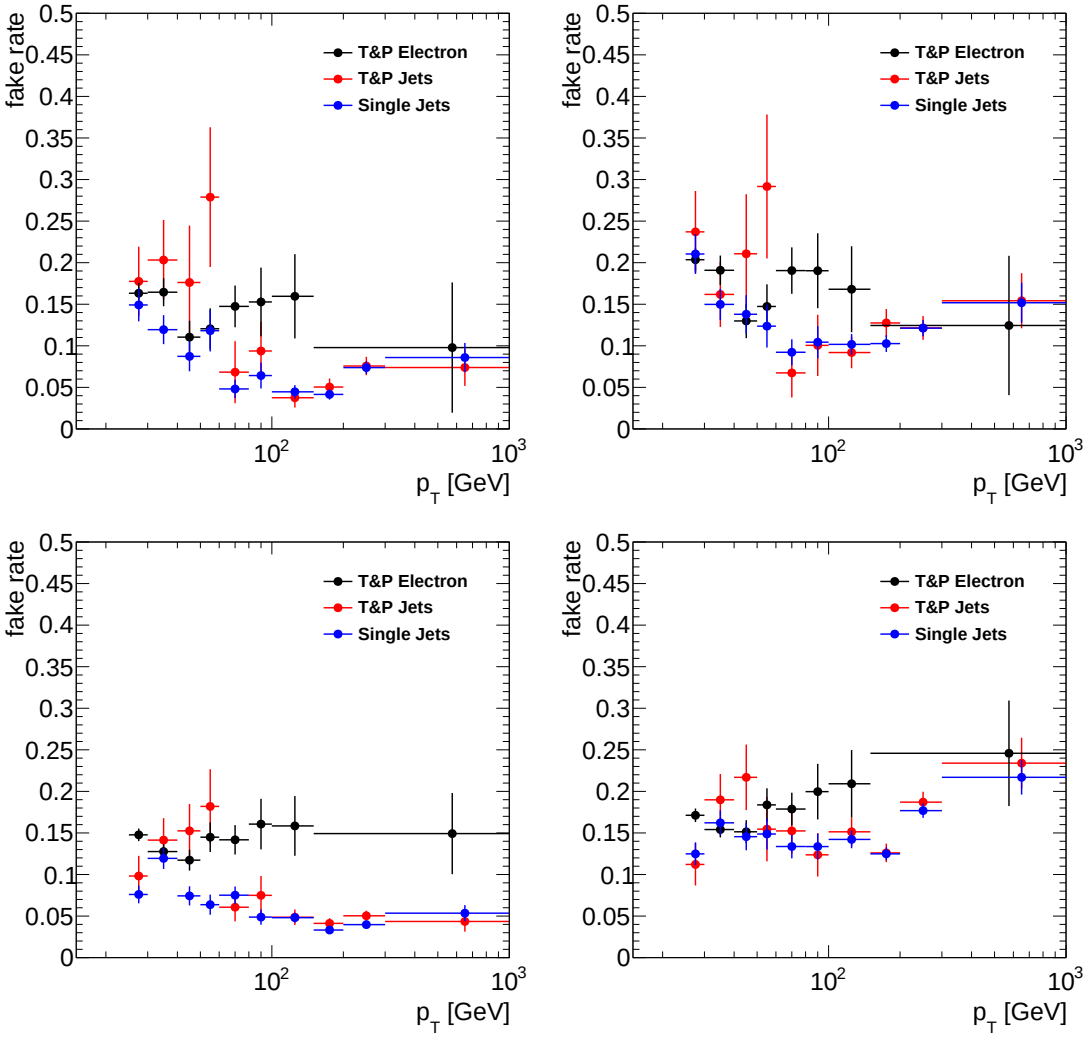

Figure 8.4: The p_T spectra of the fake rates of the leading electron f_1 (left) and of the sub-leading electron f_2 (right) for $|\eta| < 0.6$ (top) and $0.6 < |\eta| < 1.37$ (bottom) are shown. In blue the fake rates estimated with the single object method and in red (jet trigger) and black (electron trigger) the results of the two tag and probe methods are shown.

most inner layer of the pixel detector. Within the statistical uncertainties all methods leads to the same fake rates. For the leading electrons the distribution is nearly flat, where the distributions for the sub-leading electrons seem to predict higher fake rates for larger values of p_T.

As default the fake rates, estimated with the single object method and jet triggers was used. This method gives the cleanest jet sample where no further Monte Carlo corrections are needed and has in addition the highest statistics. The fake rates from the other methods are used to estimate the uncertainty on the background estimation as discussed in the following.

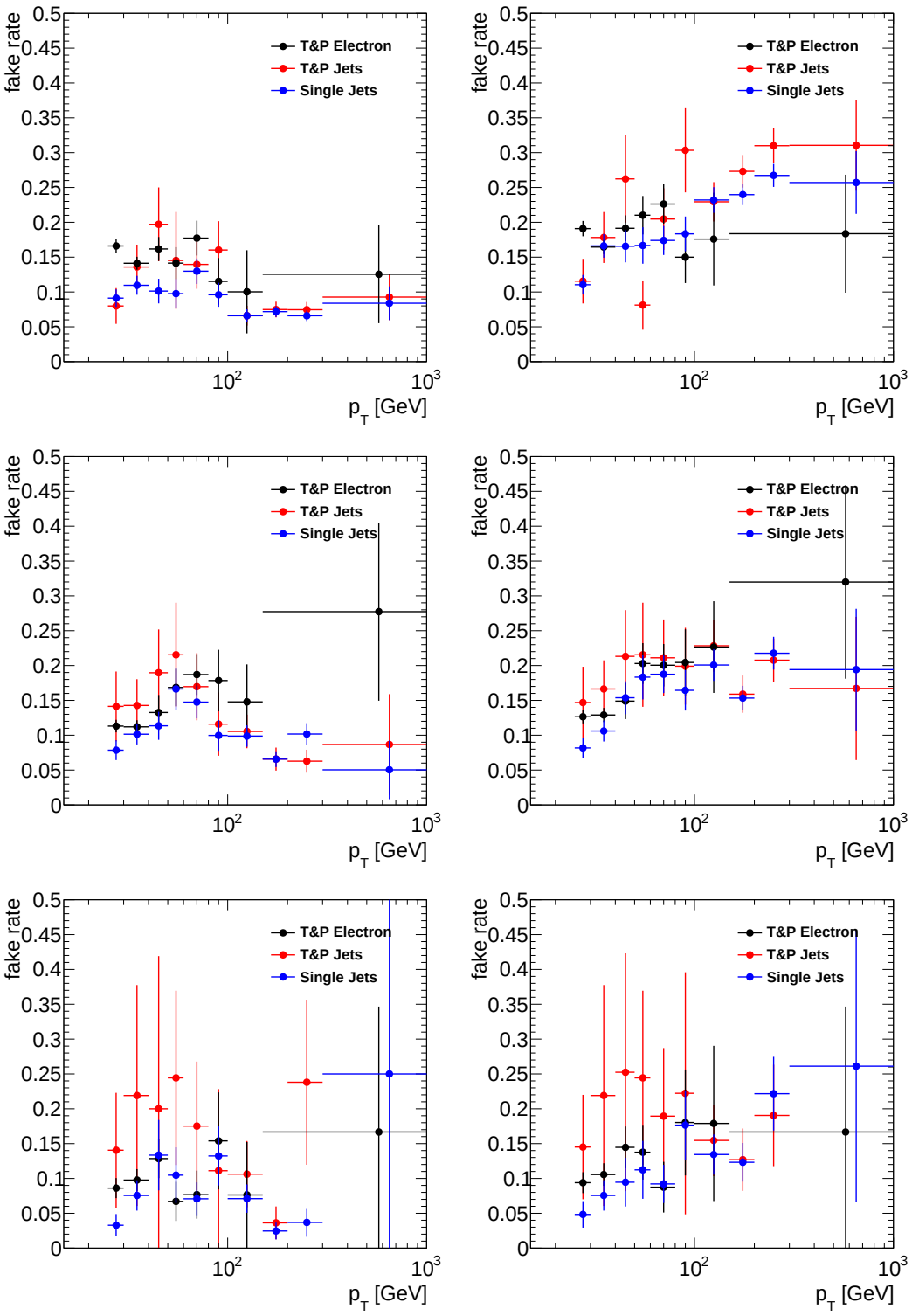

Figure 8.5: The p_T spectra of the fake rates of the leading electron f_1 (left) and of the subleading electron f_2 (right) for $1.52 < |\eta| < 2.01$ (top), $2.01 < |\eta| < 2.37$ (middle), and $2.37 < |\eta| < 2.47$ (bottom) are shown. In blue the fake rates estimated with the single object method and in red (jet trigger) and black (electron trigger) the results of the two tag and probe methods are shown.

8.2.3 *Real Electron Efficiency Estimation*

To calculate the real electron efficiency a sample with only real electrons is needed. The electron objects are well described in the Monte Carlo simulation and the same reconstruction algorithm as for data is used. Therefore it was possible to calculate the real electron efficiency on the signal Drell-Yan Monte Carlo sample. To get even better agreement between data and the Monte Carlo sample all corrections mentioned in Section 5.3 were applied. The efficiency was calculated using $r_{1,2} = N^{real}_{tight}/N^{real}_{loose}$. The indices loose and tight refer to the selections mentioned in Section 8.2.2. A truth matching was applied to select only real electrons from the hard process. Therefore, the reconstructed electrons had to match an electron from Z/γ^* decay at generator level within $\Delta R < 0.1$. Again a separation between the efficiency r_1 for the leading electron and r_2 for the sub-leading electron was made. As for the fake rate the efficiency was calculated for five different regions in $|\eta|$ separately. The resulting real electron efficiencies are shown in Figure 8.6 for the different η regions.

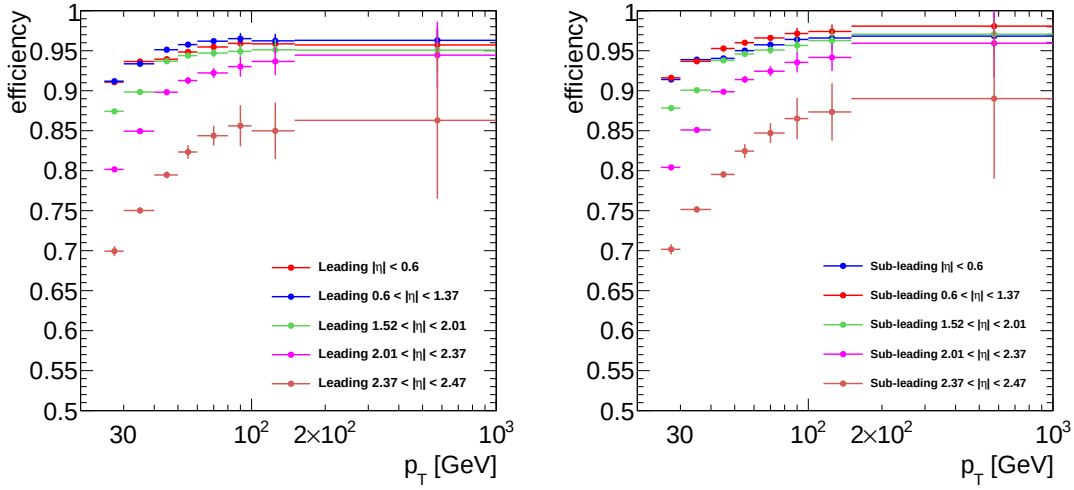

Figure 8.6: The p_T^{elec} dependency of the real electron efficiency r_1 (left) and r_2 (right) separated for the different η ranges.

The behavior for leading and sub-leading electrons is the same. For the barrel region the efficiencies are between 92% and 98% and for the end-cap region they are between 70% and 96%. For all detector regions the efficiency increases with transverse momentum before reaching a plateau at around 80 GeV. Due to the fact that the efficiency is very high and all events passing the tight selection are also included in the loose selection binomial uncertainties were used.

8.2.4 *Fakeable Object Selection*

The objects to which the fake rates, fake factors and real electron efficiencies are applied are called fakeable objects. They are identical with N_{TL}, N_{LT} and N_{LL} mentioned in Section 8.2.1. They are selected by using the definition of "loose" and "tight" mentioned in Section 8.2.2. For N_{TL} events were selected where the object with higher p_T fulfills the leading signal selection and another object with lower p_T passed the "loose"

selection but fails at least one cut of the "tight" selection. For N_{LT} it is vise versa, and for N_{LL} both objects have to pass the "loose" and fail the "tight" selection. N_{TT} which is used in the matrix to correct for real electron contribution is identically with the signal selection. In difference to the signal selection all possible combinations were used if in an event three or more objects were found and not only the pair with the highest p_T. This is important because each combination has the possibility to fake a signal event, where the probability is given by the product of the corresponding fake rates.
Figure 8.7 shows the raw distributions of the three fakeable object pairs after the selection.

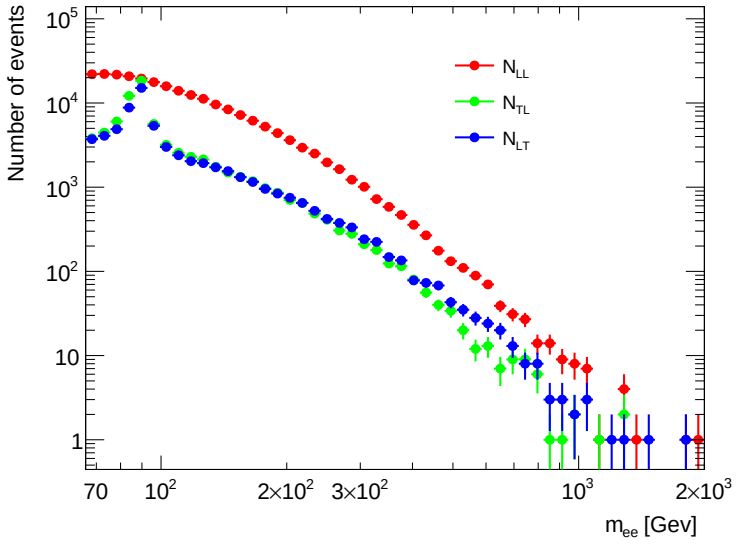

Figure 8.7: N_{TL}, N_{LT} and N_{LL} distributions without any correction and without fake rates applied.

The spectrum of N_{LL} shows a smooth behavior as expected. For the other two plots a peak around the invariant mass of the Z-boson is clearly visible. This peak is coming from events with two real electrons, where one of them does not pass the signal selection and is selected as "loose" fail "tight". In the plots it is direct visible for Z-boson events but it is also true for all other sources with two real electrons.
In case were the variation of the matrix method described in Section 8.2.1 were used an additional correction is needed. To correct for remaining events with two real electrons the method to obtain the fakeable objects was also applied on all Monte Carlo samples with contributions of two real electrons in final state. The resulting distributions, after applying the matrix method and the fakeable objects were summed up using Equation 8.13 are shown in Figure 8.8a. To get the final "Dijet & W+jets" background from this variation the distributions derived from the Monte Carlo samples were subtracted from the ones obtained from data. For the default, where the matrix method without simplification is used, this effect is already considered in Equation 8.5 and no further corrections are needed. The final spectrum in an equidistant logarithmic binning is shown in Figure 8.8b.

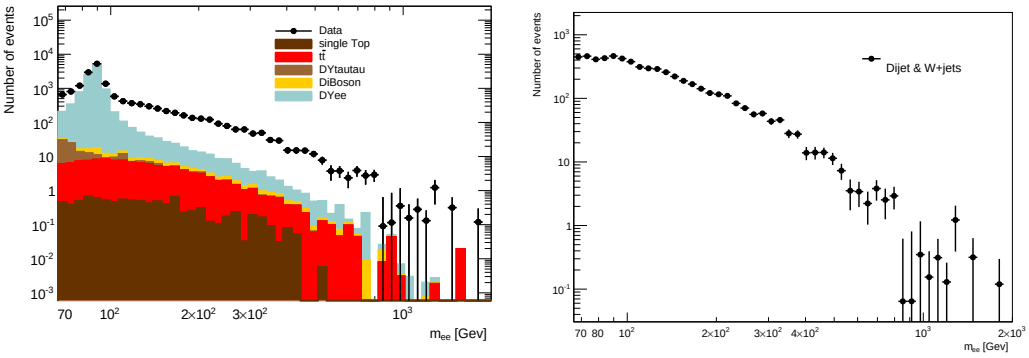

(a) (b)

Figure 8.8: On the left side the distributions estimated from the $r = 1$ method for data after applying the fake factors is shown. The correction for real electron contribution is not applied. The amount of this correction is given by the stacked Monte Carlo contributions. On the right side the final "Dijet & W+jets" contribution estimated with the default method in an equidistant logarithmic binning is shown.

8.3 UNCERTAINTIES

8.3.1 *Real Electron Background*

The background with two real electrons in the final state were estimated with the help of Monte Carlo simulations. There are two main effects which were taken into account. First the uncertainty coming from the theoretical knowledge of the production cross-section of the processes. This was assumed to be 5% for the diboson production [93], 6% for the $t\bar{t}$ cross-section [94][98] and 7% for the single top process [95]. The second contribution is the statistical limitation of the available Monte Carlo samples. All other sources of uncertainties for these background components like energy-resolution correction or the different efficiency scale factors are negligible. The resulting uncertainty as well as the single components are given in Table 8.3.

8.3.2 *Fake Electron Background*

Uncertainty on Fake Rate Estimation

To estimate the uncertainty on the single jet method which was chosen as default, multiple cut variations were done. The cleaning cut on missing transverse energy (MET) to remove real electrons from W-boson decays were vary up to 30 GeV and down to 20 GeV. The window size for the cut on the invariant mass to suppress real electrons from Z-boson decay was varied by 10 GeV up and down. The variations were done for each η region and leading and sub-leading electrons separately and the largest deviation for each bin was taken as systematic uncertainty on the fake rate estimation. In Figure 8.9 the result is shown exemplary for the leading electron in the inner mosts barrel region.

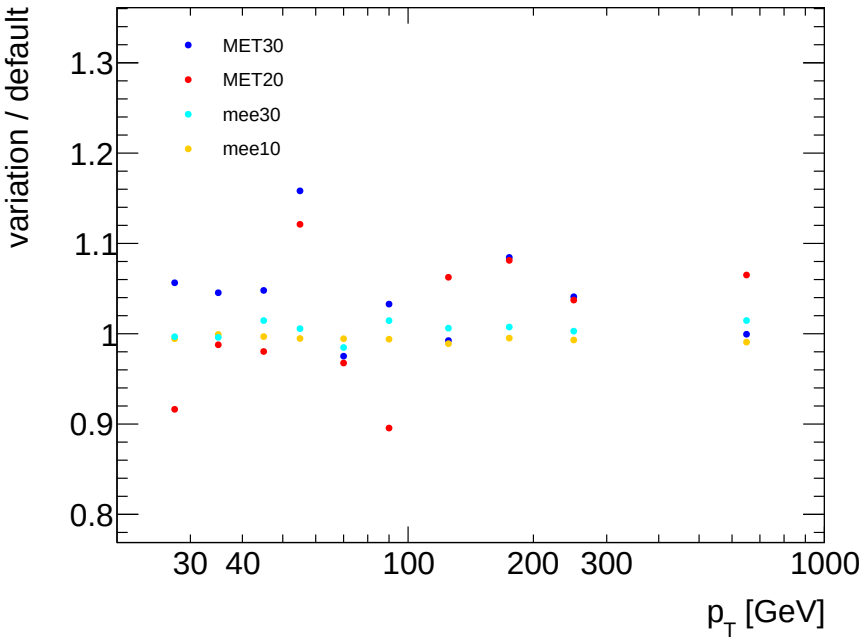

Figure 8.9: The influence of different cut variations on the estimated fake rates are shown. The changes was performed on the different cleaning cuts.

Uncertainty on the Fake Electron Background

To estimate the uncertainty the fake background method different variations were used and the results were compared to the default method. Instead of the full matrix method the simplification with $r_{1,2} = 1$, as described in Section 8.2.1, was used to get a feeling about the stability of the method. In addition the two other sets of fake rates, estimated with the other methods were applied to both matrix methods. This leads to five different background estimations compared to the reference method.
The ratios between the default method and the different variations are plotted in Figure 8.10.
As systematic uncertainty on the fake background method the largest deviation for each bin was used. To propagate the statistical and systematic uncertainties of the fake rate estimation the default fake rates were shifted up and down by the statistical and systematic uncertainties, estimated as described in Section 8.3.2. Afterwards, the uncertainties of the method, the statistical uncertainty on the fake rate and the systematic uncertainty on the fake rate were summed up quadratically. The uncertainty contributions together with the resulting total uncertainty are shown in Figure 8.11.
With respect to the published result, where an flat uncertainty of 20% for each bin was used the relative uncertainty gets larger. This is caused by the reduced fake background due to the tighter identification cuts. Nevertheless, the absolute uncertainties are smaller compared to the published result.

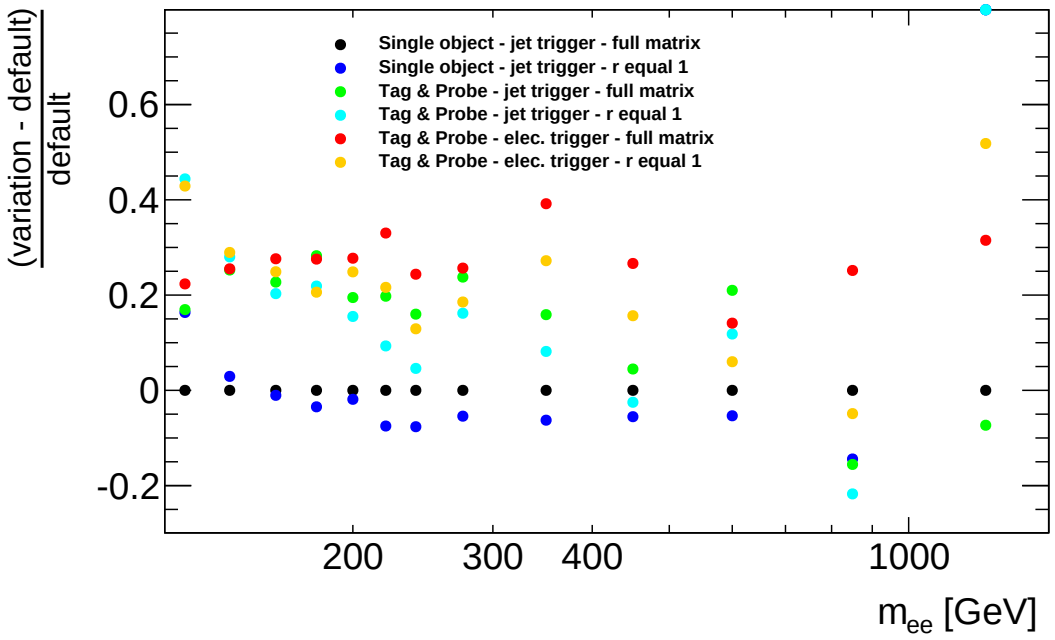

Figure 8.10: Variations of the background method compared to the default method.

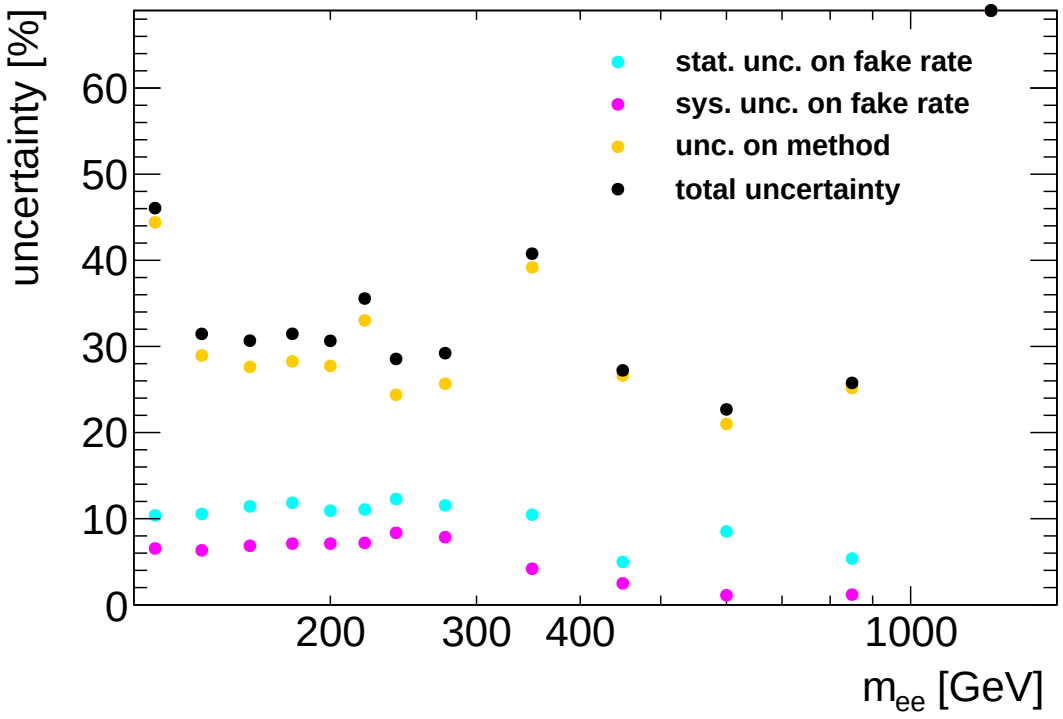

Figure 8.11: Total uncertainty on the fake background estimation (black) in percent. In addition the uncertainty on the method (yellow), the uncertainty due to statistical uncertainty on the fake rate estimation (blue) and the uncertainty due to the systematic uncertainty on the fake rate estimation (magenta) are shown.

8.4 SUMMARY OF BACKGROUND AND NUMBER OF SIGNAL EVENTS

In Table 8.3 all background contributions with their statistical and systematic uncertainties are shown together with the resulting number of signal events and their uncertainties.

Table 8.3: Summary of the number of selected events, background events and number of signal events in bins of m_{ee}. The number of background events are separated for the different background components and are shown together with the statistical and systematic uncertainties. The number of signal events (N_{Sig}) are the shown together with the statistical uncertainty of the selected data (Data stat.) and the total systematic uncertainty (Tot sys.), where all uncertainties on the background are summed up quadratically.

m_{ee} [GeV]	116-130	130-150	150-170	170-190	190-210	210-230
data	8436	6056	3226	1930	1314	801
QCD & W+jet	$139 \pm 7 \pm 62$	$147 \pm 7 \pm 43$	$103 \pm 5 \pm 29$	$81 \pm 5 \pm 23$	$51 \pm 4 \pm 14$	$37 \pm 3 \pm 12$
diboson	$90 \pm 2 \pm 5$	$95 \pm 2 \pm 5$	$68 \pm 2 \pm 3$	$51 \pm 1 \pm 3$	$37 \pm 1 \pm 2$	$28 \pm 1 \pm 1$
$t\bar{t}$	$273 \pm 4 \pm 16$	$308 \pm 4 \pm 18$	$229 \pm 3 \pm 14$	$165 \pm 3 \pm 10$	$116 \pm 2 \pm 7$	$88 \pm 2 \pm 5$
single top	$27 \pm 2 \pm 2$	$32 \pm 2 \pm 2$	$26 \pm 2 \pm 2$	$15 \pm 1 \pm 1$	$11 \pm 1 \pm 1$	$11 \pm 1 \pm 1$
N_{Sig}	7907	5474	2800	1618	1100	637
$\pm$ Data stat.	92	78	57	44	36	28
$\pm$ Tot sys.	68	54	37	29	19	16

m_{ee} [GeV]	230-250	250-300	300-400	400-500	500-700	700-1000	1000-1500
data	604	870	629	198	110	29	5
QCD & W+jet	$31 \pm 3 \pm 8$	$49 \pm 3 \pm 13$	$42 \pm 3 \pm 17$	$9 \pm 2 \pm 3$	$7 \pm 1 \pm 1$	$1.5 \pm 0.6 \pm 0.4$	$0.1 \pm 0.2 \pm 0.4$
diboson	$21 \pm 1 \pm 1$	$34 \pm 1 \pm 2$	$28 \pm 1 \pm 1$	$9 \pm 0.2 \pm 0.5$	$5 \pm 0.1 \pm 0.3$	$1.4 \pm < 0.1 \pm 0.1$	$0.3 \pm < 0.1 \pm < 0.1$
$t\bar{t}$	$61 \pm 2 \pm 4$	$90 \pm 2 \pm 5$	$63 \pm 2 \pm 4$	$17 \pm 1 \pm 1$	$6 \pm 0.6 \pm 0.4$	$0.4 \pm 0.2 \pm < 0.1$	$0.1 \pm 0.1 \pm < 0.1$
single top	$7 \pm 1 \pm 1$	$8 \pm 1 \pm 1$	$9 \pm 1 \pm 1$	$3 \pm 1 \pm 0.2$	$1 \pm 0.4 \pm 0.1$	$0.1 \pm 0.1 \pm < 0.1$	$0.1 \pm 0.1 \pm < 0.1$
N_{Sig}	483	689	487	160	91	26	4.4
$\pm$ Data stat.	25	29	25	14	10	5	2.2
$\pm$ Tot sys.	10	16	18	4	2	0.8	0.5

For the number of signal events (N_{Sig}) the sum of all background components was subtracted from the number of selected events. The statistical uncertainty of N_{Sig} is propagated from the statistical uncertainty on data only. For the systematic uncertainty the statistical and systematic uncertainties from the different background contributions are summed up quadratically.

8.5 CONTROL PLOTS

To prove that the background estimation and the Monte Carlo corrections work fine the data distribution for different variables are plotted together with signal Monte Carlo and all background contributions as discussed above. To give a better feeling for the agreement plots of the ratio of data and the sum of signal Monte Carlo and background are attached to each plot. The spectrum of the invariant mass of the di-electron system is shown in Figure 8.12 in an equidistant logarithmic binning and in Figure 8.13 in the binning of the measurement.
Over all there is a good agreement within the statistical uncertainty, but the data is $\sim 5\%$ higher than the sum of signal Monte Carlo and background predictions. A shift

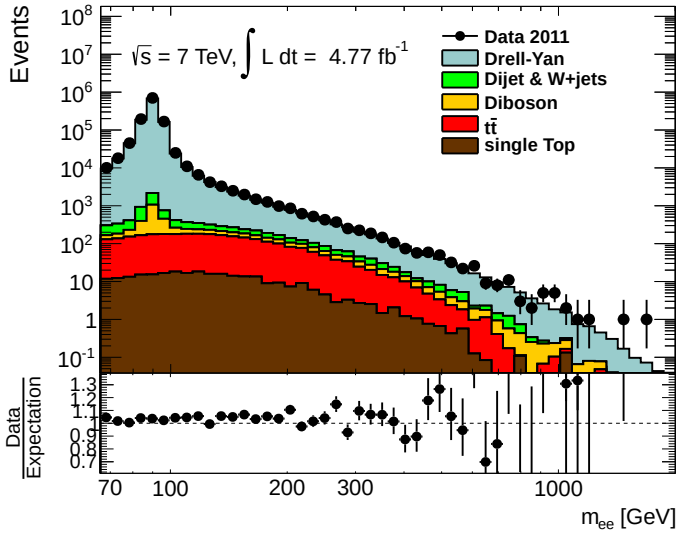

Figure 8.12: Distribution of m_{ee} from data compared to signal Monte Carlo sample (PYTHIA) corrected to NNLO and all backgrounds in an equidistant logarithmic binning.

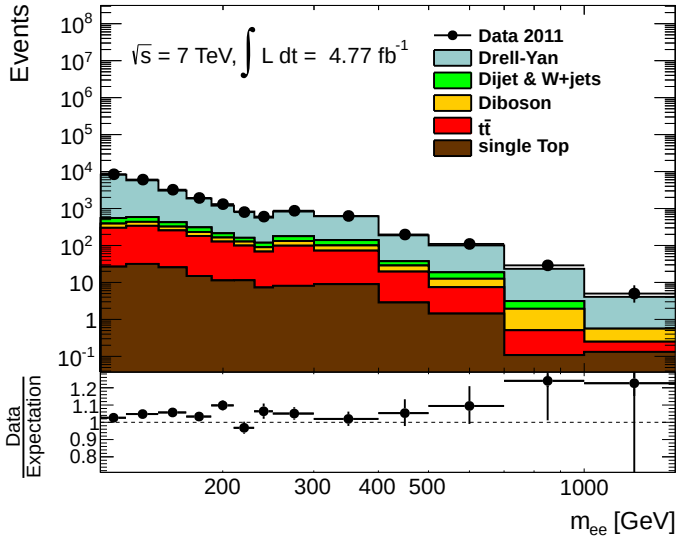

Figure 8.13: Distribution of m_{ee} from data compared to signal Monte Carlo sample (PYTHIA) corrected to NNLO and all backgrounds in the binning of the measurement (right).

of around 3% was already visible in Ref. [42]. After publication of the paper the luminosity measurement for 2011 was corrected by the responsible ATLAS group [75]. The central luminosity value was corrected down by 1.7%. The signal and background Monte Carlo samples are normalized to the integrated luminosity. This explains why the disagreement gets larger by ~ 2%.

In addition the spectra of the transverse momentum (p_T) of the selected leading and sub-leading electrons are shown in Figure 8.14 and Figure 8.15.

The distributions are shown for different ranges of m_{ee}. As expected the distributions show a peak at around half of the invariant mass with a strongly falling tail. Also in these plots the overall 5% effect is visible. The agreement of the shapes are very good and for low p_T the data driven background (green area) fits perfect. The differences

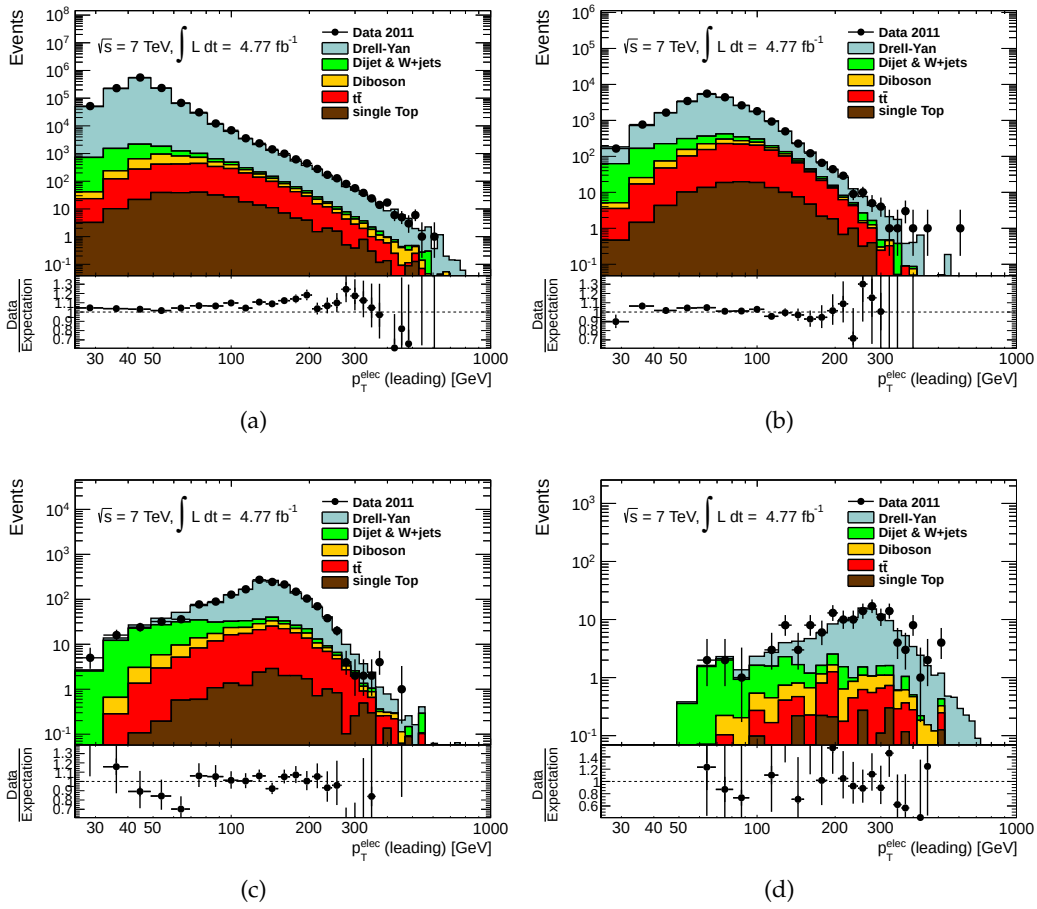

Figure 8.14: Distributions of p_T of the leading electrons are shown. Separated in different ranges of m_{ee}. Complete range (a), $116\,GeV < m_{ee} < 250\,GeV$ (b), $250\,GeV - 500\,GeV$ (c) and $500\,GeV < m_{ee} < 1500\,GeV$ (d) are shown. Data (black points) is compared to signal Monte Carlo (PYTHIA) and all backgrounds.

between the spectra of the leading and the sub-leading electrons are clearly visible.
Figure 8.16 shows the pseudorapidity (η) distributions of both electrons.
In the plots different mass ranges are shown. The distributions show the typical behavior, where the number of events gets smaller for larger values of $|\eta|$. This is caused by the $p_T > 25$ GeV requirement on the electrons. Objects in the forward regions need higher energy for the same value of p_T.Therefore, more events are cut away. For larger values of $|\eta|$ the fake background contribution gets larger. This is caused by the fact, that the jet production cross-section is larger for more forward regions. The vetoed region between the barrel and the end-cap part of the electromagnetic calorimeter is visible. The agreement within the statistical uncertainty is good.
The angle ϕ of the selected electrons is shown in Figure 8.17.
As expected the events are uniformly distributed over the angle ϕ. This is true for data as well as for the signal Monte Carlo and all background contributions. In Figure 8.17a the cut to remove electrons close to the region with dead calorimeter cells is visible at $\phi = -1$ The drop down at the edges at π and $-\pi$ is due to the chosen binning.
In Figure 8.18 the transverse momentum of the di-electron system is shown.

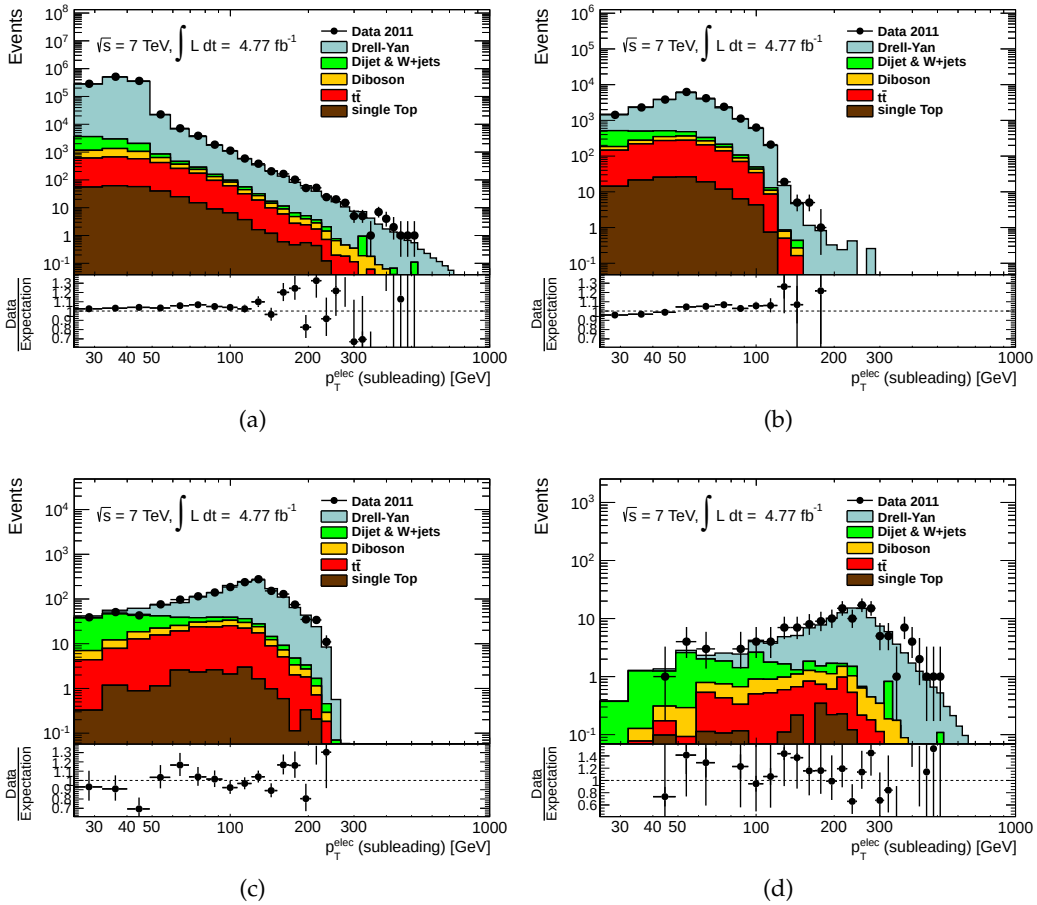

Figure 8.15: Distributions of p_T of the sub-leading electrons are shown. Separated in different ranges of m_{ee}. Complete range (a), $116\,\text{GeV} < m_{ee} < 250\,\text{GeV}$ (b), $250\,\text{GeV} - 500\,\text{GeV}$ (c) and $500\,\text{GeV} < m_{ee} < 1500\,\text{GeV}$ (d) are shown. Data (black points) is compared to signal Monte Carlo (PYTHIA) and all backgrounds.

The distributions show the typically strong falling behavior. For the plot without a cut on the invariant mass (Figure 8.18a) there is a larger discrepancy in the region between 200 GeV and 400 GeV. In the other spectra this discrepancy is not visible which means that the discrepancy is coming from the Z-peak region which is not part of this work. It is clearly visible that for the ranges with high invariant mass the p_T of the di-electron system on average is smaller then for low mass. This is expected because with the production of objects with high invariant mass less energy to boost the produced object in the transverse plane is available.
The spectrum of the rapidity of the di-electron system is shown in Figure 8.19.
The maximum of the distribution is around zero and drops down slightly to the edges. The upper bound is the absolute value of 2.47 for this measurement. This is only realizable if both electrons are at the edge of the electromagnetic calorimeter and back to back in the ϕ plane. Since the rapidity is a quantity of the boost of the boson the phase space becomes smaller with higher invariant masses. This is clearly visible in Figure 8.19c and Figure 8.19d. The comparison between data and the signal Monte Carlo plus all backgrounds shows good agreement over the whole invariant mass range.

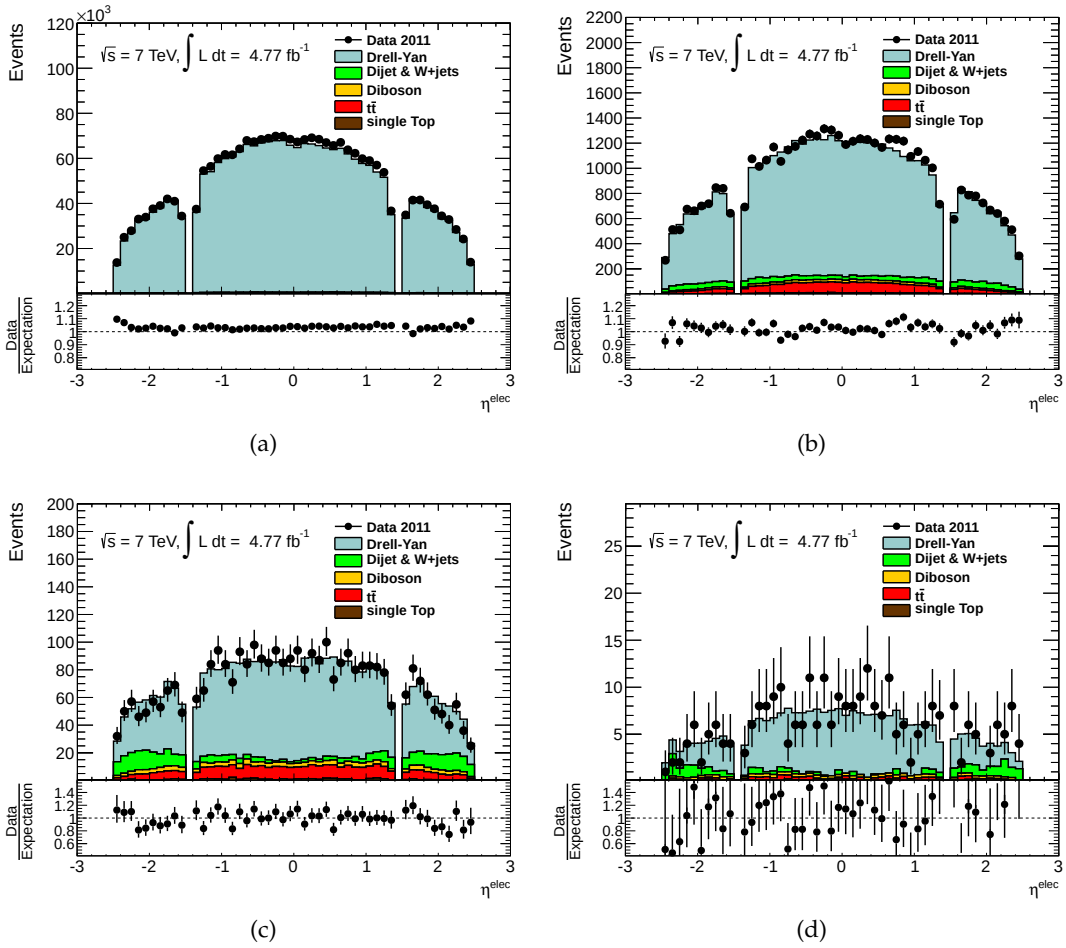

Figure 8.16: η distribution of all electrons passing the selection. Separated in different ranges of m_{ee}. Complete range (a), $116\,\mathrm{GeV} < m_{ee} < 250\,\mathrm{GeV}$ (b), $250\,\mathrm{GeV} - 500\,\mathrm{GeV}$ (c) and $500\,\mathrm{GeV} < m_{ee} < 1500\,\mathrm{GeV}$ (d) are shown. Data (black points) is compared to signal Monte Carlo (PYTHIA) and all backgrounds.

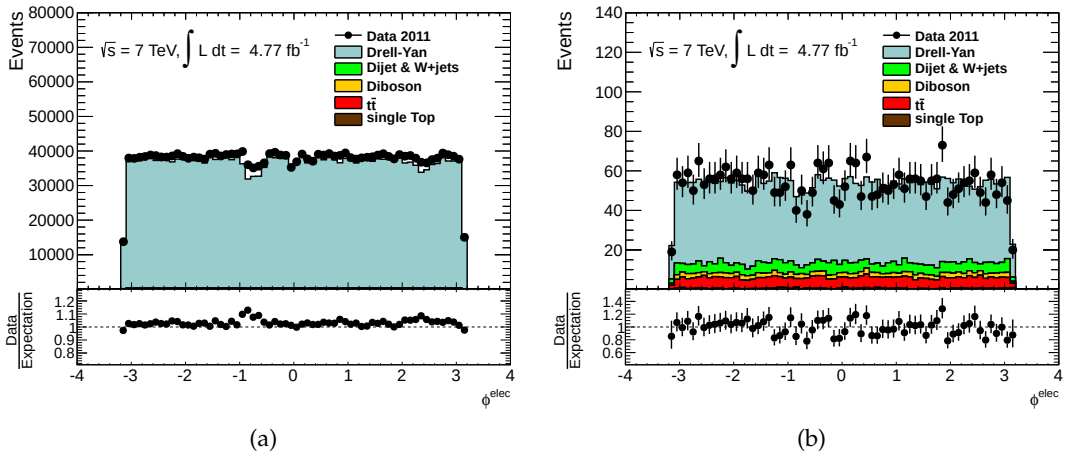

Figure 8.17: ϕ distribution of all electrons passing the selection. Separated in different ranges of m_{ee}. Complete range (a) and $250\,\mathrm{GeV} - 500\,\mathrm{GeV}$ (b) are shown. Data (black points) is compared to signal Monte Carlo (PYTHIA) and all backgrounds.

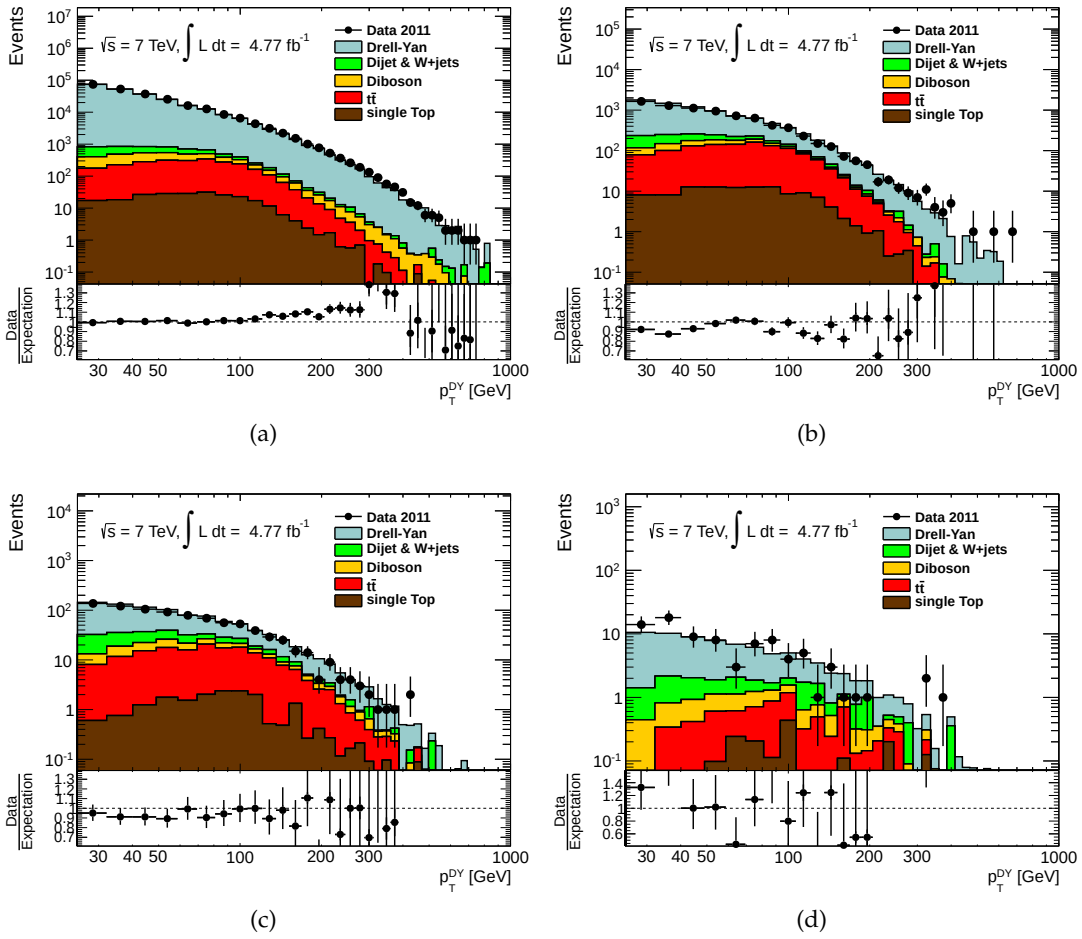

Figure 8.18: p_T distribution of the di-electron system. Separated in different ranges of m_{ee}. Complete range (a), $116\,\mathrm{GeV} < m_{ee} < 250\,\mathrm{GeV}$ (b), $250\,\mathrm{GeV} - 500\,\mathrm{GeV}$ (c) and $500\,\mathrm{GeV} < m_{ee} < 1500\,\mathrm{GeV}$ (d) are shown. Data (black points) is compared to signal Monte Carlo (PYTHIA) and all backgrounds.

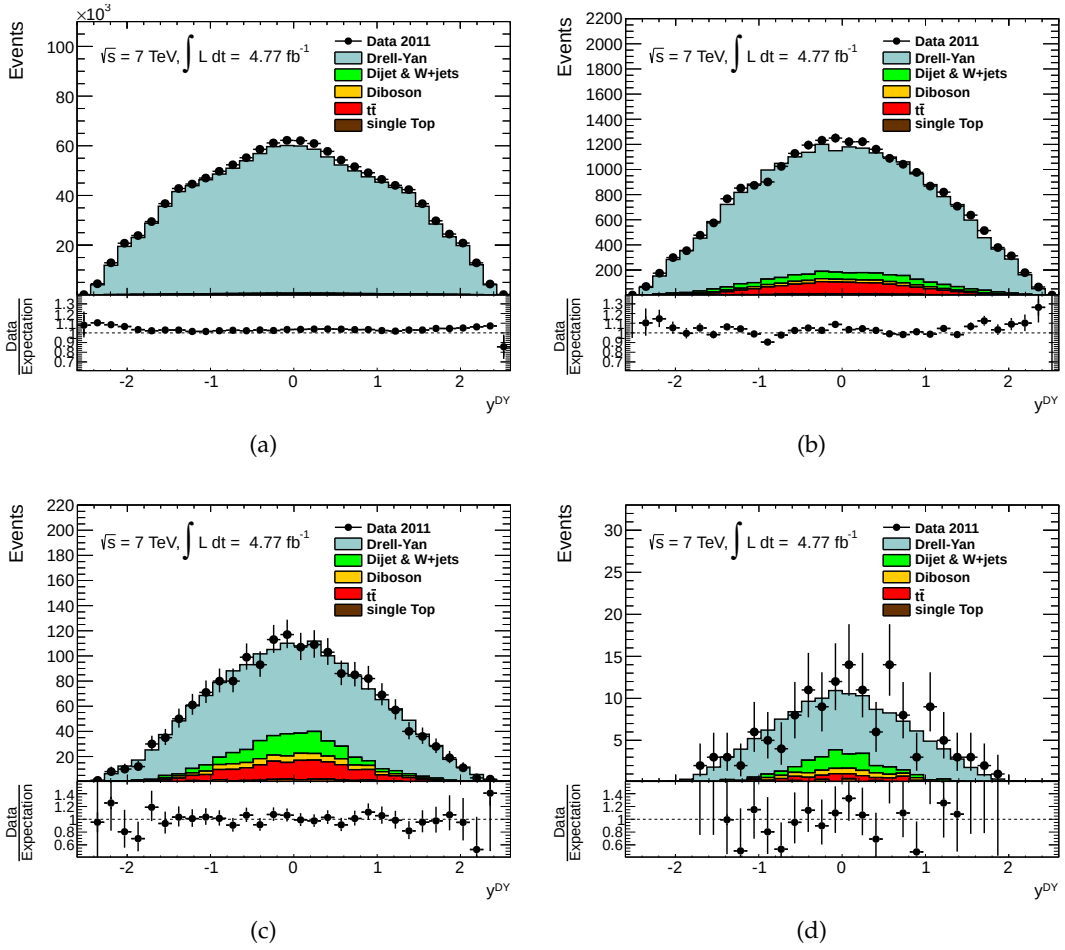

Figure 8.19: Rapidity distribution of the di-electron system. Separated in different ranges of m_{ee}. Complete range (a), $116\,\mathrm{GeV} < m_{ee} < 250\,\mathrm{GeV}$ (b), $250\,\mathrm{GeV} - 500\,\mathrm{GeV}$ (c) and $500\,\mathrm{GeV} < m_{ee} < 1500\,\mathrm{GeV}$ (d) are shown. Data (black points) is compared to signal Monte Carlo (PYTHIA) and all backgrounds.

9

UNFOLDING

The differential cross-section in bins of the invariant mass m_{ee} was calculated using Equation 9.1

$$\frac{d\sigma_{fid}}{dm_{ee}} = \frac{N_{sig}}{C_{DY}\, L_{int}} \frac{1}{\Delta m_{ee}} \tag{9.1}$$

where N_{sig} is the number of selected events after background subtraction as described in Section 7 and Section 8, C_{DY} is the correction factor for detector effects as described in this section, and L_{int} is the integrated luminosity of the data collected by the ATLAS experiment in 2011.

Born, Bare, Dressed
In general the cross-section can be measured with respect to different levels of quantum electrodynamics (QED) final state radiation (FSR) corrections. This leads to different definitions of the truth level for the electrons:

- Born level: Electrons before QED final state radiation are used. This allows to perform a full QED correction during the unfolding.
- "bare" level: Electrons after QED final state radiation are used. This allows an unfolding without any QED corrections.
- "dressed" level: In this case a hybrid of the two others is used. The Lorentz-vector of the bare electron is used and all QED FSR photons within a cone of $\Delta R < 0.1$ are re-summed to the vector. The result is a partial QED FSR correction, taking only the collinear radiation into account.

For this measurement the final cross-section was calculated at Born and at "dressed" level. Therefore also the correction C_{DY} were calculated for electrons on both truth levels. The cross-section was extrapolated to a common fiducial region with $p_T^{elec} > 25\,\text{GeV}$ and $|\eta|^{elec} < 2.5$. To extrapolate the cross-section from the selected events the background was subtracted and afterwards an unfolding was performed. The unfolding is required to correct the distribution for detector and migration effects. Migration means that the reconstructed object has a different mass then the object produced at the hard process.

9.1 PURITY

The purity is defined as the fraction of events which were reconstructed and generated in the same mass bin with respect to all events reconstructed in this bin. Figure 9.1 shows the purity in bins of the invariant mass.

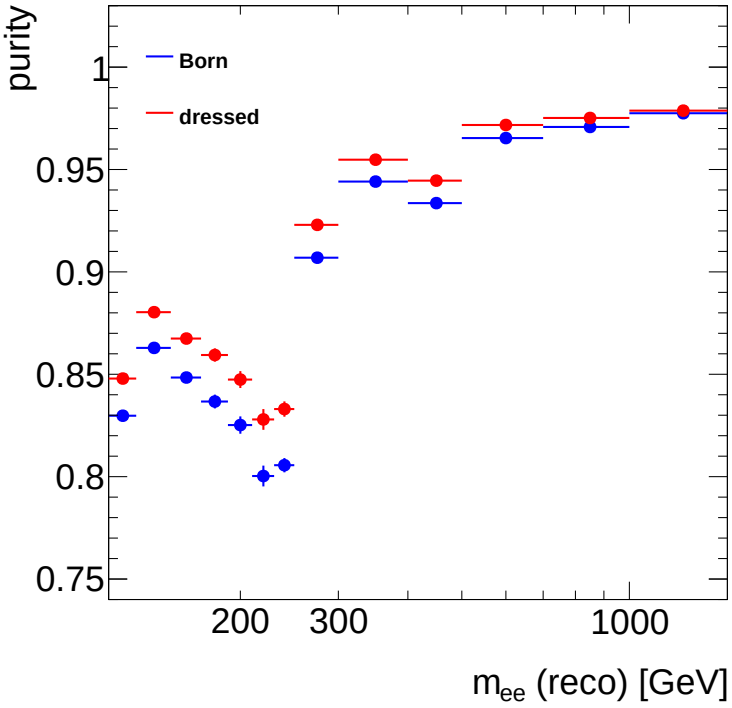

Figure 9.1: Fraction of events where reconstructed and generated mass fall in the same bin with respect to all events reconstructed in this bin. The purity is shown for the truth mass at Born level (blue) and at "dressed" level (red) estimated from the PYTHIA signal sample.

The values are between 80% and 98%. With larger bin size the migration effects are getting smaller. The reconstruction and identification efficiencies get better with higher p_T of the electrons and therefore corresponding higher invariant mass. In the case where the truth mass was calculated using "dressed" electrons the purity is always a little bit higher. In most bins the effect is on the order of 4% but the distribution shows the same behavior as for Born level. This is expected because the electrons at "dressed" level are more like the reconstructed electrons compared to the electrons at Born level. Therefore, the reconstruction inefficiency and the migration effects becomes slightly smaller.

9.2 CENTRAL VALUE OF C_{DY}

Due to the good purity in the chosen binning it was possible to use a bin-by-bin method[1]. For each bin the correction factor C_{DY} was calculated using Equation 9.2.

$$C_{DY} = \frac{N_{MCreco}}{N_{MCgenfid}}, \tag{9.2}$$

where N_{MCreco} is the number of events after reconstruction and selection obtained from the signal MC sample with all weights applied and $N_{MCgenfid}$ the number of events after applying the fiducial cuts ($|\eta| < 2.5$ and $p_T > 25\,GeV$) on truth level[2]. This also includes the small acceptance correction over the transition region between barrel and endcap and up to $|\eta| < 2.5$.
C_{DY} was calculated using the $pp \to Z/\gamma^* + X \to ee + X$ signal sample generated with the PYTHIA generator. To get a feeling of the influence of the chosen generator the procedure was also done with samples generated with the MC@NLO and SHERPA generators. The SHERPA generator delivers no information about the electrons at Born level. Therefore, this MC can only be used to calculate the cross-section at "dressed" level. The result of the different generators is shown in Figure 9.2.

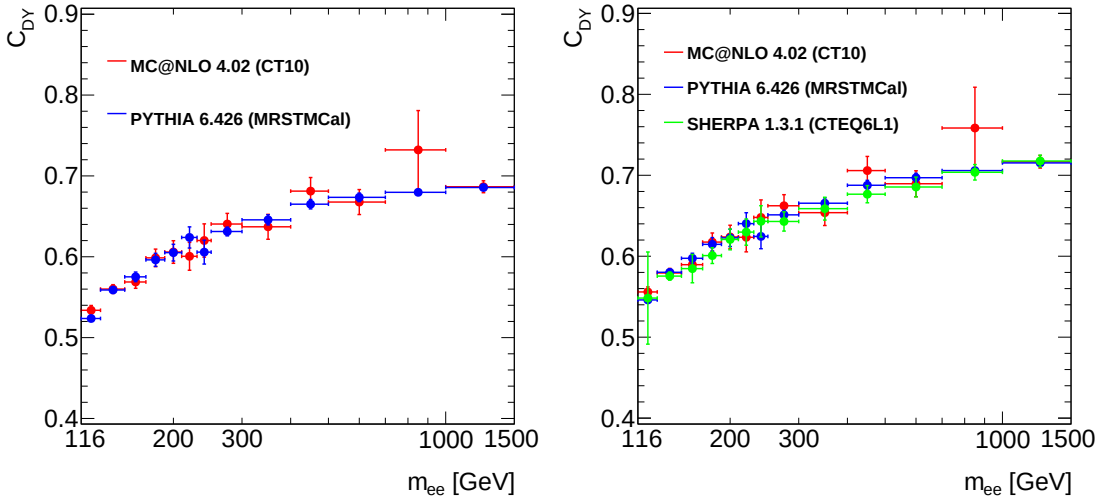

Figure 9.2: The central value of C_{DY} is shown to unfold the signal events to Born level (left) and to "dressed" level (right). The result for Born is shown for PYTHIA (blue) and MC@NLO (red) generator and for "dressed" in addition also for SHERPA (green).

The results from all generators used agree within the statistical uncertainties. The values calculated with the PYTHIA Monte Carlo samples were taken as default, because these samples has the highest statistics. Furthermore, no uncertainty related to the choice of the generator was applied.

1 Bin-by-bin method means that C_{DY} is calculated and applied for each bin separately.
2 Before the detector simulation was applied to the generated events.

PDF-XChange Editor Click to BUY NOW! tracker-software.com

9.3 UNCERTAINTIES

To estimate the uncertainty of C_{DY} different methods were used which will be described in this section. To estimate the effect of the reweighting of the Monte Carlo samples for pile-up, Z p_T, z-vertex position and k-factors, C_{DY} was calculated with and without the reweighting applied. This was done for each component separately and the difference to the central value was used as systematic uncertainty.
The uncertainties related to the reconstruction scale factor (SF), identification SF and trigger SF were estimated using a complete up-down variation of the corresponding uncertainties by one sigma. This is a very conservative estimate but necessary because there was no separation between correlated and uncorrelated uncertainties available for these scale factors. These variations have only influence of N_{MCreco}. Therefore, the uncertainty was calculated from the relative difference between the central value of N_{MCreco} and the result of the up and down variations. As final uncertainty the mean of these two variations was used.
For the energy correction two effects were taken into account. The correction of the energy resolution of the Monte Carlo sample which is described in detail in Section 5.3.3 and the energy correction applied to data. The uncertainty related to the latter one was also estimated with the help of the Monte Carlo sample. This was done because the Monte Carlo sample provides better statistic, especially for events with high invariant mass. This was possible because for both, data and Monte Carlo, the same reconstruction algorithm was used and the detector simulation of the Monte Carlo fits to the data as shown in Section 8.5. The uncertainty on the energy resolution was estimated by the difference on C_{DY} whether applying the smearing to the simulation or not. The uncertainty on the energy correction was available separated in statistical and systematic components. The systematic component was handled in the same way as the scale factors. The central value of N_{MCreco} was compared to the result when the energy correction was varied by one sigma up or down. Again the mean value of the two variations was taken as uncertainty. The statistical and therefore uncorrelated component of the energy correction was treated in a different way.
One thousand pseudo-experiments were performed to obtain the uncertainty. The energy correction is available as an η dependent matrix. In each pseudo-experiment a random number of a Gaussian distribution with mean of zero and a width of one was drawn for each bin. This procedure provides a random number which is in 67% of the cases between -1 and 1. During one iteration the random number was always kept the same for objects which belongs to the same η bin. The random number was then multiplied with the one sigma statistical uncertainty of the energy correction. Afterwards the energy correction was shifted by this factor before applying it to the electron object. The thousand resulting distributions of N_{MCreco} were plotted and the result of two exemplary bins is shown in Figure 9.3. The mean and the standard deviation of these distributions were calculated and the latter was used as final uncertainty due to the energy correction.
To evaluate the total systematic uncertainty all single components were summed up quadratically. The central value of C_{DY} calculated at Born level using the PYTHIA simulation as well as the statistical and all systematic uncertainties are summarized in Table 9.1. For "dressed" level the uncertainties are identical.

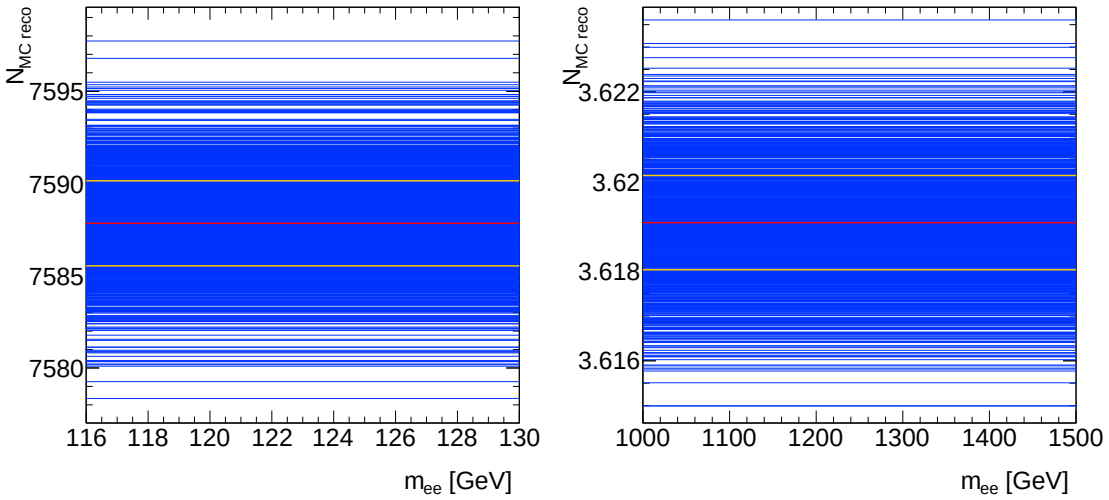

Figure 9.3: The distribution of N_{MCreco} shown for all pseudo-experiments for the bin 116 GeV $< m_{ee} <$ 130 GeV and 1000 GeV $< m_{ee} <$ 1500 GeV. The mean and the standard deviation are indicated by the red and yellow lines.

Table 9.1: Statistical (from MC statistics) and systematic relative uncertainties on C_{DY} with respect to Born level, calculated with PYTHIA. The values are given in percent. The sources of the systematic uncertainty are trigger efficiency, reconstruction efficiency, identification (ID) efficiency (which combines the medium, B-layer and isolation (for leading electron) requirements), energy scale (separated in systematic and statistical component), energy resolution, pileup, description of Z transverse momentum distribution (Z_{pt}) influence of z-vertex reweighting and the influence of extrapolation to NNLO theory (k-factor). In addition the central value of C_{DY} with the statistical uncertainty is given for comparison.

m_{ee}^{min} [GeV]	m_{ee}^{max} [GeV]	C_{DY}	stat.	Trig. Eff.	Rec. Eff	ID Eff	E-scale sys.	E-scale stat.	E-res	pileup	Z_{pt}	z-vertex	k-factor	Unfolding	total sys
116	130	0.524	0.8	0.9	1.0	1.0	0.8	0.0	0.1	0.1	0.0	1.2	0.1	1.5	2.7
130	150	0.559	0.7	0.9	1.0	1.1	0.7	0.0	0.1	0.1	0.0	0.9	0.1	1.5	2.5
150	170	0.575	1.0	0.9	1.0	1.1	0.7	0.0	0.4	0.1	0.0	0.9	0.0	1.5	2.6
170	190	0.596	1.4	0.9	0.9	1.1	0.6	0.0	0.4	0.0	0.1	0.6	0.0	1.5	2.4
190	210	0.605	1.7	0.9	0.9	1.1	0.8	0.1	0.1	0.1	0.0	0.1	0.0	1.5	2.4
210	230	0.624	2.1	0.9	0.9	1.1	1.2	0.1	0.1	0.0	0.1	1.1	0.0	1.5	2.8
230	250	0.606	2.4	0.9	0.9	1.1	1.1	0.1	0.3	0.1	0.0	0.7	0.0	1.5	2.6
250	300	0.631	0.9	0.9	0.9	1.1	1.3	0.0	0.4	0.1	0.1	0.8	0.0	1.5	2.8
300	400	0.646	1.0	0.9	0.9	1.1	1.5	0.0	0.0	0.1	0.1	0.6	0.1	1.5	2.8
400	500	0.665	0.9	0.8	0.9	1.1	2.2	0.0	0.1	0.1	0.1	0.8	0.1	1.5	3.2
500	700	0.673	0.8	0.8	0.9	1.1	2.4	0.0	0.0	0.1	0.0	1.1	0.1	1.5	3.5
700	1000	0.680	0.6	0.8	0.9	1.1	2.8	0.0	0.1	0.1	0.0	1.0	0.1	1.5	3.7
1000	1500	0.686	0.4	0.8	0.9	1.0	3.3	0.0	0.1	0.2	0.0	1.2	0.2	1.5	4.1

The largest uncertainty is coming from the identification efficiency and the energy-scale correction. The uncertainties of trigger, reconstruction and identification efficiency are nearly the same over the whole mass range. Over all, the systematic uncertainty is between 2.4% and 4.1%. The binning of the Monte Carlo samples used is clearly visible

on the statistical uncertainties. Only one sample covering the range between 120 GeV and 250 GeV was available. Due to the fact that the production cross-section gets smaller with the invariant mass the uncertainty rise up to this point ($m_{ee} = 250$ GeV) and then drop down again.

10

RESULTS

In this section the resulting cross-sections at "Born" and "dressed" level are presented. The cross-sections are compared to theoretical predictions and cross-sections extracted from Monte Carlo generators.

10.1 THEORY PREDICTION

The theory predictions, which were used to compare to the final cross-sections, were calculated using FEWZ3.1[1] [99]. This version of FEWZ allows for the first time to calculate the Drell-Yan cross-section at NNLO in pQCD with electro-weak corrections at NLO applied. It is possible to calculate the cross-section for different sets of parton distribution functions (PDFs). The different PDFs were taken from the most recent version (5.8.8) of the library LHAPDF [100]. With FEWZ it is possible to perform the calculation for two different electroweak (EW) parameter schemes, called "G_μ" and "$\alpha(M_Z)$" due to the choices of the Standard Model input parameters as introduced in Ref. [101]. For the central values always the G_μ scheme was used where the values of α_G and $\sin^2(\theta_W)$ were calculated based on G_μ, M_Z and M_W using the following relations:

$$1/\alpha_G = \sqrt{2} G_\mu M_W^2 (1 - M_W^2/M_Z^2)/\pi \quad \text{and} \quad \sin^2(\theta_W) = 1 - M_W^2/M_Z^2. \tag{10.1}$$

For the calculation the best known values of masses were used which are $G_\mu = 1.16637 \times 10^{-5} 1/\text{GeV}^2$, $M_W = 80.403\text{GeV}$, $M_Z = 91.1876\text{GeV}$ [22]. The $\alpha(M_Z)$ scheme was used for cross checks.
The theory prediction using the MSTW2008 [102] parton distribution function was calculated using the settings mentioned above. To get a feeling about the PDF sensitivity of the measurement the same calculation was also made for all other modern NNLO PDFs. These are CT10nnlo [103], HERAPDF15nnlo [104], ABM11 [105] and NNPDF23 [106]. All other calculations including the corrections mentioned below and the uncertainties as described in Section 10.1.1 were taken from Ref. [107] and are the same as already used in Ref. [42].
To estimate the effect of the influence of the non-resonant $\gamma\gamma \to l^- l^+$ background the cross-section was calculated with help of the MRST2004qed [108] PDF set. This is a quite old PDF set but the only one available with a prediction of the photon PDF.
In addition the prediction was corrected for real boson emission as described in Ref. [109]. Since the diboson background was already subtracted from data the remaining real boson emission was calculated using MADGRAPH 5 [110]. The effect was found to be

1 Fully Exclusive W, Z Production through NNLO in pQCD.

negligible for low masses and reaches 2% in the highest m_{ee} bin.
To extract the cross-section from the Monte Carlo simulations the number of events after the fiducial cuts ($p_T^{elec} > 25\,GeV$ and $|\eta^{elec}| < 2.5$) on generator level were normalized to the collected integrated luminosity.

10.1.1 *Theory Uncertainties*

The uncertainties applied to the FEWZ calculation using the MSTW2008 PDF were taken from Ref. [107]. The uncertainties correlated to the PDFs were evaluated at 68% confidence level on the PDF. In addition variations of α_s and the factorization and normalization scales based on the PDF has been performed. The resulting uncertainties together with the statistical uncertainty and the central value are presented in Table 10.1. The cross-sections with the statistical uncertainties of the different PDFs are shown in Table 10.2. The influence of the real boson correction and the photon induced process is shown in Table 10.3.

Table 10.1: FEWZ 3.1 predictions of the fiducial cross-section in pb/GeV in the G_μ scheme including electroweak corrections using the MSTWNNLO2008 PDF set, for the cross-section at Born level in the fiducial region (electron $p_T > 25$ GeV and $|\eta| < 2.5$). The statistical uncertainty and the uncertainties from the PDF error set (68%), the combined PDF error set and α_s, and the factorization and renormalization scales are shown in percent and are taken from Ref. [107].

m_{ee}^{min} [GeV]	m_{ee}^{max} [GeV]	$\frac{d\sigma_{fid}}{dm_{ee}}$ [pb]	Stat	+PDF	-PDF	+(PDF,α_s)	−(PDF,α_s)	Scales
116	130	2.131×10^{-1}	0.21	1.54	1.45	2.27	1.70	0.12
130	150	9.427×10^{-2}	0.21	1.51	1.41	2.16	1.65	0.01
150	170	4.600×10^{-2}	0.21	1.51	1.37	2.06	1.60	0.23
170	190	2.610×10^{-2}	0.19	1.52	1.36	2.00	1.57	0.27
190	210	1.607×10^{-2}	0.18	1.55	1.35	1.98	1.55	0.06
210	230	1.045×10^{-2}	0.16	1.58	1.34	1.97	1.54	0.19
230	250	7.116×10^{-3}	0.18	1.62	1.35	1.97	1.53	0.19
250	300	4.004×10^{-3}	0.15	1.68	1.37	1.97	1.52	0.48
300	400	1.433×10^{-3}	0.13	1.81	1.42	1.97	1.51	0.35
400	500	4.352×10^{-4}	0.09	2.00	1.51	2.00	1.58	0.44
500	700	1.160×10^{-4}	0.07	2.22	1.60	2.22	1.82	0.55
700	1000	1.894×10^{-5}	0.05	2.68	1.71	2.91	2.44	0.72
1000	1500	2.032×10^{-6}	0.04	3.73	2.11	4.30	3.68	0.99

10.2 FIDUCIAL CROSS SECTION

Figure 10.1 shows the cross-section at Born level in the fiducial region with $p_T > 25\,GeV$ and $|\eta| < 2.5$ and Figure 10.2 shows the same distribution but restricted to a region of $116\,GeV < m_{ee} < 500$ GeV.
As expected shows the cross-section a strongly falling behavior over six orders of magnitude. The systematic uncertainties are dominant in the region up to $m_{ee} = 200$ GeV and are in the order of 2.5% to 3%. The statistical uncertainties are 2% for low invariant

Table 10.2: FEWZ3.1 predictions of the fiducial cross-section in pb/GeV in the G_μ scheme including electroweak corrections using the HERAPDF1.5, CT10NNLO, ABM11NNLO and NNPDF2.3 PDF sets for the cross-section at Born level in the fiducial region (electron $p_T > 25$ GeV and $|\eta| < 2.5$). Statistical uncertainties are shown in percent and are taken from Ref. [107].

m_{ee}^{min}	m_{ee}^{max}	HERAPDF1.5		CT10NNLO		ABM11		NNPDF2.3	
[GeV]	[GeV]	$\frac{d\sigma_{fid}}{dm_{ee}}[\frac{pb}{GeV}]$	Stat [%]	$\frac{d\sigma_{fid}}{dm_{ee}}[\frac{pb}{GeV}]$	Stat [%]	$\frac{d\sigma_{fid}}{dm_{ee}}[\frac{pb}{GeV}]$	Stat [%]	$\frac{d\sigma_{fid}}{dm_{ee}}[\frac{pb}{GeV}]$	Stat [%]
116	130	2.179×10^{-1}	0.32	2.154×10^{-1}	0.29	2.223×10^{-1}	0.28	2.110×10^{-1}	0.14
130	150	9.574×10^{-2}	0.28	9.394×10^{-2}	0.28	9.782×10^{-2}	0.27	9.307×10^{-2}	0.14
150	170	4.693×10^{-2}	0.27	4.564×10^{-2}	0.26	4.761×10^{-2}	0.24	4.555×10^{-2}	0.13
170	190	2.672×10^{-2}	0.23	2.598×10^{-2}	0.24	2.710×10^{-2}	0.24	2.572×10^{-2}	0.13
190	210	1.642×10^{-2}	0.22	1.591×10^{-2}	0.26	1.665×10^{-2}	0.21	1.588×10^{-2}	0.11
210	230	1.072×10^{-2}	0.24	1.031×10^{-2}	0.22	1.087×10^{-2}	0.20	1.033×10^{-2}	0.11
230	250	7.293×10^{-3}	0.20	7.013×10^{-3}	0.20	7.349×10^{-3}	0.21	7.003×10^{-3}	0.11
250	300	4.098×10^{-3}	0.20	3.932×10^{-3}	0.18	4.128×10^{-3}	0.17	3.942×10^{-3}	0.09
300	400	1.472×10^{-3}	0.16	1.397×10^{-3}	0.15	1.476×10^{-3}	0.15	1.409×10^{-3}	0.09
400	500	4.446×10^{-4}	0.25	4.204×10^{-4}	0.12	4.456×10^{-4}	0.11	4.265×10^{-4}	0.06
500	700	1.177×10^{-4}	0.17	1.105×10^{-4}	0.09	1.175×10^{-4}	0.09	1.133×10^{-4}	0.05
700	1000	1.907×10^{-5}	0.13	1.778×10^{-5}	0.07	1.878×10^{-5}	0.07	1.841×10^{-5}	0.04
1000	1500	2.007×10^{-6}	0.19	1.874×10^{-6}	0.21	1.925×10^{-6}	0.19	1.975×10^{-6}	0.03

Table 10.3: Photon induced (PI) and real W and Z radiation corrections to the FEWZ3.1 predictions of Table 10.1 and Table 10.2. The additive PI correction is evaluated in pb/GeV using the MRST2004qed PDF. The multiplicative correction from W/Z radiation is evaluated using MADGRAPH 5. This table is taken from Ref. [107].

m_{ee}^{min} [GeV]	m_{ee}^{max} [GeV]	PI correction [pb/GeV]	W/Z radiation [%]
116	130	$2.46 \pm 0.91 \times 10^{-3}$	0.1 ±0.1
130	150	$1.42 \pm 0.53 \times 10^{-3}$	0.1 ±0.2
150	170	$9.07 \pm 3.46 \times 10^{-4}$	0.2 ±0.2
170	190	$6.03 \pm 2.33 \times 10^{-4}$	0.2 ±0.2
190	210	$4.12 \pm 1.61 \times 10^{-4}$	0.2 ±0.2
210	230	$2.90 \pm 1.14 \times 10^{-4}$	0.3 ±0.2
230	250	$2.09 \pm 0.83 \times 10^{-4}$	0.3 ±0.2
250	300	$1.25 \pm 0.51 \times 10^{-4}$	0.3 ±0.2
300	400	$4.85 \pm 2.02 \times 10^{-5}$	0.4 ±0.2
400	500	$1.60 \pm 0.69 \times 10^{-5}$	0.6 ±0.2
500	700	$4.62 \pm 2.08 \times 10^{-6}$	0.8 ±0.2
700	1000	$8.57 \pm 4.09 \times 10^{-7}$	1.1 ±0.2
1000	1500	$1.11 \pm 0.57 \times 10^{-7}$	2.2 ±0.2

masses and raise above 10% starting from $m_{ee} = 500$ GeV. The measured cross-section is compared to the theory predictions calculated with FEWZ 3.1. The dark green error band indicates the systematic uncertainties and the light green band the total uncertainties of the measurement. In the upper ratio plot the results using the five different

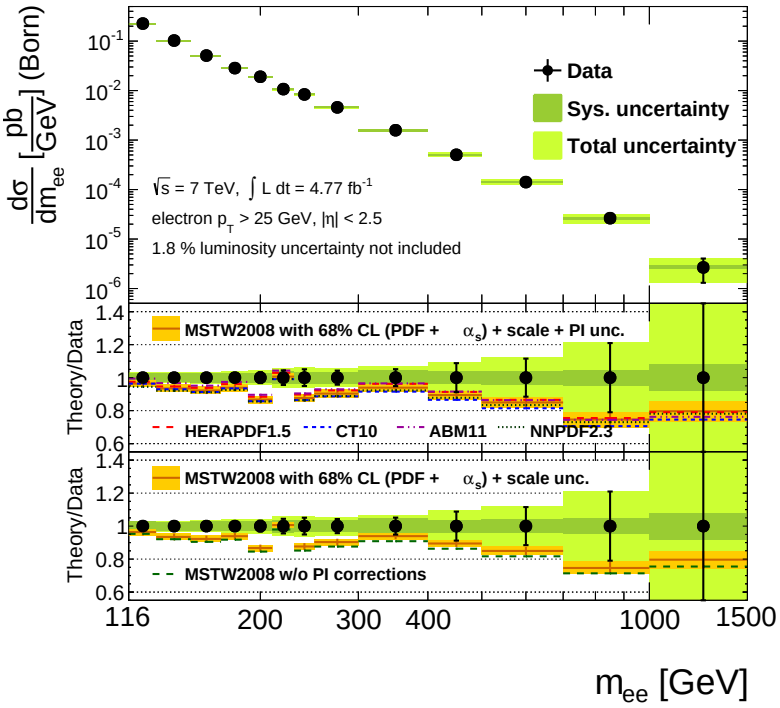

Figure 10.1: Cross-section at Born level in the region $p_T > 25\,GeV$ and $|\eta| < 2.5$ compared to the cross-section calculated with FEWZ 3.1. The upper ratio shows the result compared to the calculation using MSTW2008 PDF in brown with an orange error band for the theoretical uncertainties. The result using HERAPDF (red), CT10 (blue), ABM (magenta) and NNPDF (green) are shown without error. In the lower ratio the comparison is also done to the result using the MSTW2008 PDF without the photon induced corrections.

PDFs are compared to the measurement. For MSTW2008 an error band is shown to give a feeling about the size of the resulting theoretical uncertainties. The uncertainties on the calculations, using the other PDFs, are on the same order. As already seen in the distributions comparing data to the Monte Carlo samples the theoretical predictions underestimate the cross-section by about 5%. Within the total uncertainties of the measurement and the uncertainty of the prediction they are in agreement. The results using different PDFs are all in the same order and are all within the uncertainty of the MSTW2008 prediction.
In the lower ratio plot the influence of the photon induced process is shown. The measured cross section is compared to the default calculation using the MSTW2008 PDF and to the calculation using the same PDF but without the correction due to photon induced process. The effect is only on the order of the uncertainty of the theory prediction. Due to large uncertainty on the photon PDF the uncertainty on the photon induced process is on the oder of 50%. Therefore, this measurement is not sensitive to the PI effect. However, the with taking this process into account the discrepancy between measurement and theoretical prediction becomes smaller.
Figure 10.3 shows the cross-section at "dressed" level in the fiducial region with $p_T > 25\,GeV$ and $|\eta| < 2.5$.

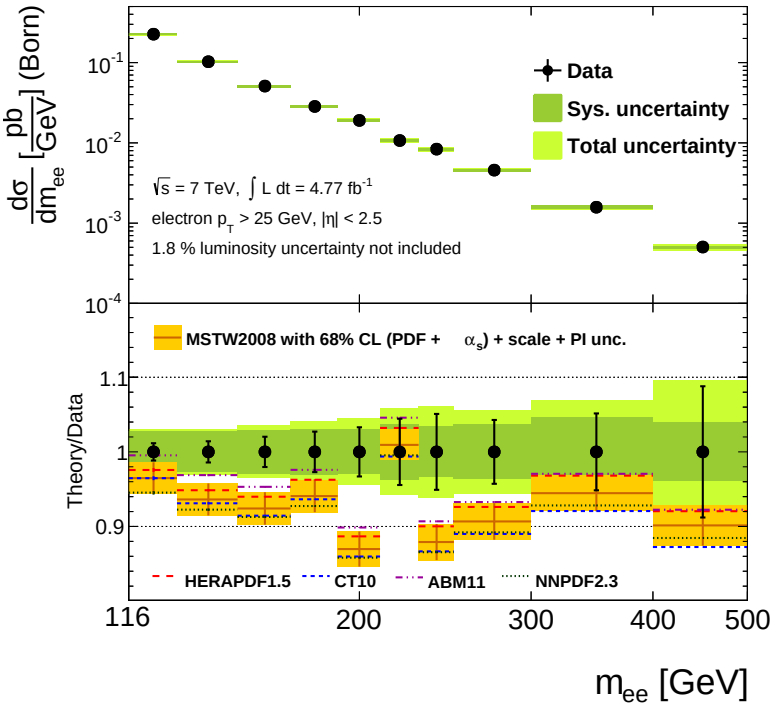

Figure 10.2: Cross-section at Born level in the region $p_T > 25\,GeV$ and $|\eta| < 2.5$ compared to the cross-section calculated with FEWZ 3.1. This is a close-up of the region of $116\,GeV < m_{ee} < 500\,GeV$.

In this plot the measured cross-section is compared to the predictions from the three different Monte Carlo generators which were used for this analysis. To have a better comparison to the generated spectra the k-factors as described in Section 5.3.2 were not applied to the Monte Carlo samples. Instead the distributions were scaled to the same inclusive cross-section as the measured data. The global scaling factor is given in the plot. As expected the scaling factor for the NLO generator (MC@NLO) is with 9% the smallest and the factors for the LO generators (PYTHIA and Sherpa) are significantly larger. Within the uncertainties the shape of all generators is in agreement with the measurement.

10.3 RESULTS COMPARED TO THE PUBLISHED MEASUREMENT

A comparison between the resulting cross-section published in the paper [42] and the result presented in this thesis was done. The ratio between the two measurements are shown in Figure 10.4.
The published measurement was corrected for the newest luminosity measurement and scaled by 1.7% to be comparable. In plot the ratio between old and new measurement is shown and the statistical (black) and systematical (green) uncertainties are the uncertainties of the older measurement. The two measurements are in a very good agreement, especially in the bins with high statistics. The deviations starting from 300 GeV can be explained by the smaller number of selected events and the differences in the used identification cuts and energy scales. The change in the set of identification

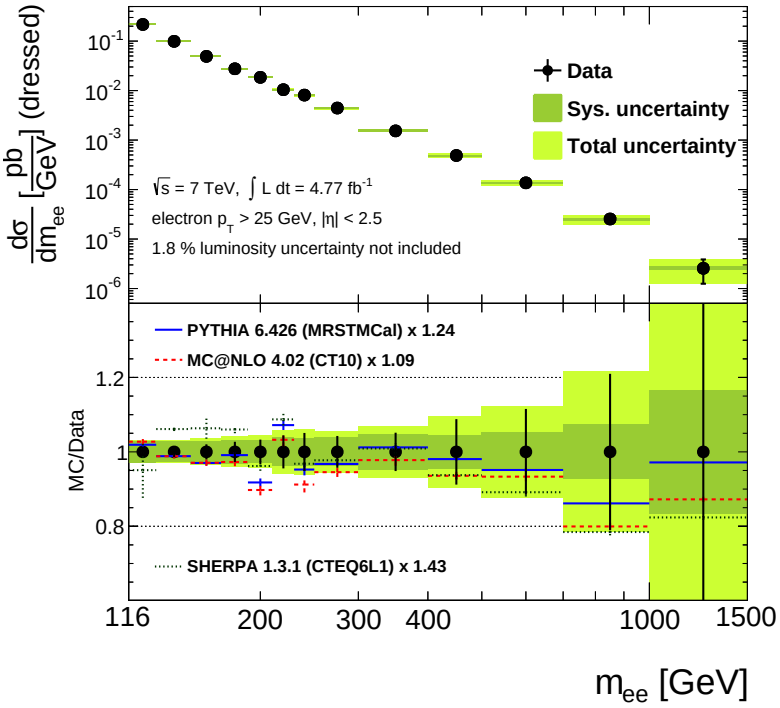

Figure 10.3: Cross-section at "dressed" level in the region $p_T > 25\,GeV$ and $|\eta| < 2.5$ compared to the cross-section extrapolated from the Monte Carlo generators Pythia (blue), MC@NLO (red), and SHERPA (green).

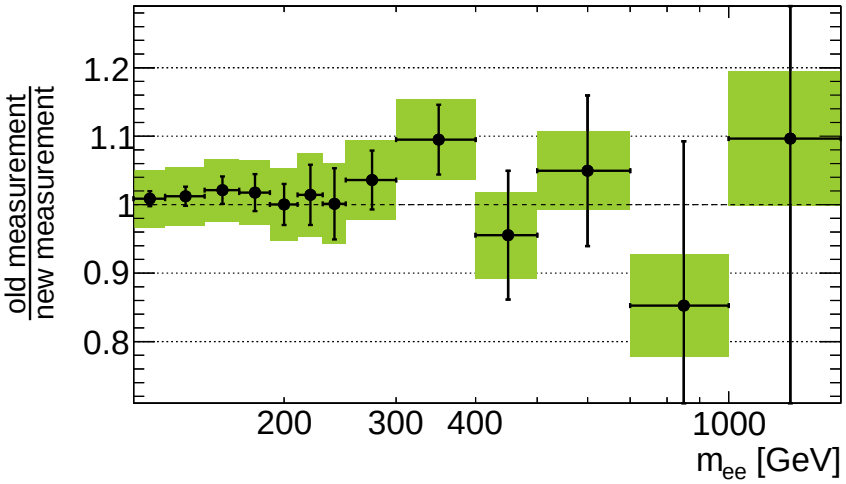

Figure 10.4: Comparison of the resulting cross-section as published (old measurement) and the result presented in this thesis (new measurement). The statistical uncertainty (black) and the systematic uncertainty (green) are the uncertainties from the old measurement.

cuts leads to a different signal event selection and the energy scale can lead to a different migration behavior for single events. In Figure 10.5 the systematic uncertainties of the two measurements are shown.

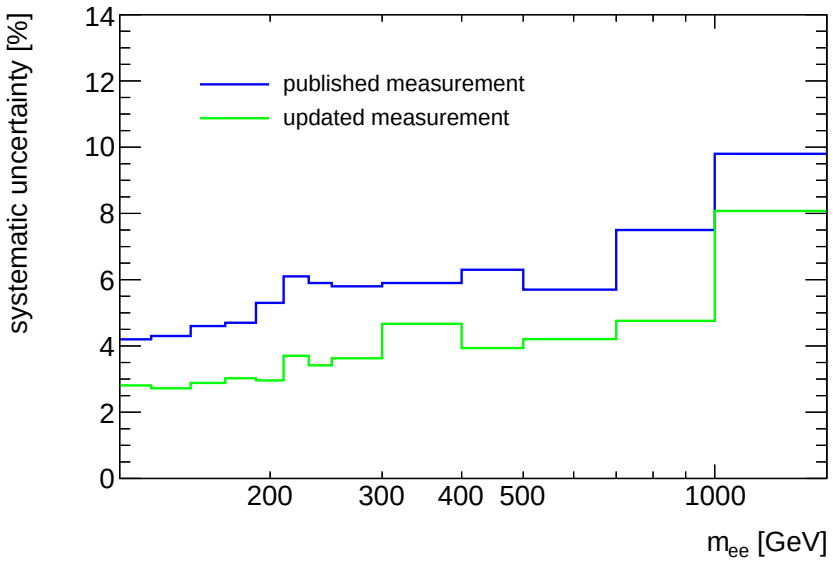

Figure 10.5: Comparison of the systematic uncertainties of the published result and the result presented in this thesis. The uncertainties of the published measurement are shown in blue and the uncertainties of the updated measurement are shown in green.

In blue the uncertainties of the measurement as it was published, and in green the updated uncertainties as presented in this thesis are shown. Due to the new identification cuts, the updated energy calibration and the reduced fake background the uncertainty was reduced by approximately 30%.

PDF-XChange Editor
Click to BUY NOW!
tracker-software.com

PDF-XChange Editor
Click to BUY NOW!
tracker-software.com

Part IV

SEARCH FOR NEW PHENOMENA WITH THREE OR MORE ELECTRONS/POSITRONS IN FINAL STATE

PDF-XChange Editor
Click to BUY NOW!
tracker-software.com

11

INTRODUCTION

The Standard Model of particle physics is a very accurate model which can describe mostly all of the phenomena observed in experiments. However, there are some examples which can not be explained by this theory such as neutrino oscillation and the amount of dark matter. Several attempts to extend the Standard Model to a theory which can also explain theses phenomenas leads to final states with multi-lepton signatures. Some of these theories are discussed in Chapter 2.4.2.

In this part of the thesis a model independent search for final states with three or more electrons is presented. The analysis was performed on the data collected in 2012 with the ATLAS detector at $\sqrt{s} = 8$ TeV.

For three or more electrons the largest contribution in the Standard Model with the correct number of real electrons in the final stage is coming from the diboson processes (WZ- and ZZ-production). This processes are well described by Monte Carlo generators and the theoretical cross section is known up to Next-to-Leading-Order (NLO) with only 5% uncertainty. The largest challenge is the description of the contribution which contains at least one jet, faking an electron. To describe these processes, the data-driven method used for the Drell-Yan cross-section measurement was develop further to be usable also for this analysis. This component could have had reduced by tighten the cuts for the signal selection, but aim of this analysis was it to cut away as few real electrons as possible.
By using also electrons reconstructed in the forward region[1] of the detector ($2.5 < |\eta| < 4.9$) the acceptance of the analysis is enlarged.

1 Which is not covered by the tracking system.

PDF-XChange Editor
Click to BUY NOW!
tracker-software.com

12

EVENT SELECTION

In this chapter the cuts to select multi-electron events and the different categories will be discussed. All cuts are identical for data and for used Monte Carlo samples. For this analysis the complete data collected in 2012 in the so-called "EGamma" stream were used. All events which had fired at least one electron or photon trigger are collected in this stream. Only proton-proton collisions with $\sqrt{s} = 8\,\text{TeV}$ were taken into account.

12.1 DATASET

For this analysis the complete dataset of proton-proton collisions collected with the ATLAS detector in 2012 at a center of mass energy of $\sqrt{s} = 8\,\text{TeV}$ was used. In Figure 12.1 the cumulative luminosity delivered to and recorded by ATLAS versus time is shown.

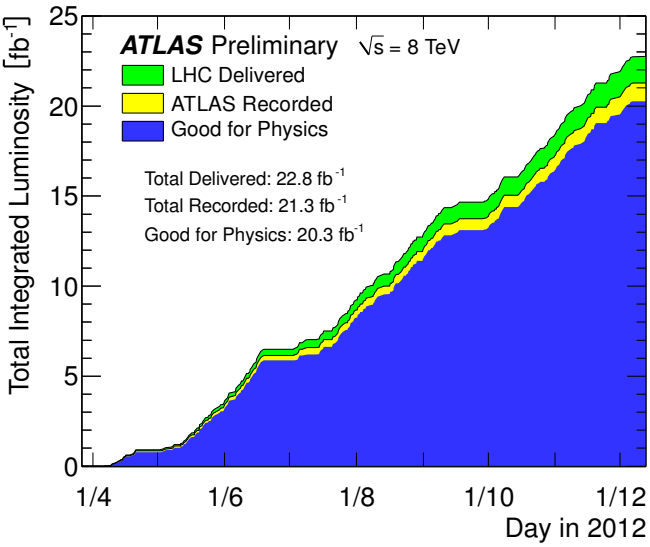

Figure 12.1: Cumulative luminosity versus time delivered to (green), recorded by ATLAS (yellow), and after applying all quality cuts (blue) during stable beams and for pp collisions at sqrts = 8 TeV in 2012.

After applying all quality cuts the amount of collected and used data is corresponding to an integrated luminosity of 20.3 fb^{-1}. For the event selection all data collected in the so-called "EGamma"[1] stream were used. In this stream all events which had fired at least one electron or photon trigger are collected. For the data-driven background estimation, presented in the next chapter, the so-called "JetTauEtMiss" collection was

1 The "E" denotes electron and the "Gamma" denotes photon.

used additionally. As indicated by the name of the stream it contains all events were a jet, tau or missing transverse energy trigger had fired.

12.2 TRIGGERS

For the multi electron analysis on the 2012 data the "EF_2e12Tvh_loose1" was used together with the "EF_2e12Tvh_loose1_2StarB"[2] to correct for inefficiency at low p_T. These are di-electron (2e) triggers with a p_T threshold of 12 GeV and loose electron ID requirements. To optimize the L1 trigger an η dependent energy threshold (v) and a hadronic isolation (h) was used at this level. For the L2 trigger an additional track isolation (T) was applied. The "1" at the end of loose indicates that a at this point new set of ID requirements was used, which is now the default as described in the next section.
The "EF_jX_a4tchad"[3] triggers, which are again used for the data-driven background method are the same as for 2011 were only the name and the p_T thresholds have changed.

12.3 EVENT BASED SELECTION

First a set of event based cuts was applied, which will be described in the following.

Good Run List
To remove events which were recorded during bad beam or detector conditions a so called "good run list" (GRL) was applied. For this analysis a GRL which requires good conditions in the inner detector and the central and forward calorimeters was used. Explicit the GRL named "data12_8TeV.periodAllYear_DetStatus-v61-pro14-02_DQDefects-00-01-00_PHYS_StandardGRL_All_Good_EgammaForward.xml" were used.

Vertex cut
To remove cosmic events and to be sure that all reconstructed events were originated in the beam pipe a vertex cut was applied. All events in the selection had to have at least one primary vertex with three or more associated tracks.

Trigger
Goal of this analysis was it to select events with three or more electrons with a p_T-requirement as small as possible. Therefore the EF_2e12vhT_loose1 trigger together with EF_2e12Tvh_loose1_L2StarB (see above for more details), to correct for inefficiencies in later runs, was used. Both triggers are unprescaled, that means no event with the required signature was lost due to dead time. The choice of the trigger leads to the offline requirement of two central electrons[4] with a $p_T > 15$ GeV and at least loose ID criteria for all categories of the analysis.

2 This trigger is only available for some runs and is used in combination with the default trigger. The "L2StarB" indicates that some corrections on the L2 trigger was applied to correct for the inefficiencies.
3 X = 15, 25, 35, 45, 55, 80, 110, 145, 180, 220, 280, 360, 460.
4 Only the central region of the detector is covered by the trigger-system.

PDF-XChange Editor Click to BUY NOW! tracker-software.com

12.4 OBJECT BASED SELECTION

Cuts on the reconstructed electron objects were applied to increase the probability of real electrons. Two different set of cuts are applied depending on the detector region where the electron objects were reconstructed. For the further procedure objects reconstructed in $|\eta_{elec}| < 2.5$ are called "central" and all objects with a larger absolute value of η are called "forward".

12.4.1 *Central Objects*

Author and η Cut
A cut on the pseudorapidity of the electron objects $|\eta_{elec}| < 2.47$ was applied. In addition, the transition region between barrel and end-cap ($1.37 < |\eta_{elec}| < 1.52$) was excluded[5]. With help of the author information only electrons, reconstructed by the standard algorithm[6] were taken into account. For more information about the reconstruction algorithm see Section 4.1.

Object Quality
During the run period some of the optical transceivers (OTx) on the front end board of the Liquid Argon (LAr) calorimeter were broken. Electron objects which are detected close by such a channel were removed from the selection. Also events with LAr noise bursts were removed.

Electron Identification
To distinguish between reconstructed real electrons and fake objects the Medium ID was used. Only objects which passed the requirements of this ID was taken further into account. The Medium ID has a efficiency of 90% and is powerful to reject fake objects. For more details of the electron IDs see Section 4.2.

Cut on p_T
All objects from the central region are required to have a transverse momentum (p_T) larger than 15 GeV to fulfill the requirements of the used trigger.

12.4.2 *Forward Objects*

Author and η Cut
A cut on the pseudorapidity of the electron objects $2.5 < |\eta_{elec}| < 4.9$ was applied. In addition, the transition region between the inner wheel of the end-cap and the forward calorimeter (FCAL) ($3.16 < |\eta_{elec}| < 3.35$) was excluded because of the very poor resolution. With help of the author information only electrons, reconstructed by the forward algorithm[7] were taken into account. For more information about the reconstruction algorithm see Section 4.1.

5 The resolution in the transition region between barrel and end-cap is very poor.
6 The variable "el_author" had to be 1 or 3.
7 The variable "el_author" had to be 8.

Object Quality
During the run period some of the optical transceivers (OTx) on the front end board of the Liquid Argon (LAr) calorimeter were broken. Electron objects which are detected close by such a channel were removed from the selection. Also events with LAr noise bursts were removed.

Electron Identification
A forward object had to pass the forward medium ID requirements which are described in detail at Section 4.2. The efficiency of the forward medium ID is around 80% and the background suppression is quit strong.

Cut on p_T
The $p_T$of the objects had to be larger than 20 GeV. Due to the missing tracking system in the forward region the IDs are only valid for objects with p_T> 20 GeV. Therefore the $p_T$cut is slightly higher then for central objects.

12.5 FINAL SELECTION AND DIFFERENT CATEGORIES

If an event pass all the selection cuts as described above and there are at least two central objects which fulfill the object selection[8] it is taken into account for the final selection. In this step also the different categories are defined.
In some cases the electron reconstruction algorithm reconstruct two energy depositions in the calorimeter which are very close ($\Delta R < 0.1$) and which were then matched to the same track. The shape and the energy deposition of these two clusters are always close but not the same. This happens in less then 0.2% of the selected events. Therefore it seems to be a small problem with the reconstruction algorithm. To deal with this only the object with the higher p_T were used if in an event two objects were using the same tracking informations. The other object was rejected.
The events are sorted by the number of central and forward objects in the event passing the cuts. All categories are defined as minimum requirements and all possible unique combinations are considered. An example is given in the following. If in an event are four selected central objects this event will have four different entries in the "three central" category and one entry in the "four central" category. If in an event are three selected central objects and one forward object this event will have one entry in the "three central" and one entry in the "three central one forward" category.
For each category there are two sub-categories. One were the present of at least one real Z-boson is required and one were only events without a real Z-boson were taken into account. To consider if there is a real Z-boson or not the invariant mass of all possible pairs was calculated. A real Z-boson was identified if the invariant mass of at least one pair was in mass window of 10 GeV around the real Z-boson mass. If both electrons were reconstructed they also have to had opposite charge. For the veto the mass window was enlarged to 20 GeV around the Z-boson mass. The different categories together with the number of selected events are shown in Table 12.1

8 This is necessary to fulfill the trigger requirements.

Table 12.1: Number of selected events, shown for the different categories.

minimal requirements	events	events with Z	events w/o Z
at least three central electrons	6700	3997	1587
at least two central and one forward electron	8467	6201	1302
at least four central electrons	51	48	2
at least three central and one forward electron	23	21	1
at least two central and two forward electrons	19	13	2
more than four central electrons	0	0	0
more than three central electrons and at least one forward electron	0	0	0
more than two central electrons and at least two forward electron	1	1	0
more than one central electron and at least three forward electron	0	0	0

PDF-XChange Editor
Click to BUY NOW!
tracker-software.com

13

STANDARD MODEL PREDICTION

The selected events from data are compared to predictions for all known Standard Model processes which could contribute to the different categories. These predictions can be separated into two components.
The first includes all processes with at least the exact numbers of real electrons in the final state for the different categories. The contribution of these processes was estimated using Monte-Carlo simulations and the procedure is described in the first part of this chapter.
The second component includes all contributions where at least on object faking an electron signature. This contribution was estimated with a data-driven method, which will be described in detail in the second part of this chapter.

13.1 REAL ELECTRON CONTRIBUTION

To estimate the contribution from Standard Model processes with the correct number of real electrons in the final state Monte Carlo samples were used. The following processes were taken into account.

- Diboson production processes (WW, WZ, ZZ)
- $t\bar{t}$ production in association with vector bosons ($t\bar{t}W$, $t\bar{t}Z$, $t\bar{t}WW$)
- Triple vector boson production processes (WWW^*, ZZZ^*, ZWW^*)
- Higgs decay via ZZ (Higgs production over Vector-boson fusion, gluon-gluon fusion and production in association with an W-boson or $t\bar{t}$-production.)
- DY $\rightarrow$ ee
- DY $\rightarrow \tau\tau$
- $t\bar{t}$ production (with a lepton filter applied)
- single Top production with an associated W-boson

For each Monte Carlo sample a cut on generator level was applied to make sure that only events with at least the correct number of real electrons passed the selection for the different categories. Therefore the number of electrons on generator level after the simulation of the hard process were counted. Afterwards the same signal selection as for data was applied to the Monte Carlo samples. The Monte Carlos samples were

weighted to the luminosity and scale factors for reconstruction, identification and trigger were used as described in Section 5.3. All Monte Carlo samples, together with the number of generated events and the corresponding cross-sections can be found at Table 13.1. Additional Monte Carlo samples, only used for the category with at least two real electrons in the final state are listed in Appendix B.

Table 13.1: Table of the simulated Monte Carlo samples for the 2012 multi-electron search. Simulations for all processes contributing to the categories defined for the search are listed. Beside the ATLAS internal run number in column two, the used generator (column three), the cross-sections (times branching ratios) times filter efficiencies (column four), the number of generated events N_{event} (column five), the corresponding luminosity $\mathcal{L}_{MC}$ is given in column six.

Signature (filter)	MC runnumber	generator	$\sigma B \times \epsilon_f$ [pb] [%]	N_{event} [k]	$\mathcal{L}_{MC}$ [fb^{-1}]
WZ production	105987	Herwig	6.56	1000	152.4
ZZ production	105986	Herwig	1.56	245	157.1
WWW* production	167006		5.10×10^{-3}	50	9,803
ZZZ* production	167008		3.32×10^{-4}	50	150,602
ZWW* production	167007		1.55×10^{-3}	50	32,258
$t\bar{t}W$ production	119353	Herwig	1.04×10^{-1}	400	3,846
$t\bar{t}Z$ production	119355	Herwig	6.77×10^{-2}	400	5,908
$t\bar{t}WW$ production	119583	Herwig	9.19×10^{-4}	10	10,881
VBF Higgs production	160205		4.27×10^{-4}	200	468,384
gg fusion Higgs production	160155		3.48×10^{-3}	200	57,471
Higgs W production	160255		1.47×10^{-4}	100	680,272
Higgs $t\bar{t}$ production	167562		2.37×10^{-5}	100	4,219,409

Following the procedure described above the last four processes in the listing as well as the WW-diboson production contributes only to the "two central electrons" category which was used as a control region. All other processes contributes to the "three central" and the "two central & one forward" categories. For all categories with four electrons the ZZ-Diboson, $t\bar{t}Z$, $t\bar{t}WW$, ZZZ*, ZWW* and the Higgs production were considered. For the categories with five or more electrons only the events from the ZZZ* process and the Higgs production in association with a W-boson or $t\bar{t}$-pair were considered.

13.2 FAKE CONTRIBUTION

In addition there is a large contribution coming from events were one or more electron signatures are faked by jets. For the category with three central electrons for example these are mainly events where a Z-boson decays into two electrons and in addition a jet was misidentified as an electron.
To estimate these contributions a data-driven matrix-method was used. The idea of the method is the same as already described in Chapter 8 for the high-mass Drell-Yan

cross-section. Before this thesis the method was only used for analysis with one or two electron objects. Therefore the method had to be extended to get a prediction for events with three, four or even five objects.
For two objects there are four real quantities and four measurable quantities which are connected via a matrix with dimension four. For three objects the number of quantities and the dimension of the matrix is enlarged to eight. For four objects there are already sixteen different combinations and for five objects the number is twenty three.
To invert the matrices the program Mathematica [111] was used. With this program it was not possible to invert the full matrix if the dimension becomes larger then eight. To have a consistent procedure the method where the real electron efficiency was set to one ($r = 1$) was used as default. The missing correction was done with help of Monte Carlo samples. The full matrix method ($r \neq 1$) was used to estimate the uncertainty on the method for three selected objects. For the categories with four, respectively five, objects also the full matrix was used, but the real electron efficiencies was set to one for the two, respectively three, objects with highest p_T. This is the minimum simplification of the matrix in order to be still able to invert the matrix. As shown in Figure 13.5 the efficiency for high p_T is close to one. Therefore the effect should be negligible with respect to the other uncertainties.

13.2.1 *Fake Rate Estimation*

The fake rate $f = \frac{N^{fake}_{Tight}}{N^{fake}_{Loose}}$ was estimated using three different methods. The "Loose" and "Tight" level was defined for central and forward objects separately. The "Tight" level is always the same as the signal selection, while the "Loose" level is defined as:

- "central objects": loose electron ID and p_T> 15 GeV
- "forward objects": forward loose electron ID and p_T> 20 GeV

Goal of all three methods is to have a jet-sample as clean as possible to estimate the probability of a jet faking the electron signature. In the following the different methods will be described in detail.

Single Object Method with Jet Trigger
For this method the "JetTauEtmiss" stream and a single jet trigger was used. Due to the high rate of jets at LHC there are several single jet triggers with different p_T threshold. To cover the whole range 13 different triggers were used. The single jet triggers with low p_T threshold were all prescaled[1] but this is not important for the method because only the ratio and not the total number of jets is important. In the case that more than one trigger had fired in one event the trigger with the lowest $p_T$threshold was used. This was done to avoid double counting.
To make sure that the objects reconstructed as electrons are correlated to a jet a matching ($\Delta R < 0.1$) was performed. The matched jet object had to have a good quality. This was done by applying a "medium" jet cleaning. For more details see Section 8.2.2
To remove possible real electrons further cleaning cuts were applied. Events with a

1 Prescaled means that not all event which fulfill the requirements of the trigger are recorded. If the final rate is too high, only a fraction of all possible events are recorded.

MET > 25 GeV were removed from the selection. This cut is efficient to remove electrons from W-boson decays. To remove electrons from the Drell-Yan process events where two objects in the electron container had at least passing the loose (or forward loose) electron ID and build an object with an invariant mass close to the Z-boson mass ($71\,\text{GeV} < m_{ee} < 111\,\text{GeV}$) were rejected. Also events with two electron objects with at least medium (or forward medium) electron ID were removed.
All objects surviving the above procedure was then tested with the "Loose" and "Tight" definition. For each trigger the fake rates was calculated separately and afterwards the weighted average was calculated.

Tag and Probe Method on Jet Stream
For this method the same data and triggers as for the previous method were used. Also the matching between electron and jet objects was done the same way.
For more details about the idea of the tag and probe method see Section 8.2.2.
As tag object any central object which failed the loose electron ID and had a p_T larger than 15 GeV was used. All other electrons in the events were tested as probe electrons if they fulfill either the "Loose" or the "Tight" requirements. This was done using all possible tag and probe combinations but each electron object was only taken once as probe object.
Also here some additional cleaning cuts were used to suppress real electrons. Again events with a MET > 25 GeV where removed to reject W-boson events. To suppress electrons coming from the Drell-Yan process objects where the invariant mass of the tag and the probe objects is close to the Z-pole ($|91\,\text{GeV} - m_{ee}| < 20\,\text{GeV}$) were removed. Also if both objects was in the central region and they had opposite charge they was not taken into account.

Tag and Probe Method on Egamma Stream
This method is nearly the same as the one before, but the same data and trigger as for the event selection was used. The more signal like trigger is the largest challenge for this method. The trigger, requiring two central objects with at least loose electron ID is the reason why this method could be only used to estimated the fake rate of central objects.
The choose of the tag object is also biased by the trigger. Therefore the tag object had to passed the loose electron ID but fail the medium electron ID or the isolation. The p_T of the object had to be larger then 15 GeV.
The cleaning cuts are the same as for the jet stream, but the matching to a jet object is missing. After passing all cuts the probe objects was tested with the "Loose" and "Tight" definition.
Since this method has still a non negligible amount of real electrons in the selection the same procedure was repeated with the real electron Monte Carlo samples to get a feeling of the number of real electron passing this procedure. The result from the Monte Carlo samples was subtracted from the "Loose" and "Tight" distributions before the fake rate f was calculated. In Figure 13.1 the p_T distribution of the probe objects are shown.
The data point shows the raw "Loose" and "Tight" distribution from this method. They are plotted together with the corrections extracted from the real electron Monte Carlo samples which were subtracted afterwards. In the further process if it is

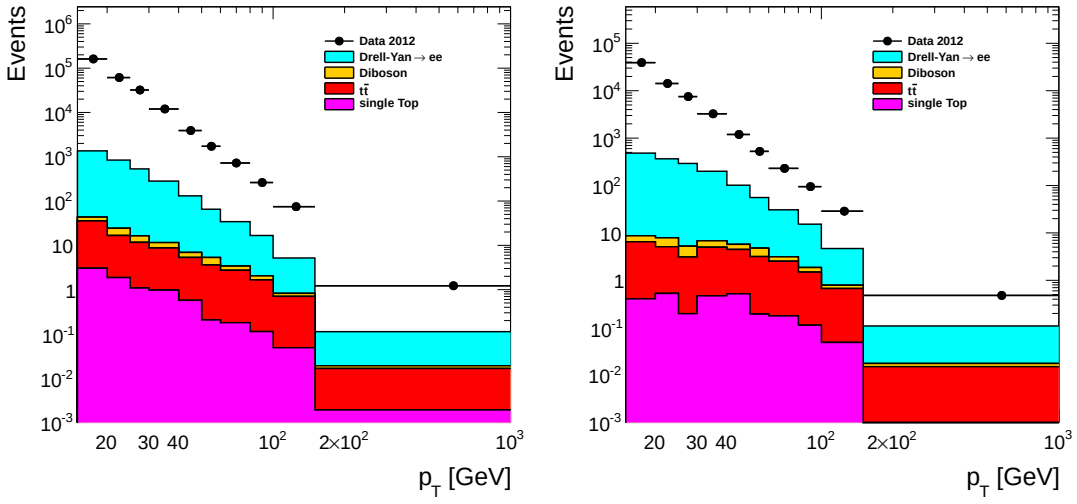

(a) The p_T distribution of "Loose" selection.

(b) The p_T distribution of "Tight" selection.

Figure 13.1: The distributions of the tag and probe method on the Egamma stream to estimate the fake rate together with the correction from the real electron Monte Carlo samples which was subtracted afterwards.

quoted that this method was used for forward objects the fake rate from the tag and probe method on jet stream was used.

13.2.2 *Comparison of the Fake Rate Methods*

Figure 13.2 shows the estimated fake rates for the central region using the three different methods.
The different methods show nearly the same behavior. For the central region a trend to larger fake rates is visible for higher p_T objects. In most bins the single jet method provides the smallest fake rates, where the tag and probe method on the EGamma stream gives the largest. For the latter the last bin was enlarged due to problems with the statistics. The fake rate value in the central region is in average around 0.3. In the region between $0.6 < |\eta| < 2.37$ the behavior is nearly the same, where for the region $|\eta| < 0.6$ the rate is more flat and for $2.37 < |\eta| < 2.47$ the the fake rate is much higher.
In Figure 13.3 the fake rates estimated for the forward region are shown.
The distributions for the forward region shows a different behavior. In the region of the Endcap inner wheel ($2.5 < |\eta| < 3.16$) the fake rate drops down for higher p_T objects and goes up again starting from 150 GeV on. The fake rate estimated in the FCAL region ($3.16 < |\eta| < 4.9$) is nearly flat at around 0.6. In the bins, where no point is shown, no object was found for the calculation. Also no fakeable object was found in this phase space.
As default method the single jet method was chosen. This method has the largest statistics and provides the cleanest jet sample.

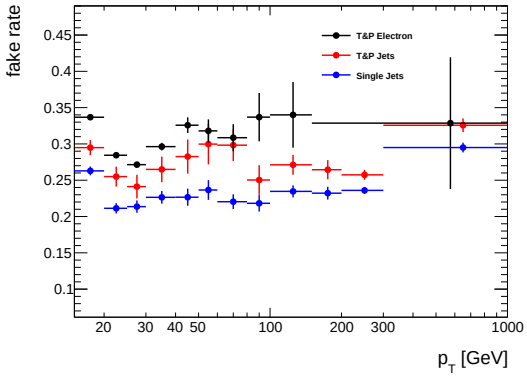

(a) $|\eta| < 0.6$

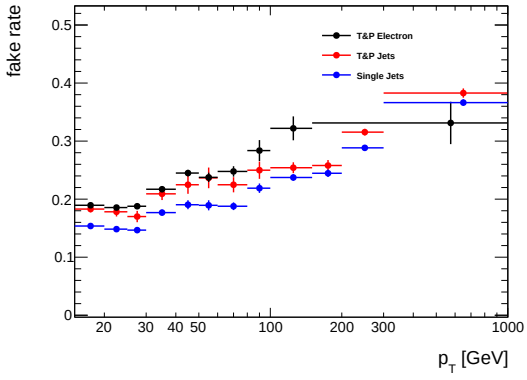

(b) $0.6 < |\eta| < 1.37$

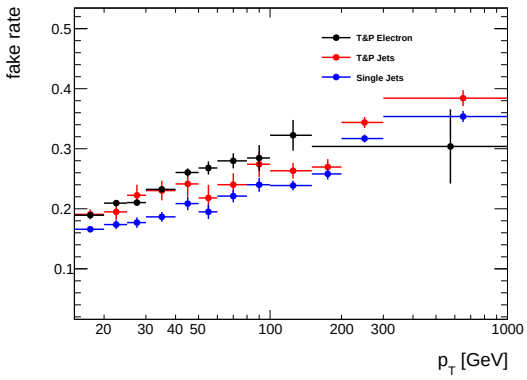

(c) $1.52 < |\eta| < 2.01$

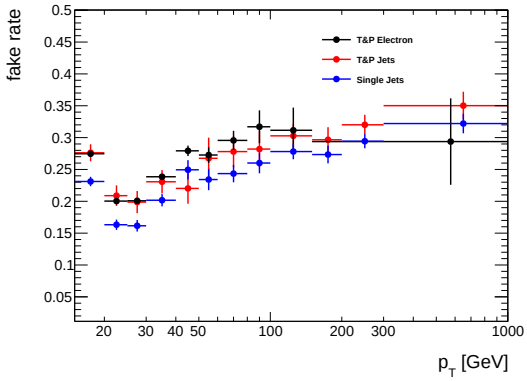

(d) $2.01 < |\eta| < 2.37$

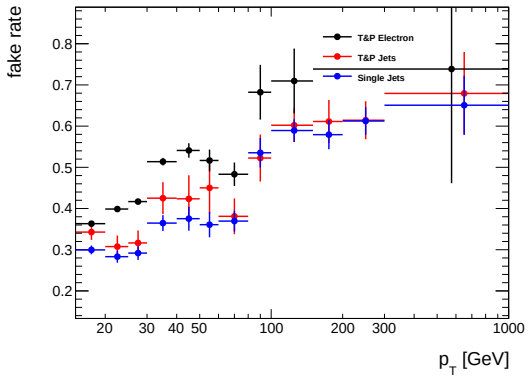

(e) $2.37 < |\eta| < 2.47$

Figure 13.2: The p_T dependent fake rates for the central detector regions ($|\eta| < 2.47$). In each plot the result of the three different methods are shown.

Fake Rate for Different Compositions

The composition of the jets[2] in the signal sample and in the "JetTauEtmiss" sample, which was used for the default method to estimate the fake rates might be different. The effect was tested calculating the fake rates separately for b-jets and all other jets.

2 The number of heavy jets, coming from bottom- or charm-quarks, with respect to the number of light jets (up-,down- and strange-quarks).

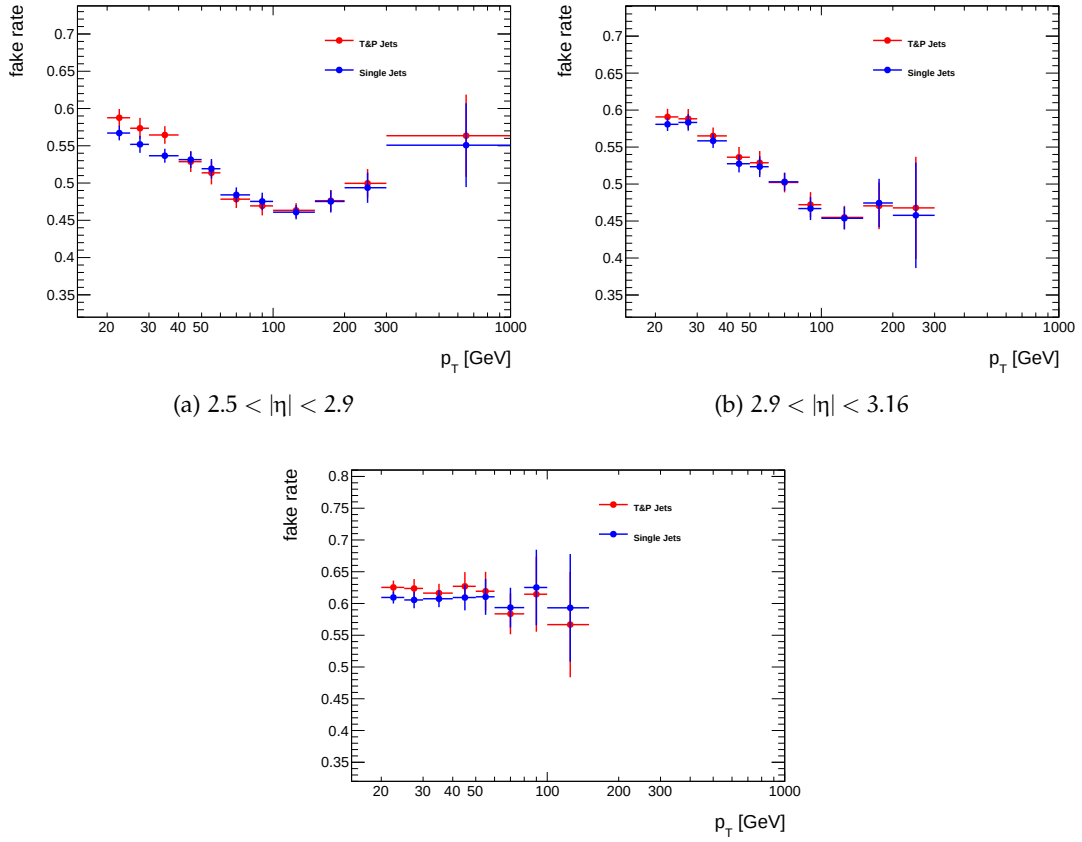

(a) $2.5 < |\eta| < 2.9$

(b) $2.9 < |\eta| < 3.16$

(c) $3.16 < |\eta| < 4.9$

Figure 13.3: The p_T dependent fake rates for the forward detector regions ($2.5 < |\eta| < 4.9$). In each plot the result of the two different methods are shown.

To distinguish between b-jets and other jets the parameter "MV1" was used. This parameter is calculated using a multi-variant method and gives the probability that the jet is coming from the decay of a bottom quark. The cut, used for this analysis gives a b-tagging efficiency of 70% and the remaining light jet contribution is only at 0.7%. More details about the algorithm used and the efficiency and light jet rejection can be found at Ref. [112]. In Figure 13.4 the fake rate distribution for the complete central region is shown.
There is clearly an effect for low p_T jets visible. For an b-jet with a transverse momentum of 15 GeV the fake rate is three times larger and becoming the same for p_T larger then 100 GeV. This effect was considered by applying the correct fake rates. Even if the effect seems to be large, it is not. The contribution of b-jets to the fakeable objects is smaller then 2%. Therefore an effect of the different jet composition is not visible in the final fake contribution.

13.2.3 *Real Electron Efficiency*

The real electron efficiency was calculated using the $pp \to Z/\gamma \to ee$ Monte Carlos samples. A truth matching ($\Delta R < 0.1$) was applied to make sure that only real electrons coming from the hard process were taken into account. Since the goal is it to

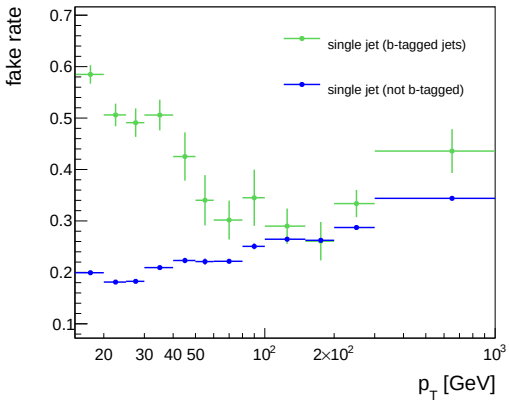

Figure 13.4: The comparison between the fake rate of b-tagged and not b-tagged jets.

calculate a single real electron efficiency no MET cut nor trigger requirements was applied. All electron objects surviving the above procedure were tested with the "Loose" and "Tight" definition. Afterwards the real electron efficiency was calculated using $r = \frac{N^{elec}_{Tight}}{N^{elec}_{Loose}}$. The resulting real electron efficiencies are shown in Figure 13.5 for the central region and in Figure 13.6.
In the central region the efficiency increase with higher $p_T$of the electrons. In the forward region the efficiency is mostly constant. In nearly all bins the efficiency is above 90%.

13.2.4 *Fakeable Object Selection*

The fakeable objects were selected the same way as described in Section 8.2.4, but for each selection type (central or forward) there is a "Loose not Tight" selection defined. The objects have to fulfill the "Loose" definition as defined in Section 13.2.1 but fail the "Tight" definition (which is identical with the signal selection).
The selected objects ("Loose" or "Loose not Tight") were ordered by p_T. Then all possible unique combinations were saved for each category and afterwards the fakeable objects were weighted with the corresponding factors calculated from the matrix-method. Since this method is a little bit complicated a example will be given in the following.
From now on the shortcut "Lc" will be used for a central object passing the "Loose not Tight" selection, "Tc" for a central object passing the "Tight" selection and "Lf" and "Tf" for a forward object.
Assumption: An event with the following objects was found: Tc(1), Lc(2), Tc(3), Lf(4).
These objects would now contribute to the following categories:

- "two central": Tc(1)Lc(2), Tc(1)Tc(3), Lc(2)Tc(3)
- "three central": Tc(1)Lc(2)Tc(3)
- "two central, one forward": Tc(1)Lc(2)Lf(4), Tc(1)Tc(3)Lf(4), Lc(2)Tc(3)Lf(4)
- "three central, one forward": Tc(1)Lc(2)Tc(3)Lf(4)

At the end the event contributes three different fakeable objects for the "two central" and "two central, one forward" categories and one fakeable object for the "three central"

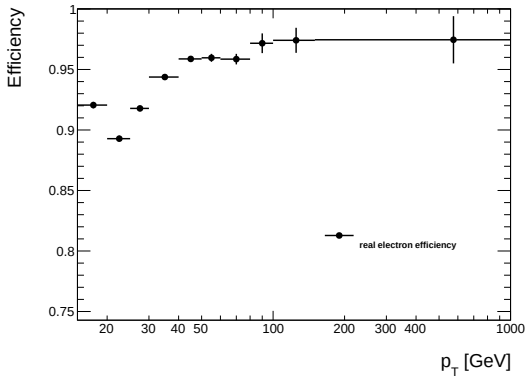

(a) $|\eta| < 0.6$

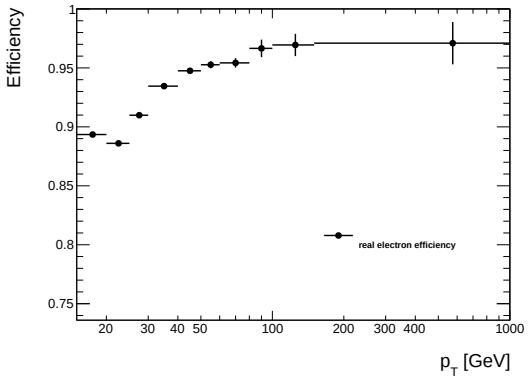

(b) $0.6 < |\eta| < 1.37$

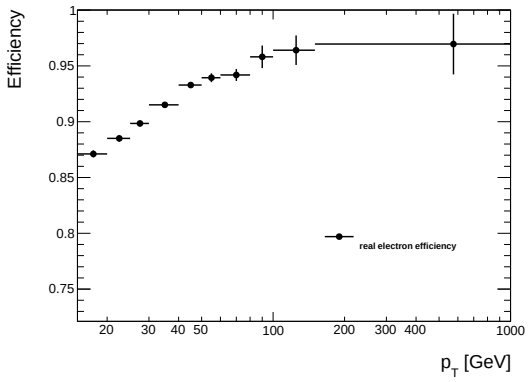

(c) $1.52 < |\eta| < 2.01$

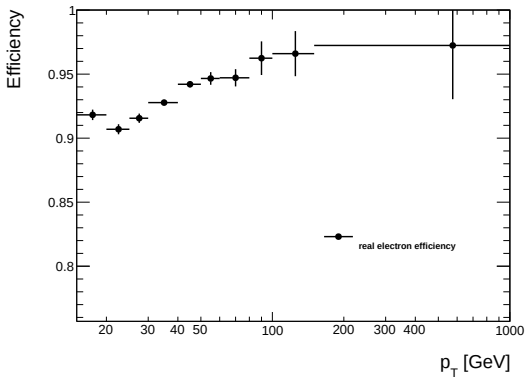

(d) $2.01 < |\eta| < 2.37$

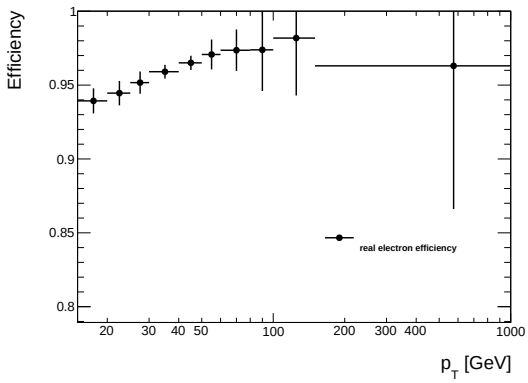

(e) $2.37 < |\eta| < 2.47$

Figure 13.5: The p_T dependent real electron efficiencies for the central detector regions.

and "three central, one forward" categories. Every time weighted with a different factor as calculated from the matrix-method.

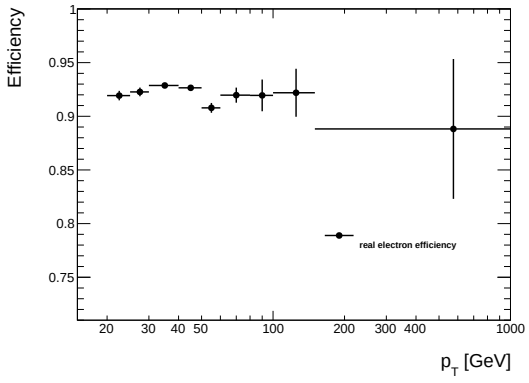

(a) $2.5 < |\eta| < 2.9$

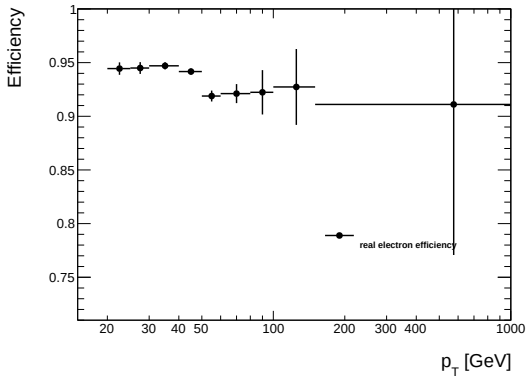

(b) $2.9 < |\eta| < 3.16$

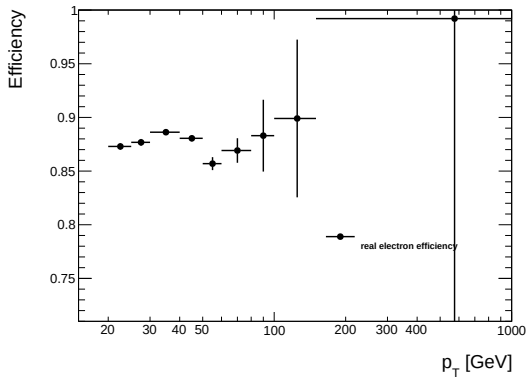

(c) $3.16 < |\eta| < 4.9$

Figure 13.6: The p_T dependent real electron efficiencies for the forward detector regions.

13.2.5 *Uncertainty on the Standard Model Prediction*

Real Electron Contributions

For the real electron contribution, predicted with Monte Carlo samples the theoretical uncertainty of the cross-section as well as the statistic limitation[3] of the samples were used as uncertainty. The theoretical uncertainty on the diboson production cross-sections is 5% [93]. This was applied as a flat uncertainty. Since this is the dominant contribution for all categories[4] all other cross-section uncertainties are negligible.

Fake Contributions

To estimate the uncertainty on the data-driven method the three fake rates, extracted from the different methods were used. Together with the choice of the general method (full matrix or $r = 1$) this gives six different results for the fake contribution. Since the fake contributions are very dependent on the category and also on the distribution itself this was done separately for each single distribution by comparing the five vari-

3 The statistic of the Monte Carlo samples is in general very good. Only in some bins this has an effect.

4 Beside the "two central" category, but this was only used for a cross check. In this channel there might be some important sources of uncertainties missing.

ations with the result from the default method. For a conservative estimation always the maximum deviation for each bin was taken as uncertainty. Figure 13.7 shows two typical examples. Other examples can be found in Figure C.1 in Appendix C.

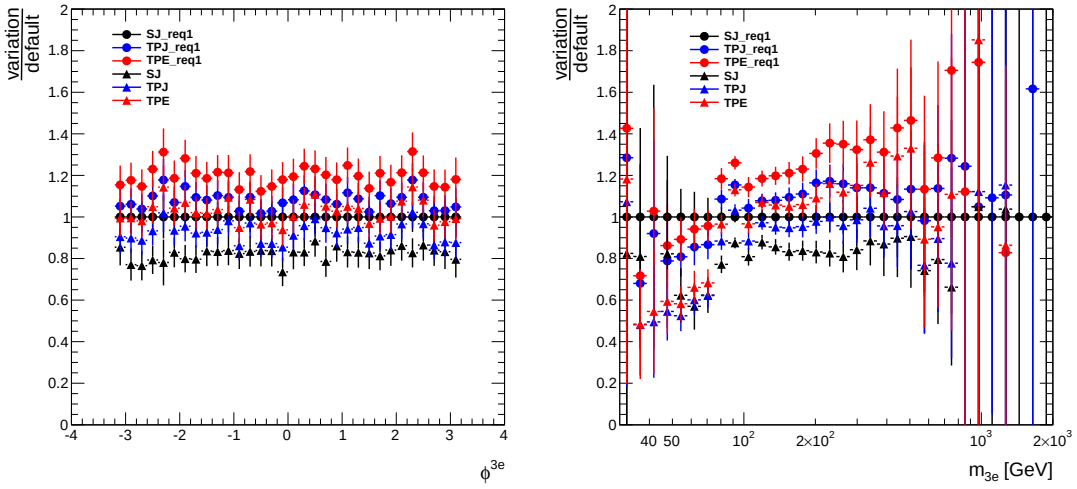

(a) The Φ spectrum of the three electron system. (b) The invariant mass spectrum of the three electron system.

Figure 13.7: Ratio of the variations with respect to the default method for two distributions from the "three central" category.

On the left side the five different variations are shown for the Φ distribution of the three electron system. The variations shows a maximum deviation of around 20% for each bin. The method where r was set to be equal one with the fake factors, estimated from the tag and probe method on the Egamma stream shows the largest upwards variation, where the largest downwards fluctuation is coming from the full-matrix method using the fake factors from the single jet method. This distribution was chosen, because the statistic is nearly the same for each bin. For other distributions where this is also true the behavior of the uncertainty is the same. On the right side the behavior for the invariant mass distribution of the three electron system is shown. In the region were the statistic uncertainty is not dominant the average of the variation is also in the order of 20%. In the region above 80 GeV it seems that the default method is over estimating the fake contribution a little bit. Above 80 GeV it shows the same behavior as before.
The uncertainty on the Monte Carlo prediction together with the systematic uncertainty of the data-driven method and the statistic uncertainty of the default data-driven method were added up quadratically to got the final uncertainty on the Standard Model prediction. This was done for each distribution and for each bin separately and is shown in the following plots as a hatched area.

PDF-XChange Editor
Click to BUY NOW!
tracker-software.com

14

VALIDATION AND CROSS CHECKS

For the 2011 data and for a selection with two electrons it was shown in the high-mass Drell-Yan analysis (see Part iii) that the Standard Model is well described by the combination of Monte Carlo samples and the data-driven method. The Monte Carlo samples were normalized with next-to-leading order (NLO) and next-to-next-to-leading order (NNLO) cross-sections to the corresponding luminosity of the data.
To validate the data-driven method for the 2012 data the inclusive "two central electron" category was used. The invariant mass of the two electron system is shown in Figure 14.1a starting from 10 GeV. In Figure 14.1b the p_T distribution of the single electrons starting at 15 GeV is shown.

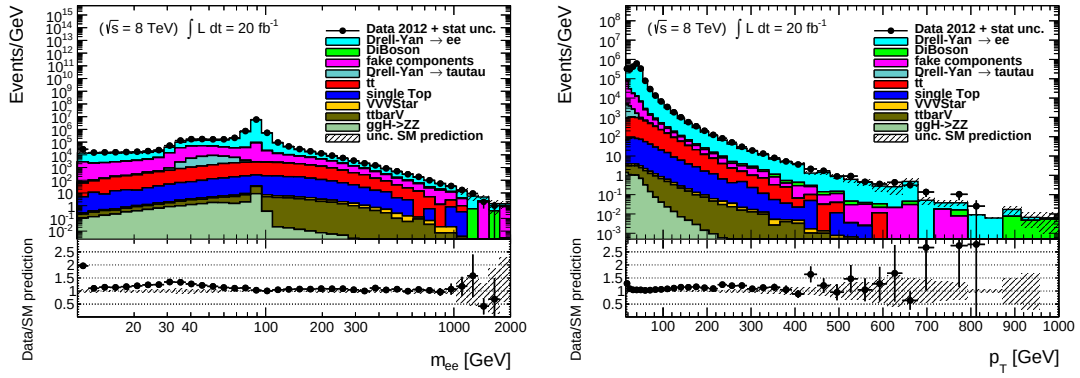

(a) Invariant mass of the two central electrons

(b) p_T of the single electrons

Figure 14.1: Control distributions of the "two central" category. The data from 2012 (black points) is shown together with the Monte Carlo samples and data-driven prediction.

The invariant mass distribution shows a really good agreement between data and the Standard Model expectation for the region of 60 GeV and above. The discrepancy up to 40% at around 30 GeV and the outlier at 10 GeV can be explained by the Drell-Yan Monte Carlo samples used for this region. For this region leading order (LO) SHERPA Monte Carlo samples were used without correction factors for higher order[1]. At 10 GeV an explicit sample for the Y decay is missing.
The spectrum of the single electron p_T starting at 15 GeV shows the expected behavior. The mismatch of the first bin is due to the LO Monte Carlo sample mentioned above. As mentioned before, no uncertainty on the Drell-Yan cross-section was applied. Apart from that the distribution shows a good agreement getting a little bit worse for high

1 For these Monte Carlo samples no k-factors were available.

p_T . This is unfortunately a known effect for all ATLAS analysis.
Since the contribution of the data-driven method is significant smaller for the two electron selection as for the categories with three electrons it is important to check also some control distributions for these categories. Figure 14.2 shows the single electron distributions of η and p_T for the "three central" category.

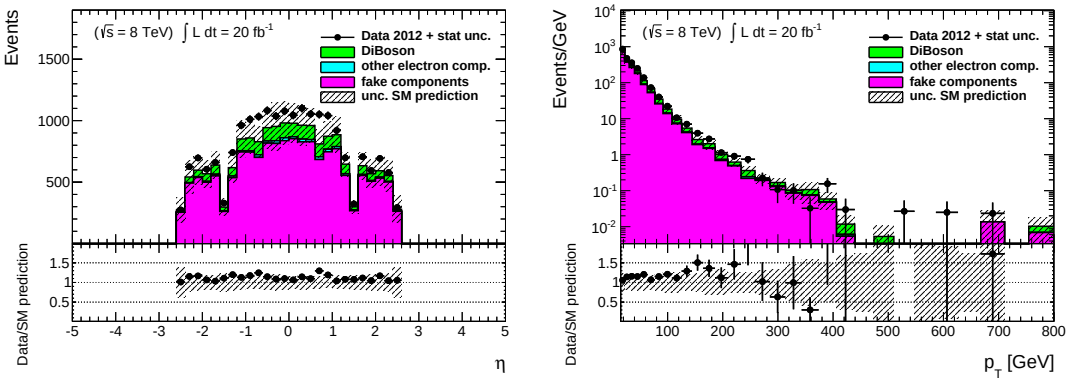

(a) The η distribution of the single electrons. (b) The p_T distribution of the single electrons.

Figure 14.2: Control distributions of the "three central" category. The data from 2012 (black points) is shown together with the Monte Carlo and data-driven prediction.

Within the uncertainty the agreement of the η spectrum is good. The ratio is nearly flat. An underestimation of around 10% of the Standard Model prediction is visible but is covered by the uncertainties. The p_T distribution shows a good agreement for p_T smaller 120 GeV. For higher values the agreement gets slightly worse, but only for one data point the difference is above one sigma.
To get a feeling about the behavior of the electrons reconstructed in the forward region two control functions of the "two central, one forward" category are shown in Figure 14.3.

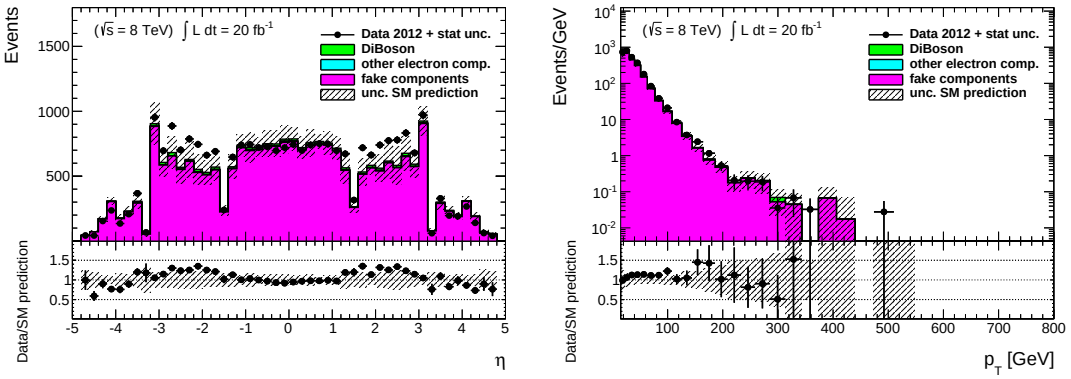

(a) The η distribution of the single electrons. (b) The p_T distribution of the single electrons.

Figure 14.3: Control distributions of the "two central, one forward" category. The data from 2012 (black points) is shown together with the Monte Carlo and data-driven prediction.

For the η distribution some fluctuations in the order of 30% are visible but everything is covered by the uncertainties. In the central region the agreement is better than in the forward region. The region covered by the FCAL inner wheel shows the largest deviation. The p_T spectrum of the single electrons is well described by the Standard Model prediction.

PDF-XChange Editor
Click to BUY NOW!
tracker-software.com

15

RESULTS

15.1 COMPARISION BETWEEN DATA AND STANDARD MODEL

In this chapter the selected events for the different categories are compared with the Standard Model expectation, estimated using the methods described before. For the "three central", "two central, one forward", four central", three central, one forward" and "two central, two forward" four final distributions are shown. For the "three central" also the separation of events with and without a real Z-boson are shown. A comparison of the total number of events to the Standard Model prediction is shown in Table 15.1. This includes also the categories for which no plots are shown. For this categories the statistic is such low, that plots does not make any sense.

Table 15.1: Selected events in data for the different categories compared to the Standard Model prediction. The predictions and uncertainties are separated for the diboson, the real electron without diboson and the fake components.

category	Data events	SM pred. (diboson)	unc.	SM pred. (other real)	unc.	SM pred. (fake cont.)	unc.	SM pred. (total)	unc.
"three central"	6700	664.9	33.2	105.2	51.5	5187.3	1330.2	5957.4	1331.2
"three central (Z)"	3997	617.3	30.9	32.7	36.8	2949.8	690.1	3599.8	691.1
"three central (w/o Z)"	1587	24.5	1.2	54.0	30.1	1360.7	469.2	1439.2	470.1
"two central, one forward"	8467	185.0	9.2	35.0	100.7	7607.9	1151.5	7827.8	1155.9
"two central, one forward (Z)"	6201	172.7	8.6	7.7	86.6	5609.6	588.7	5790.0	595.0
"two central, one forward (w/o Z)"	1302	7.2	0.4	21.7	41.4	1268.4	396.3	1297.3	398.5
"four central"	51	41.2	2.1	0.7	3.8	4.4	4.9	46.3	6.2
"four central (Z)"	48	40.8	2.0	0.5	3.2	3.4	3.3	44.8	4.6
"four central (w/o Z)"	2	0.2	<0.1	0.1	0.6	1.0	0.6	1.2	0.8
"three central, one forward"	23	9.0	0.5	0.1	5.2	19.3	5.6	28.4	7.7
"three central, one forward (Z)"	21	8.8	0.4	0.1	5.0	16.9	5.9	25.7	7.7
"three central, one forward (w/o Z)"	1	0.2	<0.1	<0.1	1.5	2.8	1.0	3.0	1.8
"two central, two forward"	19	3.8	0.2	<0.1	6.0	16.5	13.5	20.3	14.7
"two central, two forward (Z)"	13	3.7	0.2	<0.1	5.3	11.3	10.8	15.0	12.0
"two central, two forward (w/o Z)"	2	0.0	0.0	<0.1	1.4	1.8	1.5	1.8	2.0
"five central"	0	0.0	0.0	<0.1	<0.1	<0.1	<0.1	<0.1	<0.1
"four central, one forward"	0	0.0	0.0	0.0	0.0	0.0	0.0	0.0	0.0
"three central, two forward"	1	0.0	0.0	0.0	0.0	0.0	0.0	0.0	0.0
"two central, three forward"	0	0.0	0.0	0.0	0.0	0.0	0.0	0.0	0.0

To make the plots easier to read all real electron components, except the diboson contributions are summarized as one. The distributions of the transverse momentum are

shown with a logarithm y-axis. The binning in x-axis are equidistant in square root of the bin width. The spectra of the invariant mass are binned in an equidistant logarithm binning on the x-axis. All plots shown here are normalized to the bin width, except the rapidity spectra which shows the number of events.

Figure 15.1 shows the distributions for the "three central" category.

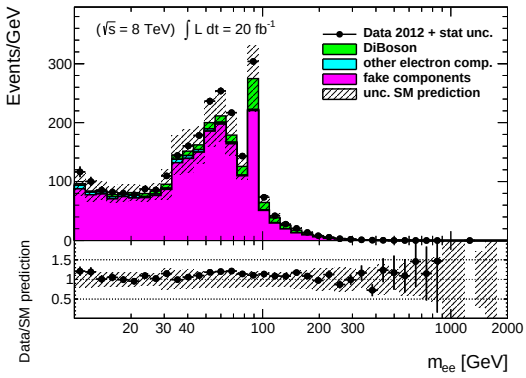

(a) Invariant mass of all possible electron pairs.

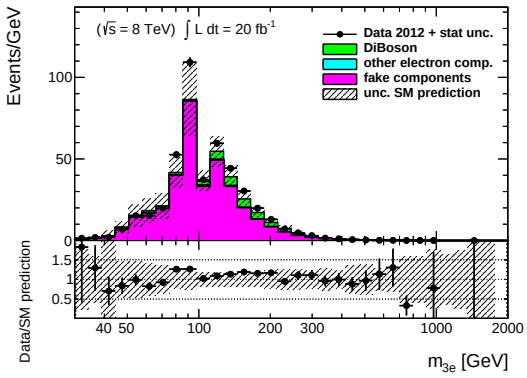

(b) Invariant mass of the three electron system.

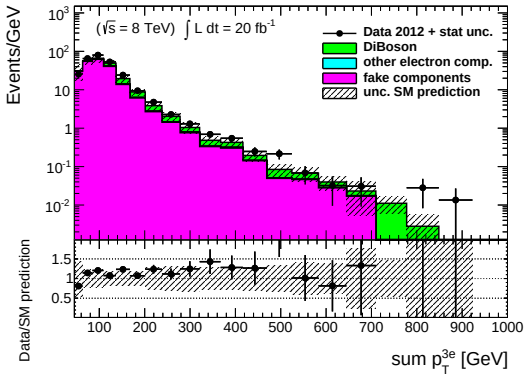

(c) The sum of the p_T of the three electrons.

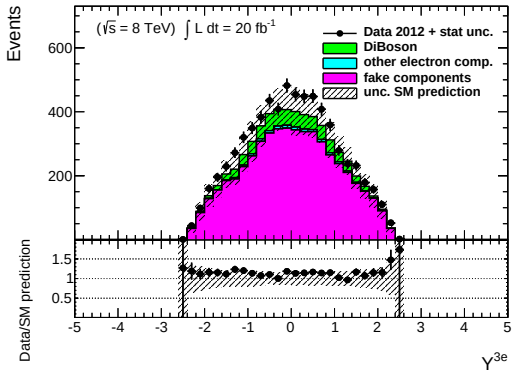

(d) The rapidity of the three electron system.

Figure 15.1: Distributions of the "three central" category. The black dots shows the result from 2012 data, which is compared to the sum of the diboson (green), other electron contributions (blue) and the fake components (magenta).

On the upper left plot the invariant mass of all possible pairs is shown. The agreement over the whole mass range is good. The small fluctuations are covered by the uncertainties. On the upper left plot the invariant mass of the three electron system is is presented. Most of the diboson events have a mass of 120 GeV and above. The peak at around 90 GeV is coming from Z-boson events with an additional jet. The two real electrons loose energy due to Bremsstrahlung and therefore the invariant mass is shifted to values below 90 GeV. Together with a low energy jet the invariant mass of these events can be in the region of the Z-peak. This is modeled nicely by the data-driven method and gives a good agreement within the uncertainties. On the lower left side the sum of the three electrons p_T is plotted. The only outlier is at around 500 GeV, but this is only a one sigma effect. The spectrum of the rapidity of the three electron system (lower right plot) shows a nice agreement. As expected most of the objects were

produced in rest. The restrictions on the electron η leads to the typical form. The over all shift of around 10% is covered by the uncertainties.
The results of the "three central" category with at least on real Z-boson in the event is presented in Figure 15.2.

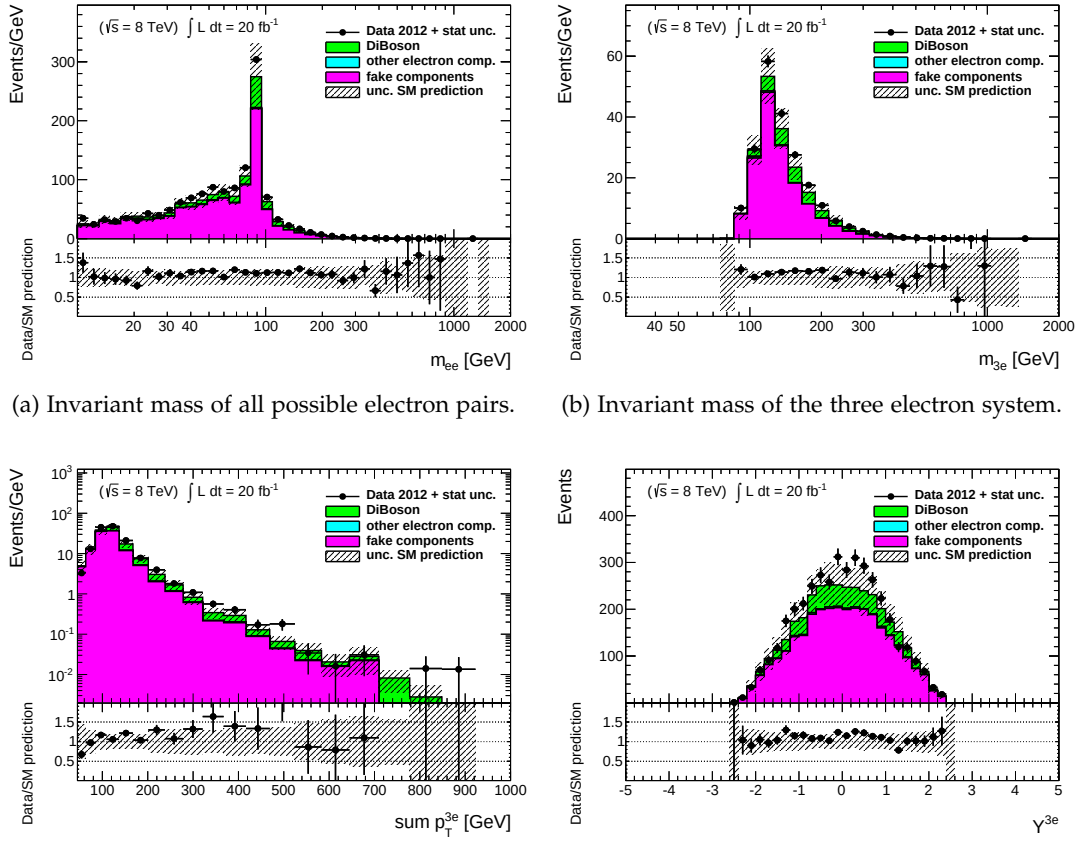

(a) Invariant mass of all possible electron pairs.

(b) Invariant mass of the three electron system.

(c) The sum of the p_T of the three electrons.

(d) The rapidity of the three electron system.

Figure 15.2: Distributions of the "three central" category. Only events which contains at least one real Z-boson are shown. The black dots shows the result from 2012 data, which is compared to the sum of the diboson (green), other electron contributions (blue) and the fake components (magenta).

This is a subset of the "three central" category. In the spectrum of the invariant mass of all possible electron pairs the Z-peak is clearly visible. The agreement within the uncertainties is very good and there are no large fluctuations. Since there is the requirement that the event contains at least one real Z-boson with invariant mass between 81 GeV and 101 GeV the invariant mass of the three electron system is always above the Z-peak. As before the agreement is good with in the uncertainties. The agreement of data and expectation of the sum of the electron p_T is also good. The outlier at 500 GeV is the same as seen before. The rapidity distribution also shows a good agreement.
The distributions for the "three central" category with a veto on real Z-bosons is shown in Figure 15.3. In this category there is nearly no contribution from processes with the correct number of real electrons. Most of the objects have low p_T . In the invariant mass spectrum of the electron pair the region which was cut away is clearly visible. Most of the electron pairs are at low m_{ee}. The agreement over the whole range is within the un-

certainties. For high invariant masses some fluctuations are visible. The invariant mass of the tree electron system is also mainly in the region above 100 GeV. The ratio shows a smooth behavior with some fluctuations. The falling spectrum of the sum of p_T of the three objects also has a good agreement. In the rapidity spectrum of the three electron system the agreement is good. There are two bins at around -1 which are slightly miss modeled by the data-driven method.

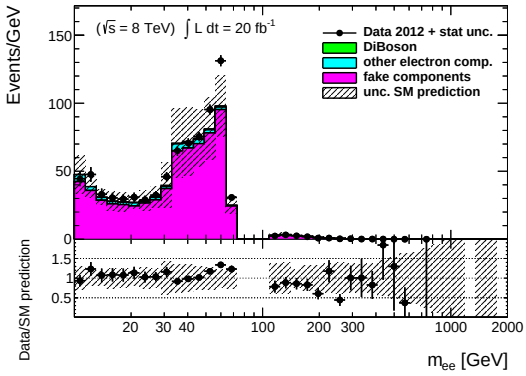

(a) Invariant mass of all possible electron pairs.

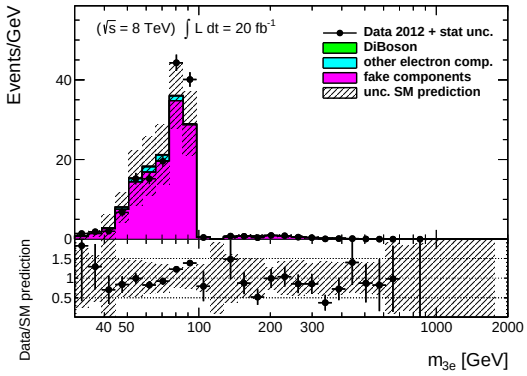

(b) Invariant mass of the three electron system.

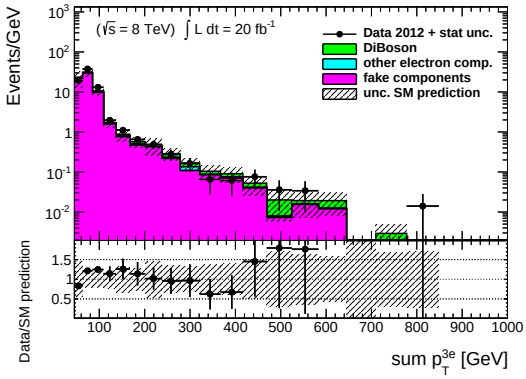

(c) The sum of the p_T of the three electrons.

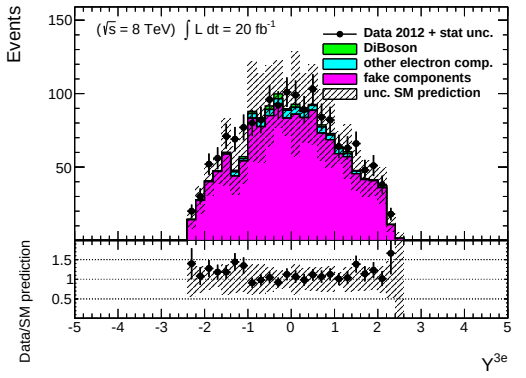

(d) The rapidity of the three electron system.

Figure 15.3: Distributions of the "three central" category. Only events without any real Z-boson are shown . The black dots shows the result from 2012 data, which is compared to the sum of the diboson (green), other electron contribution (blue) and the fake components (magenta).

Figure 15.4 shows the distributions for the "two central, one forward" category. For this category the invariant mass distribution of the electron pairs shows a good agreement in the high mass region. For the low mass region some fluctuations and small bump between 50 GeV and 80 GeV is visible. These discrepancy is coming from events without a real Z-boson. Since the forward region is not covered by the tracking system it is very hard to model the fake contribution in a correct way, especial for the low p_T region. The invariant mass distribution of the three electron system is the logical consequence of the miss behavior. The low mass pairs are combined with a third object and the effect increase in the two bins around 90 GeV. The spectrum of the sum of the electron p_T gives a good agreement and also the rapidity distribution is in good

agreement within the uncertainties. Only some bins in some bins in the forward region the fake contribution is underestimated. Due to the one electron object reconstructed in the forward region the rapidity is as expected shifted to higher values.

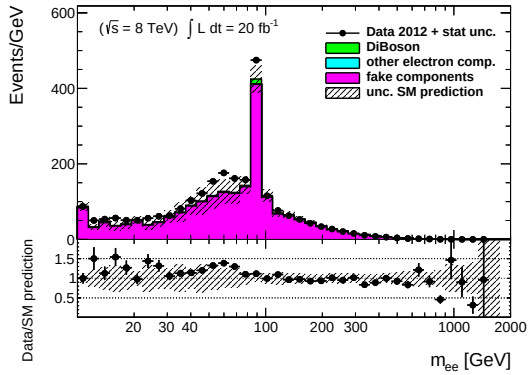

(a) Invariant mass of all possible electron pairs.

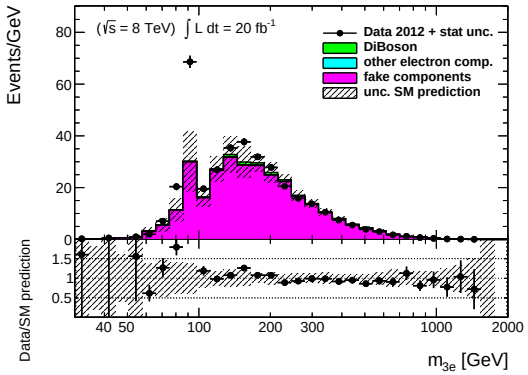

(b) Invariant mass of the three electron system.

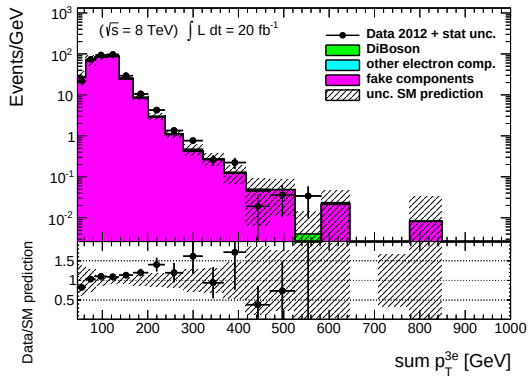

(c) The sum of the p_T of the three electrons.

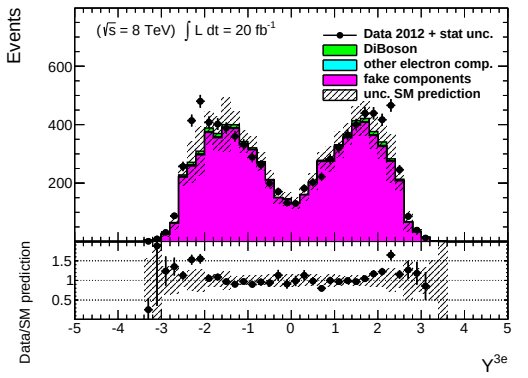

(d) The rapidity of the three electron system.

Figure 15.4: Distributions of the two central, one forward" category. The black dots shows the result from 2012 data, which is compared to the sum of the diboson (green), other electron contribution (blue) and the fake components (magenta).

At the distributions for the "four central" category, shown in Figure 15.5 a different composition of the Standard Model components is visible. These channel is dominated by the ZZ-diboson production. The peak around 91 GeV is nicely modeled by the diboson Monte Carlo sample. For the low mass region, where virtual Z-bosons and combinatorics playing a role there are some small deviations, which are covered by the uncertainties. The spectrum of the invariant mass of the whole system shows a similar behavior. Also the spectrum of the summed electron p_T and the rapidity distribution are well described by the prediction.
By including forward electrons in the selection its gets harder to get a good estimation. Figure 15.7 shows four plots of the category, where three central and one forward electron was selected. With in the statisitcaland also systematic uncertainties there is a agreement in the distribution of the invariant mass of the electron pairs. For the invariant mass of the four electron system an slightly overestimation of the Standard Model processes is visible, but within the uncertainties the agreement is given. This

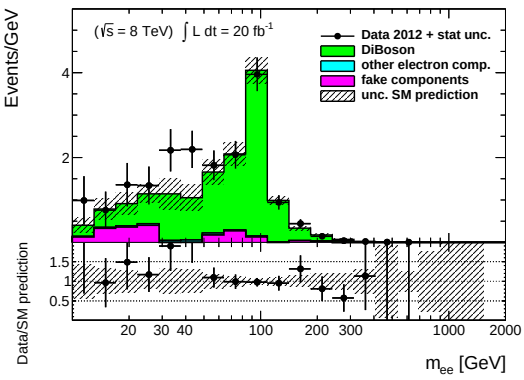

(a) Invariant mass of all possible electron pairs.

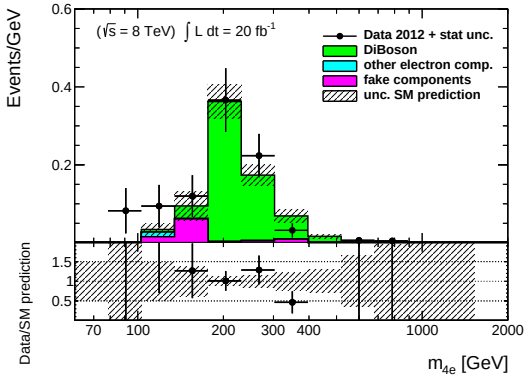

(b) Invariant mass of the four electron system.

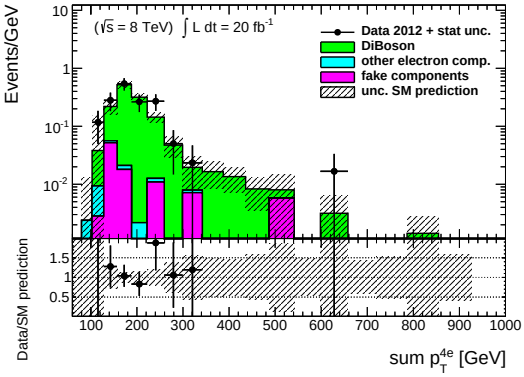

(c) The sum of the p_T of the four electrons.

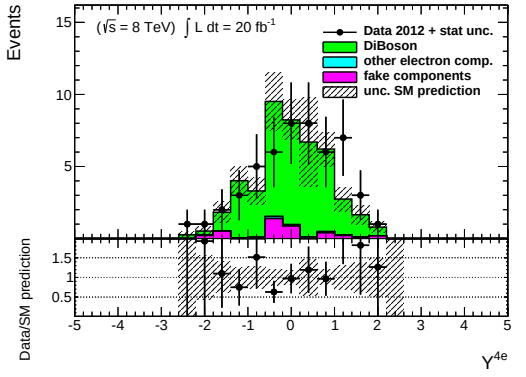

(d) The rapidity of the four electron system.

Figure 15.5: Distributions of the "four central" category. The black dots shows the result from 2012 data, which is compared to the sum of the diboson (green), other electron contribution (blue) and the fake components (magenta).

is also true for the distributions of the sum p_T and the rapidity of the four electron system.
Figure 15.7 shows the distributions for the "two central, two forward" category. For this category data and also the data-driven method is running out of statistics. Within the large uncertainties, which are for the Standard Model prediction in the order of 100%, the agreement is non the less good. Also the overall agreement as shown in Table 15.1 is good for this category.

15.2 RESULT COMPARED TO MODELS BEYOND STANDARD MODEL

The result was compared to Monte Carlo predictions of two theoretical models beyond the Standard Model to get a feeling about the sensitivity of this analysis.
The first Monte Carlo sample simulates the leptonic decay of a doubly charged Higgs, as for example predicted by type II Seesaw models as introduced in Section 2.4.2. The Monte Carlo sample was produced under the assumption of a democratic scenario where the branching ratio to each pair of lepton flavors is the same. The cross-section times branching ratio times filter efficiency is 3.7×10^{-3} pb for the production of a doubly charged Higgs with a mass of 350 GeV and 5.9×10^{-4} pb for a mass of 500 GeV.

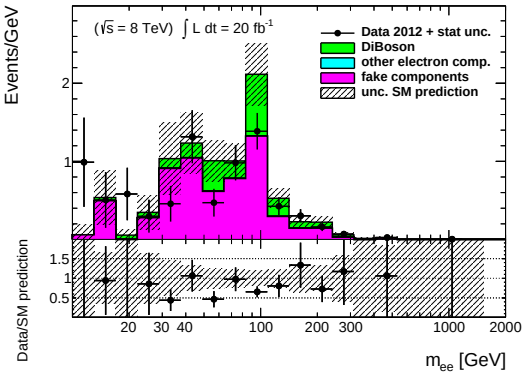

(a) Invariant mass of all possible electron pairs.

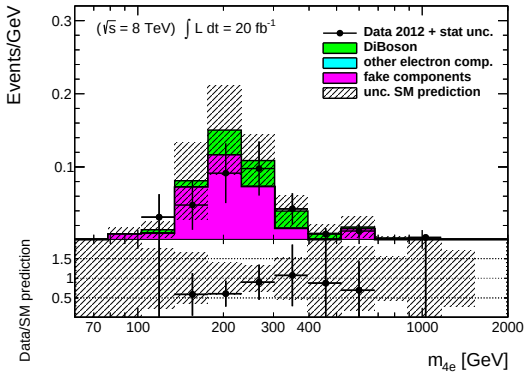

(b) Invariant mass of the four electron system.

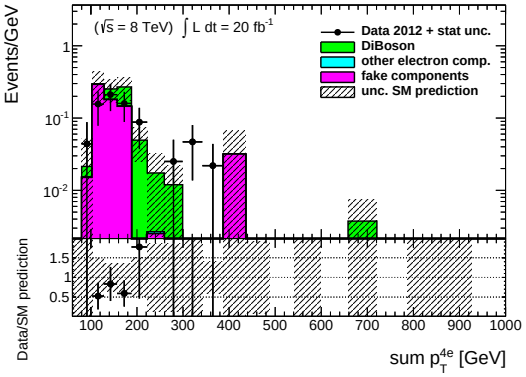

(c) The sum of the p_T of the four electrons.

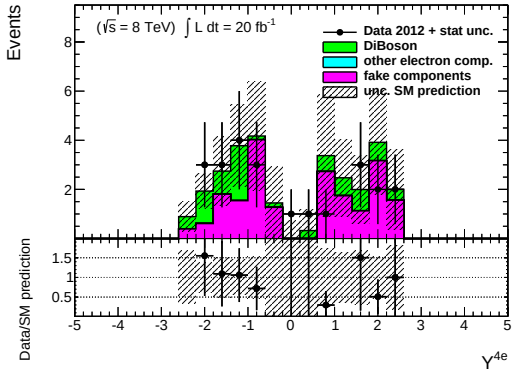

(d) The rapidity of the four electron system.

Figure 15.6: Distributions of the "three central, one forward" category. The black dots shows the result from 2012 data, which is compared to the sum of the diboson (green), other electron contribution (blue) and the fake components (magenta).

In Figure 15.8 the selected data are plotted together with the Standard Model prediction and the expectation of a doubly charged Higgs model for the two most sensitive distributions.

In the invariant mass distribution of all electron pairs in the four central category the peak at 350 GeV and 500 GeV is clearly visible. For the sample with the predicted mass of 350 GeV the expectation in the bin around the generated mass is in the same order as the Standard Model expectation and the selected data. For a mass of 500 GeV the distribution is less sensitive. A cut which only accepts same sign electrons could increase the sensitivity for this model. On the right side the spectrum of the sum of the p_T of all electrons is shown. The doubly charged Higgs model contributes at high values where the Standard Model processes prefer small values of sum p_T. This shows that a cut on the sum of the electron p_T would be could to increase the sensitivity to this model.

The second model beyond the Standard Model, which was considered is a left-right symmetric model which predicts heavy right handed neutrinos. The massive neutrinos are produced via $q\bar{q}' \to W_R^{\pm} \to N\ell^{\pm}$, where W_R is a heavy W-boson, which couples to right-handed particles. The massive neutrino decays into a Standard Model W-boson and a lepton. The Monte Carlo samples were produced for an invariant mass of the W_R-boson of 2 TeV and under the assumption that the flavor of the leptons in the

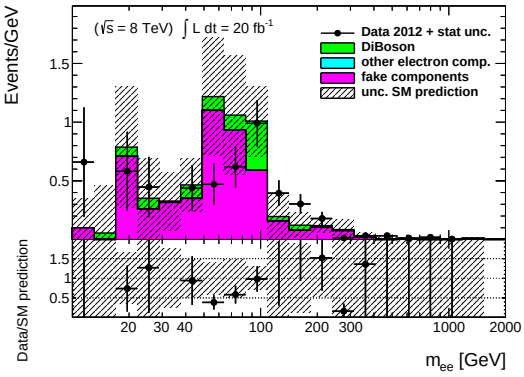

(a) Invariant mass of all possible electron pairs.

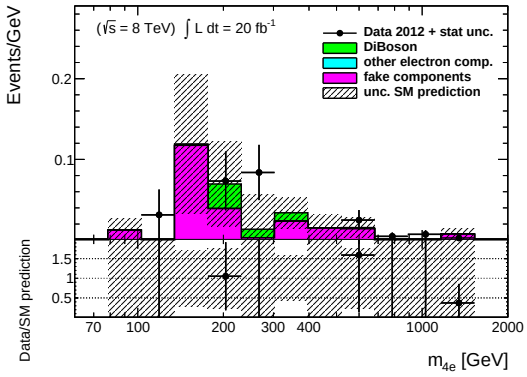

(b) Invariant mass of the four electron system.

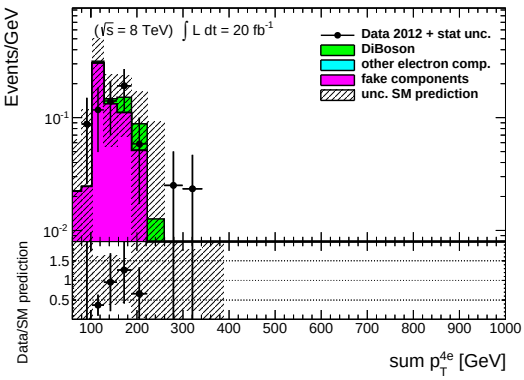

(c) The sum of the p_T of the four electrons.

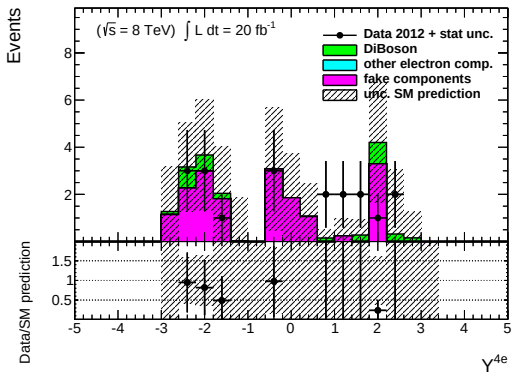

(d) The rapidity of the four electron system.

Figure 15.7: Distributions of the "two central, two forward" category. The black dots shows the result from 2012 data, which is compared to the sum of the diboson (green), other electron contribution (blue) and the fake components (magenta).

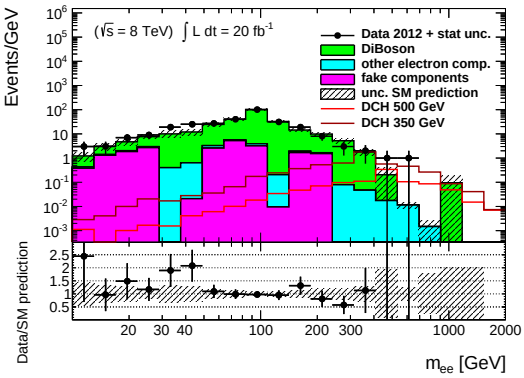

(a) Invariant mass of all possible electron pairs.

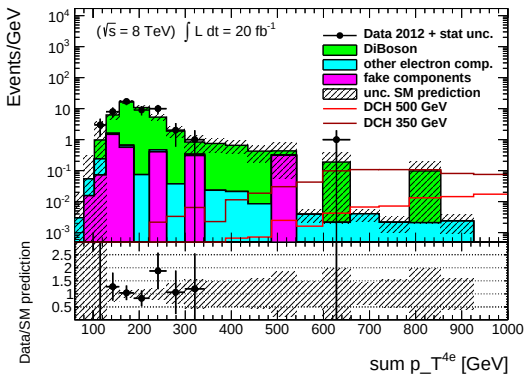

(b) The sum of the p_T of the four electrons.

Figure 15.8: Distributions of the four central category together with the expectation of a doubly charged Higgs model.

production and in the decay are the same. For a predicted mass of the right-handed neutrino of 1.5 TeV the production cross-section is 1.41×10^{-2} pb and for a mass of 1.9 TeV the cross-section is 1.02×10^{-3} pb. In Figure 15.9 the selected data are plot-

ted together with the Standard Model prediction and the expectation of the left-right symmetric model for the two most sensitive distributions.

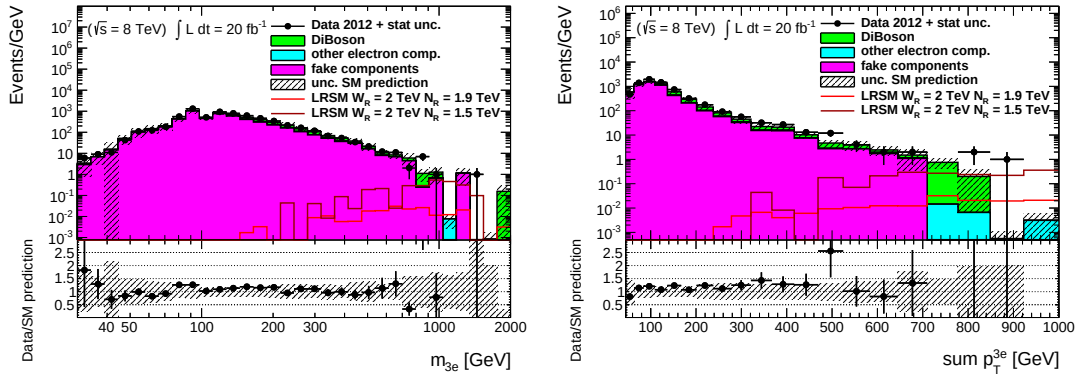

(a) Invariant mass of all possible electron pairs.

(b) Invariant mass of the four electron system.

Figure 15.9: Distributions of the four central category together with the expectation of a left-right symmetric model.

The invariant mass of the three electron system in the "three central" category (left) and the sum of the p_T of all electrons (right) are shown. In the invariant mass spectrum and in the distribution of the sum p_T the left-right symmetric model contributes at high values. Since the contribution of the neutrino from the W-boson decay into an electron and a neutrino is missing it is not possible to reconstruct the invariant mass of the W_R-boson. With a cut on the missing transverse energy it should be possible to increase the sensitivity to this model.

PDF-XChange Editor
Click to BUY NOW!
tracker-software.com

PDF-XChange Editor
Click to BUY NOW!
tracker-software.com

Part V

SUMMARY AND OUTLOOK

PDF-XChange Editor
Click to BUY NOW!
tracker-software.com

16

SUMMARY AND OUTLOOK

The Standard Model of particle physics is very successful in explaining a wide variety of experimental results. However, there are some experimental observations which cannot be explained. Several attempts to extend the Standard Model have been proposed, but for now non of them is widely accepted. In this thesis two measurements with high-energy electrons/positrons in proton-proton collisions have been presented. The measurement of the Drell-Yan cross-section as a precision test of the Standard Model and a model independent search for new phenomena beyond the Standard Model within multi-electron/positron final states.

The measurement of the differential cross-section of the process $pp \to Z/\gamma^* + X \to e^+e^- + X$ in bins of the invariant mass m_{ee} in a range from 116 GeV to 1500 GeV was presented. The Drell-Yan process is a theoretically well described process with a clean experimental signature and low background. This allows to probe the quantum chromodynamics at next-to-next-to-leading order (NNLO) in perturbation theory. Furthermore, the Drell-Yan production of e^+e^- pairs is a source of background for other Standard Model processes and the mass spectrum may be modified by new physics phenomena. Data collected with the ATLAS detector in 2011 at a center-of-mass energy of $\sqrt{s} = 7$ TeV, corresponding to an integrated luminosity of 4.77 fb^{-1}, has been analyzed. Events with two electrons reconstructed in the central region of the detector ($|\eta| < 2.47$) and with a transverse momentum (p_T) larger than 25 GeV were selected. To remove background from misidentified objects the selected electrons had to fulfill several identification requirements. The main contributions of real electron background were estimated using Monte Carlo simulations. Significant contributions are coming from diboson, $t\bar{t}$, and single top production processes. The $t\bar{t}$ background is dominant over the whole mass range. It is of the order of 3% for lower invariant masses and of the order of 10% for higher invariant masses. Other contributions, such as $DY \to \tau\tau$ and $W\gamma^*$ have been found to be negligible. To estimate the amount of background from remaining misidentified objects a data-driven method was used. The number of signal events[1] were corrected for detector and migration effects using a bin-by-bin correction, estimated on the signal Monte Carlo sample. The results are presented at "Born[2]" and "dressed[3]" level. The systematic uncertainties are of the order of 3% to 5%. Up to 400 GeV the statistic component is of the same order (1% - 5%) and becomes dominant for larger invariant masses (up to 50% for the highest mass bin). The result at "Born"

1 The number of selected events minus the background estimation.
2 Without final state radiation.
3 Including final state radiation (FSR) but with partial QED FSR corrections, taking only the collinear radiation into account.

level is compared to NNLO theoretical predictions calculated with FEWZ 3.1 [99] using different PDF sets. The effect of photon induced electron-positron production has been found to be not relevant for this measurement. With respect to the prediction the measured cross-section is roughly 6% larger over the whole mass range. The shape of the cross-section is within the uncertainties well described by the predictions. The PDF sets ABM11 [105] and HERAPDF1.5 [104] shows the best agreement. The result at "dressed" level is compared to the cross-section extrapolated from the Monte Carlo generators PYTHIA [83], MC@NLO [88], and SHERPA [86]. To be able to compare the predicted shape of the different generators the cross-sections were not corrected for higher orders, but the distributions were scaled to the same inclusive cross-section as the measured data. The global scaling factors are between 9% for MC@NLO and 43% for SHERPA. Within the uncertainties the shape of all generators fits the measured distribution.
The result of this analysis was published in [42]. For this thesis a new set of electron identification cuts and a new energy calibration were used. Also the method to estimate the fake background contribution was optimized. With the new set of identification cuts it was possible to reduce the fake background by nearly 70% with reduced signal efficiency of around 15%. With the changes it was possible to reduce the systematic uncertainties of the measurement significantly. A comparison between the old result and the new measurement shows that both are consistent.
A measurement of the high-mass Drell-Yan cross-section with data from 2012 collected at a center-of-mass energy of $\sqrt{s} = 8$ TeV is ongoing [113]. A higher integrated luminosity allows a measurement of the double differential cross-section in m_{ee} and rapidity of the di-electron system. It is also possible to reduce the uncertainties further and to get a higher sensitivity on PDF fits. Preliminary results of the measured cross-section show the same deviation from theoretical predictions as the analysis presented in this thesis. In addition, this measurement is combined with the cross-section measurement of Drell-Yan production of $\mu^+\mu^-$ pairs.

A model independent search for final states with high electron/positron multiplicity was presented in the second part of this thesis. Several theories, trying to explain observed phenomena which can not be explained by the Standard Model, such as dark matter or neutrino masses, predict new processes with three of more electrons/-positrons in the final state. Examples of these theories are the Seesaw mechanism [55] which predicts massive neutrinos and the minimal supersymmetric extension of the Standard Model [20] which can explain dark matter. For this analysis, data collected with the ATLAS detector in 2012 at a center-of-mass energy of $\sqrt{s} = 8$ TeV, corresponding to an integrated luminosity of 20.3 fb^{-1}, were used. Electrons/positrons from the central region of the detector ($|\eta| < 2.47$) with $p_T > 15$ GeV and electrons/positrons reconstructed in the forward region[4] of the detector ($2.5 < |\eta| < 4.9$) with $p_T > 20$ GeV were used. The forward region of the detector was included and the p_T requirements were kept as low as possible to get a large phase space for this search. A set of identification cuts of medium quality were applied to the selected objects. The events were separated by the electron/positron multiplicity. The Standard Model prediction for processes with the correct number of electrons/positrons in the final state was estimated using Monte Carlo simulations. Beside the diboson production processes, which are

4 This region of the detector is not covered by the tracking system.

dominant for most of the channels, the $t\bar{t}$ production in association with vector bosons, triple vector boson production, and Higgs-boson decay via ZZ was taken into account. The Standard Model contributions from processes with at least one object faking the electron/positron signature was estimated using a data-driven method. Therefore, the method used earlier for the Drell-Yan cross-section measurement was further developed to work for events with up to five objects. The comparison between selected events and Standard Model prediction shows no deviation within the uncertainties.

To get a feeling about the sensitivity of this analysis two Monte Carlo samples of processes beyond the Standard Model were used. A left-right symmetric model (LRSM) predicting right-handed massive neutrinos and a model predicting doubly charged Higgses. For the LRSM the analysis shows no sensitivity for regions which are not already excluded by other analyses. A cut on the missing transverse energy can increase the sensitivity. For the doubly charged Higgs model the analysis shows a sensitivity in the four central category, which has been tested for a doubly charged Higgs mass of 350 GeV. This confirms the results from a previous analysis based on $4.8\,\mathrm{fb}^{-1}$ at $7\,\mathrm{TeV}$ [56]. To exclude doubly charged Higgs with masses of the order of 500 GeV a more detailed study is necessary.

In this search the so-called "Matrix method" was used the first time in a analysis to estimate the fake contribution for events with high electron/positron multiplicity. The uncertainty on the data-driven method is quite large and dominates in most of the channels. With larger statistics it should be possible to reduce the uncertainties and to get more sensitive for to signals of models of new physics.

PDF-XChange Editor
Click to BUY NOW!
tracker-software.com

PDF-XChange Editor
Click to BUY NOW!
tracker-software.com

Part VI

APPENDIX

PDF-XChange Editor
Click to BUY NOW!
tracker-software.com

A

ADDITIONAL MATERIAL FOR HIGH-MASS DRELL-YAN CROSS-SECTION MEASUREMENT

Table A.1: Number of events on data for the different selection stages for events with electron pairs with invariant mass $m_{ee} > 116$ GeV. In addition the survival fraction with respect to the previous cut is given.

Cut name	number of events	survival fraction [%]
EGamma stream + skim	110,924,534	-
Good runs list + quality cuts	105,289,950	94.92
Trigger	5,088,966	4.83
Electron η restrictions	593,330	11.66
Electron $p_T > 25$ GeV	397,939	67.07
Medium electron identification	25,577	6.43
B-layer hit if expected	24,773	96.86
Isolation on leading Electron	24,232	97.82

PDF-XChange Editor Click to BUY NOW! tracker-software.com

Table A.2: Table of the DY $\rightarrow$ ee Monte Carlo samples generated with MC@NLO in different regions of invariant mass. Beside the ATLAS internal run number in column two, the cross-sections times branching ratios (column three), the filter efficiency (column four), the number of generated events N_{event} (column five), the corresponding luminosity $\mathcal{L}_{MC}$ is given in column six.

Signature	m_{ee} [GeV]	MC runnumber	$\sigma \times$ BR [pb] MC@NLO	ϵ_F [%]	N_{event} [k]	$\mathcal{L}_{MC}$ [fb^{-1}]
$Z \rightarrow ee$	60-	106087	9.49×10^{2}	100	4259	4.5
DY $\rightarrow$ ee	120-250	126336	9.73	100	193	19.8
DY $\rightarrow$ ee	250-400	126337	4.58×10^{-1}	100	18	39.1
DY $\rightarrow$ ee	400-600	126338	7.34×10^{-2}	100	18	248.5
DY $\rightarrow$ ee	600-800	126339	1.18×10^{-2}	100	18	1548.5
DY $\rightarrow$ ee	800-1000	126340	2.79×10^{-3}	100	18	6569.4
DY $\rightarrow$ ee	1000-1250	126341	9.16×10^{-4}	100	19	20241.3
DY $\rightarrow$ ee	1250-1500	126342	2.35×10^{-4}	100	19	78907.3
DY $\rightarrow$ ee	1500-1750	126343	6.83×10^{-5}	100	19	272586.2
DY $\rightarrow$ ee	1750-2000	126344	2.14×10^{-5}	100	19	870529.4

Table A.3: Table of the DY $\rightarrow$ ee Monte Carlo samples generated with SHERPA in different regions of invariant mass. Beside the ATLAS internal run number in column two, the cross-sections times branching ratios (column three), the filter efficiency (column four), the number of generated events N_{event} (column five), the corresponding luminosity $\mathcal{L}_{MC}$ is given in column six.

Signature	m_{ee} [GeV]	MC runnumber	$\sigma \times$ BR [pb] SHERPA	ϵ_F [%]	N_{event} [k]	$\mathcal{L}_{MC}$ [fb^{-1}]
$Z \rightarrow ee$	75-120	126583	8.03×10^{2}	100	20	>0.1
DY $\rightarrow$ ee	120-250	126584	8.21	100	220	26.8
DY $\rightarrow$ ee	250-400	126585	3.65×10^{-1}	100	20	54.9
DY $\rightarrow$ ee	400-600	126586	5.53×10^{-2}	100	20	361.9
DY $\rightarrow$ ee	600-800	126587	8.88×10^{-3}	100	20	2251.7
DY $\rightarrow$ ee	800-1000	126588	2.04×10^{-3}	100	20	9797.2
DY $\rightarrow$ ee	1000-1250	126589	6.60×10^{-4}	100	20	30320.5
DY $\rightarrow$ ee	1250-1500	126590	1.69×10^{-4}	100	20	118631.0
DY $\rightarrow$ ee	1500-1750	126591	4.87×10^{-5}	100	20	410702.9
DY $\rightarrow$ ee	1750-2000	126592	1.54×10^{-5}	100	16	1040379.7

Table A.4: Table of the DY $\rightarrow \tau\tau$ Monte Carlo samples generated with PHYTHIA in different regions of invariant mass. Beside the ATLAS internal run number in column two, the cross-sections times branching ratios (column three), the filter efficiency (column four), the number of generated events N_{event} (column five), the corresponding luminosity $\mathcal{L}_{MC}$ is given in column six.

Signature	m_{ee} [GeV]	MC runnumber	$\sigma \times$ BR [pb] PYTHIA	ϵ_F [%]	N_{event} [k]	$\mathcal{L}_{MC}$ [fb^{-1}]
$Z \rightarrow \tau\tau$	60-	106052	8.34×10^{2}	100	495	0.5
DY $\rightarrow \tau\tau$	120-250	105489	8.52	100	20	2.0
DY $\rightarrow \tau\tau$	250-400	105490	4.10×10^{-1}	100	20	43.4
DY $\rightarrow \tau\tau$	400-600	105491	6.64×10^{-2}	100	20	274.3
DY $\rightarrow \tau\tau$	600-800	105492	1.10×10^{-2}	100	20	1694.9
DY $\rightarrow \tau\tau$	800-1000	105493	2.65×10^{-3}	100	20	7142.9
DY $\rightarrow \tau\tau$	1000-1250	105494	8.92×10^{-4}	100	20	21929.8
DY $\rightarrow \tau\tau$	1250-1500	105495	2.40×10^{-4}	100	20	85106.4
DY $\rightarrow \tau\tau$	1500-1750	105496	7.34×10^{-5}	100	20	291120.8
DY $\rightarrow \tau\tau$	1750-2000	105497	2.46×10^{-5}	100	20	921659.0

PDF-XChange Editor
Click to BUY NOW!
tracker-software.com

B

ADDITIONAL MONTE CARLO SAMPLES USED FOR THE MULTI-ELECTRON SEARCH

Table B.1: Table of the simulated Monte Carlo samples for the 2012 multi-electron search. All processes listed here are only contributing to the additional category with two real electrons in the final state. Beside the ATLAS internal run number in column two, the used generator (column three), the cross-sections (times branching ratios) times filter efficiencies (column four), the number of generated events N_{event} (column five), the corresponding luminosity $\mathcal{L}_{MC}$ is given in column six.

Signature (filter)	MC runnumber	generator	$\sigma B \times \epsilon_f$ [pb] [%]	N_{event} [k]	$\mathcal{L}_{MC}$ [fb^{-1}]
WW (1 lepton filter)	105985	Herwig	21.71	2489	114.6
$t\bar{t} \to \ell X$	MC@NLO	1.37×10^2	11549	84.2	
$Wt \to X$	108346	MC@NLO	22.37	1767	79.0
DY $\to$ ee (8-15 GeV)	173041	Sherpa	92.15	5000	54.3
DY $\to$ ee (15-40 GeV)	173042	Sherpa	2.79×10^2	14986	53.7
DY $\to$ ee (20-60 GeV)	129501	PowhegPhythia	7.89×10^2	5000	6.3
Z $\to$ ee (60-inf GeV)	147806	PowhegPhythia	1.11×10^3	10000	9.0
DY $\to$ ee (120-180 GeV)	129504	PowhegPhythia	9.85	500	50.8
DY $\to$ ee (180-250 GeV)	129505	PowhegPhythia	1.57	100	63.7
DY $\to$ ee (250-400 GeV)	129506	PowhegPhythia	5.49×10^{-1}	100	182
DY $\to$ ee (400-600 GeV)	129507	PowhegPhythia	8.97×10^{-2}	100	1,115
DY $\to$ ee (600-800 GeV)	129508	PowhegPhythia	1.51×10^{-2}	100	6,623
DY $\to$ ee (800-1000 GeV)	129509	PowhegPhythia	3.75×10^{-3}	100	26,667
DY $\to$ ee (1000-1250 GeV)	129510	PowhegPhythia	1.29×10^{-3}	100	77,519
DY $\to$ ee (1250-1500 GeV)	129511	PowhegPhythia	3.58×10^{-4}	100	279,330
DY $\to$ ee (1500-1750 GeV)	129512	PowhegPhythia	1.12×10^{-4}	100	892,857
DY $\to$ ee (1750-2000 GeV)	129513	PowhegPhythia	3.84×10^{-5}	100	2,604,167

Table B.2: Table of the simulated Monte Carlo samples for the 2012 multi-electron search. All processes listed here are only contributing to the additional category with two real electrons in the final state. Beside the ATLAS internal run number in column two, the used generator (column three), the cross-sections (times branching ratios) times filter efficiencies (column four), the number of generated events N_{event} (column five), the corresponding luminosity $\mathcal{L}_{MC}$ is given in column six.

Signature (filter)	MC runnumber	generator	$\sigma B \times \epsilon_f$ [pb] [%]	N_{event} [k]	$\mathcal{L}_{MC}$ [fb^{-1}]
DY $\rightarrow \tau\tau$ (8-15 GeV)	173045	Sherpa	92.08	5000	54.3
DY $\rightarrow \tau\tau$ (15-40 GeV)	173046	Sherpa	2.79×10^{2}	14993	53.7
Z $\rightarrow \tau\tau$ (60-inf GeV)	147808	PowhegPhythia	1.11×10^{3}	5000	4.5
DY $\rightarrow \tau\tau$ (250-400 GeV)	129546	PowhegPhythia	5.49×10^{-1}	20	36.4
DY $\rightarrow \tau\tau$ (400-600 GeV)	129547	PowhegPhythia	8.97×10^{-2}	20	223
DY $\rightarrow \tau\tau$ (600-800 GeV)	129548	PowhegPhythia	1.51×10^{-2}	20	1,325
DY $\rightarrow \tau\tau$ (800-1000 GeV)	129549	PowhegPhythia	3.75×10^{-3}	20	5,333
DY $\rightarrow \tau\tau$ (1000-1250 GeV)	129550	PowhegPhythia	1.29×10^{-3}	20	15,504
DY $\rightarrow \tau\tau$ (1250-1500 GeV)	129551	PowhegPhythia	3.58×10^{-4}	20	55,866
DY $\rightarrow \tau\tau$ (1500-1750 GeV)	129552	PowhegPhythia	1.12×10^{-4}	20	178,571
DY $\rightarrow \tau\tau$ (1750-2000 GeV)	129553	PowhegPhythia	3.84×10^{-5}	20	520,833

C

ADDITIONAL PLOTS OF THE MULTI-ELECTRON SEARCH

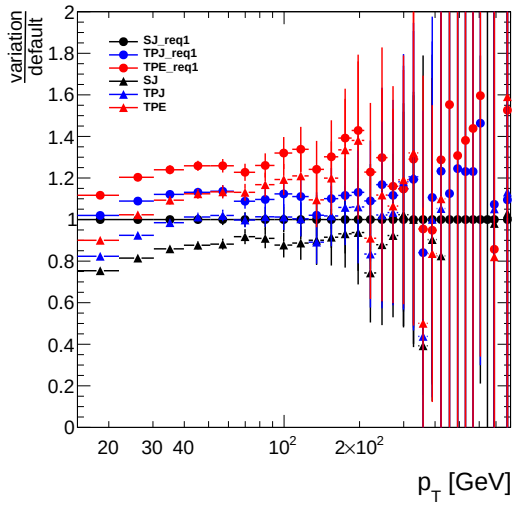

(a) p_T of all electrons.

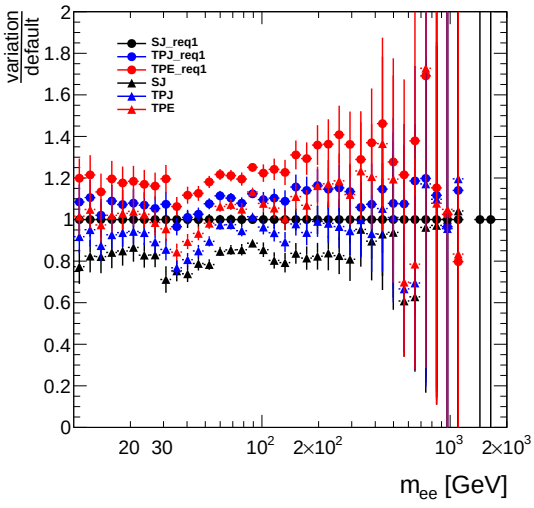

(b) Invariant mass of all electron pairs.

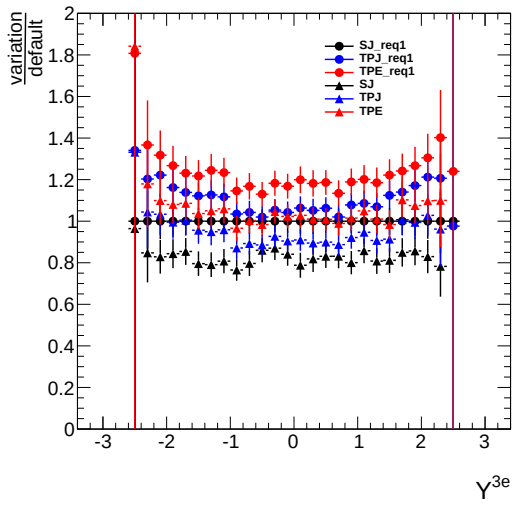

(c) The rapidity of the three electron system.

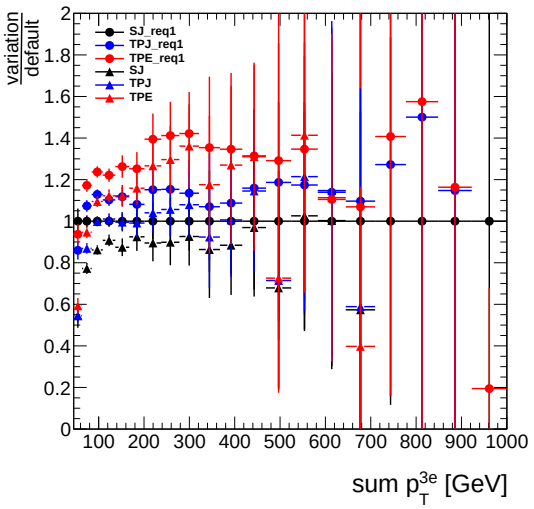

(d) The sum of the p_T of the three electrons.

Figure C.1: Additional ratios of the variations with respect to the default method for distributions of the "three central" category. The largest fluctuation of each bin is used as uncertainty.

PDF-XChange Editor
Click to BUY NOW!
tracker-software.com

BIBLIOGRAPHY

[1] *Diogenes Laertius: Lives of Eminent Philosophers*. Cambridge University Press, Retrieved 14 March 2014.

[2] E. Rutherford. The scattering of alpha and beta particles by matter and the structure of the atom. *Phil.Mag.*, 21:669–688, 1911. doi: 10.1080/14786440508637080.

[3] Sheldon L. Glashow. Partial-symmetries of weak interactions. *Nuclear Physics*, 22 (4):579 – 588, 1961. ISSN 0029-5582. doi: http://dx.doi.org/10.1016/0029-5582(61)90469-2.

[4] Steven Weinberg. A model of leptons. *Phys. Rev. Lett.*, 19:1264–1266, Nov 1967. doi: 10.1103/PhysRevLett.19.1264.

[5] Abdus Salam. Weak and Electromagnetic Interactions. *Conf.Proc.*, C680519:367–377, 1968.

[6] Murray Gell-Mann. A Schematic Model of Baryons and Mesons. *Phys.Lett.*, 8: 214–215, 1964. doi: 10.1016/S0031-9163(64)92001-3.

[7] G. Zweig. An SU(3) model for strong interaction symmetry and its breaking. Version 1. 1964.

[8] G. Arnison et all. Experimental observation of lepton pairs of invariant mass around 95 gev/c2 at the {CERN} {SPS} collider. *Physics Letters B*, 126(5):398 – 410, 1983. ISSN 0370-2693. doi: http://dx.doi.org/10.1016/0370-2693(83)90188-0.

[9] P. Bagnaia et al. Evidence for Zo to e+ e- at the CERN anti-p p Collider. *Phys.Lett.*, B129:130–140, 1983. doi: 10.1016/0370-2693(83)90744-X.

[10] S. Abachi et al. Search for high mass top quark production in $p\bar{p}$ collisions at $\sqrt{s} = 1.8$ TeV. *Phys.Rev.Lett.*, 74:2422–2426, 1995. doi: 10.1103/PhysRevLett.74.2422.

[11] F. Abe et al. Observation of top quark production in $\bar{p}p$ collisions. *Phys.Rev.Lett.*, 74:2626–2631, 1995. doi: 10.1103/PhysRevLett.74.2626.

[12] K. Kodama et al. Observation of tau neutrino interactions. *Phys.Lett.*, B504:218–224, 2001. doi: 10.1016/S0370-2693(01)00307-0.

[13] Georges Aad et al. Observation of a new particle in the search for the Standard Model Higgs boson with the ATLAS detector at the LHC. *Phys.Lett.*, B716:1–29, 2012. doi: 10.1016/j.physletb.2012.08.020.

[14] Serguei Chatrchyan et al. Observation of a new boson at a mass of 125 GeV with the CMS experiment at the LHC. *Phys.Lett.*, B716:30–61, 2012. doi: 10.1016/j.physletb.2012.08.021.

[15] Y. Fukuda et al. Evidence for oscillation of atmospheric neutrinos. *Phys.Rev.Lett.*, 81:1562–1567, 1998. doi: 10.1103/PhysRevLett.81.1562.

[16] Alejandra Melfo, Miha Nemevsek, Fabrizio Nesti, Goran Senjanovic, and Yue Zhang. Type II Seesaw at LHC: The Roadmap. *Phys.Rev.*, D85:055018, 2012. doi: 10.1103/PhysRevD.85.055018.

[17] P.A.R. Ade et al. Planck 2013 results. I. Overview of products and scientific results. 2013. doi: 10.1051/0004-6361/201321529.

[18] V. Fanti et al. A New measurement of direct CP violation in two pion decays of the neutral kaon. *Phys.Lett.*, B465:335–348, 1999. doi: 10.1016/S0370-2693(99)01030-8.

[19] Bernard Aubert et al. Observation of direct CP violation in $B^0 \to K^+\pi^-$ decays. *Phys.Rev.Lett.*, 93:131801, 2004. doi: 10.1103/PhysRevLett.93.131801.

[20] K. Desch, S. Fleischmann, P. Wienemann, H.K. Dreiner, and S. Grab. Stau as the Lightest Supersymmetric Particle in R-Parity Violating SUSY Models: Discovery Potential with Early LHC Data. *Phys.Rev.*, D83:015013, 2011. doi: 10.1103/PhysRevD.83.015013.

[21] S.F. Novaes. Standard model: An Introduction. 1999.

[22] J. Beringer et al. Review of Particle Physics (RPP). *Phys.Rev.*, D86:010001, 2012. doi: 10.1103/PhysRevD.86.010001.

[23] R. Brandelik et all. Evidence for planar events in e+e- annihilation at high energies. *Physics Letters B*, 86(2):243 – 249, 1979. ISSN 0370-2693. doi: http://dx.doi.org/10.1016/0370-2693(79)90830-X.

[24] Michael E. Peskin and Dan V. Schroeder. *An Introduction To Quantum Field Theory (Frontiers in Physics)*. Westview Press, 1995. ISBN 0201503972.

[25] W. Heisenberg. Ueber den bau der atomkerne. i. *Zeitschrift fuer Physik*, 77(1-2):1–11, 1932. ISSN 0044-3328. doi: 10.1007/BF01342433.

[26] John F. Donoghue, Eugene Golowich, Barry R. Holstein, and Mary K. Gaillard. Dynamics of the standard model. *American Journal of Physics*, 61(9):863–864, 1993. doi: http://dx.doi.org/10.1119/1.17428.

[27] P. Longe. The properties of the pauli matrices a, b, c and the conjugation of charge. *Physica*, 32(3):603 – 610, 1966. ISSN 0031-8914. doi: http://dx.doi.org/10.1016/0031-8914(66)90050-4.

[28] Peter W. Higgs. Spontaneous symmetry breakdown without massless bosons. *Phys. Rev.*, 145:1156–1163, May 1966. doi: 10.1103/PhysRev.145.1156.

[29] Steven Weinberg. A model of leptons. *Phys. Rev. Lett.*, 19:1264–1266, Nov 1967. doi: 10.1103/PhysRevLett.19.1264.

[30] H. Georgi. *Lie Algebras in Particle Physics: From Isospin to Unified Theories*. Frontiers in Physics Series. Westview Press, 1999. ISBN 9780813346113.

[31] A.D. Martin, W.J. Stirling, R.S. Thorne, and G. Watt. Parton distributions for the LHC. *Eur.Phys.J.*, C63:189–285, 2009. doi: 10.1140/epjc/s10052-009-1072-5.

[32] John M. Campbell, J.W. Huston, and W.J. Stirling. Hard Interactions of Quarks and Gluons: A Primer for LHC Physics. *Rept.Prog.Phys.*, 70:89, 2007. doi: 10.1088/0034-4885/70/1/R02.

[33] G. Altarelli and G. Parisi. Asymptotic freedom in parton language. *Nuclear Physics B*, 126(2):298 – 318, 1977. ISSN 0550-3213. doi: http://dx.doi.org/10.1016/0550-3213(77)90384-4.

[34] C. Adloff et al. Measurement of neutral and charged current cross-sections in positron proton collisions at large momentum transfer. *Eur.Phys.J.*, C13:609–639, 2000. doi: 10.1007/s100520050721.

[35] S. Chekanov et al. Measurement of the neutral current cross-section and F(2) structure function for deep inelastic e + p scattering at HERA. *Eur.Phys.J.*, C21:443–471, 2001. doi: 10.1007/s100520100749.

[36] R.S. Towell et al. Improved measurement of the anti-d / anti-u asymmetry in the nucleon sea. *Phys.Rev.*, D64:052002, 2001. doi: 10.1103/PhysRevD.64.052002.

[37] J. Pumplin, D. Stump, R. Brock, D. Casey, J. Huston, et al. Uncertainties of predictions from parton distribution functions. 2. The Hessian method. *Phys.Rev.*, D65:014013, 2001. doi: 10.1103/PhysRevD.65.014013.

[38] Sidney D Drell and Tung-Mow Yan. Partons and their applications at high energies. *Annals of Physics*, 66(2):578 – 623, 1971. ISSN 0003-4916. doi: http://dx.doi.org/10.1016/0003-4916(71)90071-6.

[39] August 2014. URL http://en.wikipedia.org/wiki/file:drell-yan.svg.

[40] F. Halzen and A.D. Martin. *Quarks and leptons: an introductory course in modern particle physics*. Wiley, 1984.

[41] J C Collins and D E Soper. The theorems of perturbative qcd. *Annual Review of Nuclear and Particle Science*, 37(1):383–409, 1987. doi: 10.1146/annurev.ns.37.120187.002123.

[42] Georges Aad et al. Measurement of the high-mass Drell–Yan differential cross-section in pp collisions at $\sqrt{s}$=7 TeV with the ATLAS detector. *Phys.Lett.*, B725:223–242, 2013. doi: 10.1016/j.physletb.2013.07.049.

[43] Serguei Chatrchyan et al. Measurement of the Drell-Yan Cross Section in pp Collisions at $\sqrt{s} = 7$ TeV. *JHEP*, 1110:007, 2011. doi: 10.1007/JHEP10(2011)007.

[44] T. Affolder et al. Measurement of $d(\sigma)/dM$ and forward-backward charge asymmetry for high mass Drell-Yan e^+e^- pairs from $p\bar{p}$ collisions at $\sqrt{s} = 1.8$ TeV. *Phys.Rev.Lett.*, 87:131802, 2001. doi: 10.1103/PhysRevLett.87.131802.

[45] B. Abbott et al. Measurement of the high mass Drell-Yan cross-section and limits on quark electron compositeness scales. *Phys.Rev.Lett.*, 82:4769–4774, 1999. doi: 10.1103/PhysRevLett.82.4769.

[46] Georges Aad et al. Measurement of the inclusive $W^{\pm}$ and Z/gamma cross sections in the electron and muon decay channels in pp collisions at $\sqrt{s} = 7$ TeV with the ATLAS detector. *Phys.Rev.*, D85:072004, 2012. doi: 10.1103/PhysRevD.85.072004.

[47] Georges Aad et al. Search for dilepton resonances in pp collisions at $\sqrt{s} = 7$ TeV with the ATLAS detector. *Phys.Rev.Lett.*, 107:272002, 2011. doi: 10.1103/PhysRevLett.107.272002.

[48] Georges Aad et al. Search for high-mass resonances decaying to dilepton final states in pp collisions at s**(1/2) = 7 TeV with the ATLAS detector. *JHEP*, 1211:138, 2012. doi: 10.1007/JHEP11(2012)138.

[49] Georges Aad et al. Search for contact interactions and large extra dimensions in dilepton events from pp collisions at $\sqrt{s} = 7$ TeV with the ATLAS detector. *Phys.Rev.*, D87:015010, 2013. doi: 10.1103/PhysRevD.87.015010.

[50] Georges Aad et al. Measurement of WZ production in proton-proton collisions at $\sqrt{s} = 7$ TeV with the ATLAS detector. *Eur.Phys.J.*, C72:2173, 2012. doi: 10.1140/epjc/s10052-012-2173-0.

[51] Georges Aad et al. Measurement of ZZ production in pp collisions at $\sqrt{s} = 7$ TeV and limits on anomalous ZZZ and ZZγ couplings with the ATLAS detector. *JHEP*, 1303:128, 2013. doi: 10.1007/JHEP03(2013)128.

[52] Serguei Chatrchyan et al. Measurement of associated production of vector bosons and top quark-antiquark pairs at sqrt(s) = 7 TeV. *Phys.Rev.Lett.*, 110:172002, 2013. doi: 10.1103/PhysRevLett.110.172002.

[53] August 2014. URL http://atlas.physicsmasterclasses.org/de/zpath.htm.

[54] Georges Aad et al. Search for heavy neutrinos and right-handed W bosons in events with two leptons and jets in pp collisions at $\sqrt{s} = 7$ TeV with the ATLAS detector. *Eur.Phys.J.*, C72:2056, 2012. doi: 10.1140/epjc/s10052-012-2056-4.

[55] F. del Aguila and J.A. Aguilar-Saavedra. Distinguishing seesaw models at LHC with multi-lepton signals. *Nucl.Phys.*, B813:22–90, 2009. doi: 10.1016/j.nuclphysb.2008.12.029.

[56] Georges Aad et al. Search for doubly-charged Higgs bosons in like-sign dilepton final states at $\sqrt{s} = 7$ TeV with the ATLAS detector. *Eur.Phys.J.*, C72:2244, 2012. doi: 10.1140/epjc/s10052-012-2244-2.

[57] S. Biondini, O. Panella, G. Pancheri, Y.N. Srivastava, and L. Fano. Phenomenology of excited doubly charged heavy leptons at LHC. *Phys.Rev.*, D85:095018, 2012. doi: 10.1103/PhysRevD.85.095018.

[58] Roberto Contino and Geraldine Servant. Discovering the top partners at the LHC using same-sign dilepton final states. *JHEP*, 0806:026, 2008. doi: 10.1088/1126-6708/2008/06/026.

[59] Antonio Delgado, Camilo Garcia Cely, Tao Han, and Zhihui Wang. Phenomenology of a lepton triplet. *Phys.Rev.*, D84:073007, 2011. doi: 10.1103/PhysRevD.84.073007.

[60] Masaki Asano, Krzysztof Rolbiecki, and Kazuki Sakurai. Can R-parity violation hide vanilla supersymmetry at the LHC? *JHEP*, 1301:128, 2013. doi: 10.1007/JHEP01(2013)128.

[61] Lyndon R Evans and Philip Bryant. LHC Machine. *J. Instrum.*, 3:S08001. 164 p, 2008. This report is an abridged version of the LHC Design Report (CERN-2004-003).

[62] ATLAS Collaboration. ATLAS Experiment at the CERN Large Hadron Collider. Technical report, 2008.

[63] CMS Collaboration. The CMS Experiment at the CERN LHC. Technical report, 2008.

[64] LHCb Collaboration. The LHCb Experiment at the CERN Large Hadron Collider. Technical report, 2008.

[65] ALICE Collaboration. The ALICE Experiment at the CERN LHC. Technical report, 2008.

[66] LHCf Collaboration. The LHCf Experiment at the CERN Large Hadron Collider. Technical report, 2008.

[67] The TOTEM Collaboration. The TOTEM Experiment at the CERN Large Hadron Collider. Technical report, 2008.

[68] D.H. Perkins. *Introduction to High Energy Physics*. Cambridge University Press, 2000. ISBN 9780521621960.

[69] *ATLAS muon spectrometer: Technical Design Report*. Technical Design Report ATLAS. CERN, Geneva, 1997. distribution.

[70] *ATLAS detector and physics performance: Technical Design Report, 1*. Technical Design Report ATLAS. CERN, Geneva, 1999. Electronic version not available.

[71] R.W.L. Jones. {ATLAS} computing and the {GRID}. *Nuclear Instruments and Methods in Physics Research Section A: Accelerators, Spectrometers, Detectors and Associated Equipment*, 502(2–3):372 – 375, 2003. ISSN 0168-9002. doi: http://dx.doi.org/10.1016/S0168-9002(03)00446-7. Proceedings of the {VIII} International Workshop on Advanced Computing and Analysis Techniques in Physics Research.

[72] Rene Brun and Fons Rademakers. {ROOT} an object oriented data analysis framework. *Nuclear Instruments and Methods in Physics Research Section A: Accelerators, Spectrometers, Detectors and Associated Equipment*, 389(1–2):81 – 86, 1997. ISSN 0168-9002. doi: http://dx.doi.org/10.1016/S0168-9002(97)00048-X. New Computing Techniques in Physics Research V.

[73] D Caforio. Luminosity Measurement Using Cherenkov Integrating Detector (LUCID) in ATLAS. 2008.

[74] V. Balagura. Notes on Van der Meer scan for absolute luminosity measurement. *Nuclear Instruments and Methods in Physics Research A*, 654:634–638, October 2011. doi: 10.1016/j.nima.2011.06.007.

[75] Georges Aad et al. Improved luminosity determination in pp collisions at $\sqrt{s}$ = 7 TeV using the ATLAS detector at the LHC. *Eur.Phys.J.*, C73:2518, 2013. doi: 10.1140/epjc/s10052-013-2518-3.

[76] ATLAS Collaboration. Electron-performance measurements with the ATLAS detector using the 2011 LHC proton-proton collision data. *Draft to be submitted to: JHEP*.

[77] W Lampl, S Laplace, D Lelas, P Loch, H Ma, S Menke, S Rajagopalan, D Rousseau, S Snyder, and G Unal. Calorimeter Clustering Algorithms: Description and Performance. Technical Report ATL-LARG-PUB-2008-002. ATL-COM-LARG-2008-003, CERN, Geneva, Apr 2008.

[78] Georges Aad et al. Electron reconstruction and identification efficiency measurements with the ATLAS detector using the 2011 LHC proton-proton collision data. *Eur.Phys.J.*, C74:2941, 2014. doi: 10.1140/epjc/s10052-014-2941-0.

[79] Georges Aad et al. Electron and photon energy calibration with the ATLAS detector using LHC Run 1 data. 2014.

[80] Universitaet Konstanz. bwgrid, August 2014. URL http://www.bw-grid.de/projekte/2012/05/11/monte-carlo-generator-for-the-lhc/.

[81] Piotr Golonka and Zbigniew Was. PHOTOS Monte Carlo: A Precision tool for QED corrections in Z and W decays. *Eur.Phys.J.*, C45:97–107, 2006. doi: 10.1140/epjc/s2005-02396-4.

[82] Michael H. Seymour and Marilyn Marx. Monte Carlo Event Generators. 2013.

[83] Torbjorn Sjostrand, Stephen Mrenna, and Peter Z. Skands. PYTHIA 6.4 Physics and Manual. *JHEP*, 0605:026, 2006. doi: 10.1088/1126-6708/2006/05/026.

[84] Torbjorn Sjostrand, Stephen Mrenna, and Peter Z. Skands. A Brief Introduction to PYTHIA 8.1. *Comput.Phys.Commun.*, 178:852–867, 2008. doi: 10.1016/j.cpc.2008.01.036.

[85] G. Corcella, I.G. Knowles, G. Marchesini, S. Moretti, K. Odagiri, et al. HERWIG 6: An Event generator for hadron emission reactions with interfering gluons (including supersymmetric processes). *JHEP*, 0101:010, 2001. doi: 10.1088/1126-6708/2001/01/010.

[86] Tanju Gleisberg, Stefan Hoeche, Frank Krauss, Andreas Schalicke, Steffen Schumann, et al. SHERPA 1. alpha: A Proof of concept version. *JHEP*, 0402:056, 2004. doi: 10.1088/1126-6708/2004/02/056.

[87] Paolo Nason. A New method for combining NLO QCD with shower Monte Carlo algorithms. *JHEP*, 0411:040, 2004. doi: 10.1088/1126-6708/2004/11/040.

[88] Stefano Frixione and Bryan R. Webber. Matching NLO QCD computations and parton shower simulations. *JHEP*, 0206:029, 2002. doi: 10.1088/1126-6708/2002/06/029.

[89] Michelangelo L. Mangano, Mauro Moretti, Fulvio Piccinini, Roberto Pittau, and Antonio D. Polosa. ALPGEN, a generator for hard multiparton processes in hadronic collisions. *JHEP*, 0307:001, 2003. doi: 10.1088/1126-6708/2003/07/001.

[90] S. Agostinelli and et al. Geant4 a simulation toolkit. *Nuclear Instruments and Methods in Physics Research Section A: Accelerators, Spectrometers, Detectors and Associated Equipment*, 506(3):250 – 303, 2003. ISSN 0168-9002. doi: http://dx.doi.org/10.1016/S0168-9002(03)01368-8.

[91] G. Aad, B. Abbott, J. Abdallah, A. A. Abdelalim, A. Abdesselam, O. Abdinov, B. Abi, M. Abolins, H. Abramowicz, H. Abreu, and et al. The ATLAS Simulation Infrastructure. *European Physical Journal C*, 70:823–874, December 2010. doi: 10.1140/epjc/s10052-010-1429-9.

[92] Matteo Cacciari, Gavin P. Salam, and Gregory Soyez. The Anti-k(t) jet clustering algorithm. *JHEP*, 0804:063, 2008. doi: 10.1088/1126-6708/2008/04/063.

[93] J. M. Butterworth et al. ATLAS Collaboration. Single and diboson production cross sections in pp collisions at sqrts = 7 tev. *ATL-COM-PHYS-2010-695*, 2010.

[94] Sven Moch and Peter Uwer. Theoretical status and prospects for top-quark pair production at hadron colliders. *Phys.Rev.*, D78:034003, 2008. doi: 10.1103/PhysRevD.78.034003.

[95] Nikolaos Kidonakis. Two-loop soft anomalous dimensions for single top quark associated production with a W- or H-. *Phys.Rev.*, D82:054018, 2010. doi: 10.1103/PhysRevD.82.054018.

[96] Dag Gillberg. Discovery of Single Top Quark Production. pages 201–204, 2009.

[97] Matteo Cacciari, Gavin P. Salam, and Gregory Soyez. The Anti-k(t) jet clustering algorithm. *JHEP*, 0804:063, 2008. doi: 10.1088/1126-6708/2008/04/063.

[98] M. Aliev, H. Lacker, U. Langenfeld, S. Moch, P. Uwer, et al. HATHOR: HAdronic Top and Heavy quarks crOss section calculatoR. *Comput.Phys.Commun.*, 182:1034–1046, 2011. doi: 10.1016/j.cpc.2010.12.040.

[99] Ye Li and Frank Petriello. Combining QCD and electroweak corrections to dilepton production in FEWZ. *Phys.Rev.*, D86:094034, 2012. doi: 10.1103/PhysRevD.86.094034.

[100] M.R. Whalley, D. Bourilkov, and R.C. Group. The Les Houches accord PDFs (LHAPDF) and LHAGLUE. 2005.

[101] Stefan Dittmaier and Max Huber. Radiative corrections to the neutral-current Drell-Yan process in the Standard Model and its minimal supersymmetric extension. *JHEP*, 1001:060, 2010. doi: 10.1007/JHEP01(2010)060.

[102] A.D. Martin, W.J. Stirling, R.S. Thorne, and G. Watt. Parton distributions for the LHC. *Eur.Phys.J.*, C63:189–285, 2009. doi: 10.1140/epjc/s10052-009-1072-5.

[103] Marco Guzzi, Pavel Nadolsky, Edmond Berger, Hung-Liang Lai, Fredrick Olness, et al. CT10 parton distributions and other developments in the global QCD analysis. 2011.

[104] F.D. Aaron et al. Combined Measurement and QCD Analysis of the Inclusive e+- p Scattering Cross Sections at HERA. *JHEP*, 1001:109, 2010. doi: 10.1007/JHEP01(2010)109.

[105] S. Alekhin, J. Blumlein, and S. Moch. Parton Distribution Functions and Benchmark Cross Sections at NNLO. *Phys.Rev.*, D86:054009, 2012. doi: 10.1103/PhysRevD.86.054009.

[106] Richard D. Ball, Valerio Bertone, Stefano Carrazza, Christopher S. Deans, Luigi Del Debbio, et al. Parton distributions with LHC data. *Nucl.Phys.*, B867:244–289, 2013. doi: 10.1016/j.nuclphysb.2012.10.003.

[107] L. Aperio-Bella, P. Bell, F. Ellinghaus, S. Gadomski, M. Goulette, C. Goeringer, U. Klein, K. Nikolics, G. Pasztor, Y-J. Schnellbach, S. Wollstadt, X. Wu, and M. Zinser. Measurement of the high-mass drell-yan differential cross-section in the di-electron final state: Supporting document.

[108] A.D. Martin, R.G. Roberts, W.J. Stirling, and R.S. Thorne. Parton distributions incorporating QED contributions. *Eur.Phys.J.*, C39:155–161, 2005. doi: 10.1140/epjc/s2004-02088-7.

[109] U. Baur. Weak Boson Emission in Hadron Collider Processes. *Phys.Rev.*, D75:013005, 2007. doi: 10.1103/PhysRevD.75.013005.

[110] Johan Alwall, Michel Herquet, Fabio Maltoni, Olivier Mattelaer, and Tim Stelzer. MadGraph 5 : Going Beyond. *JHEP*, 1106:128, 2011. doi: 10.1007/JHEP06(2011)128.

[111] Inc. Wolfram Research. Mathematica version 10.0. Wolfram Research, Inc. ;Champaign, Illinois, 2014.

[112] Measurement of the b-tag Efficiency in a Sample of Jets Containing Muons with 5 fb−1 of Data from the ATLAS Detector. Technical Report ATLAS-CONF-2012-043, CERN, Geneva, Mar 2012.

[113] Markus Zinser and Stefan Tapprogge. *Double differential cross section for Drell-Yan production of high-mass e^+e^--pairs in pp collisions at $\sqrt{s} = 8$ TeV with the ATLAS experiment*. PhD thesis, Mainz U., Aug 2013. Presented 23 Aug 2013.

ACKNOWLEDGMENTS

Aus datenschutzrechtlichen Gründen in der digitalen Version entfernt.